Fortschritt-Berichte VDI

VDI

Reihe 17

Biotechnik/
Medizintechnik

M.Sc. Robert Cichon,
Dinslaken

Nr. 295

Biomechanical Modeling and Numerical Simulation of minimal-invasive Treatment of Hip Joint Diseases

Biomechanical Modeling and Numerical Simulation of minimal-invasive Treatment of Hip Joint Diseases

Von der Fakultät für Ingenieurwissenschaften,

Abteilung Maschinenbau und Verfahrenstechnik der

Universität Duisburg-Essen

zur Erlangung des akademischen Grades

eines

Doktors der Ingenieurwissenschaften

Dr.-Ing.

genehmigte Dissertation

von

Robert Cichon

aus

Duisburg

1. Gutachter: Prof. Dr.-Ing. Wojciech Kowalczyk

2. Gutachter: Prof. Dr.-Ing. Markus Wimmer

Tag der mündlichen Prüfung: 23.10.2017

Fortschritt-Berichte VDI

Reihe 17

Biotechnik/
Medizintechnik

M.Sc. Robert Cichon,
Dinslaken

Nr. 295

Biomechanical Modeling and Numerical Simulation of minimal-invasive Treatment of Hip Joint Diseases

VDI verlag

Cichon, Robert
Biomechanical Modeling and Numerical Simulation of minimal-invasive Treatment of Hip Joint Diseases
Fortschr.-Ber. VDI Reihe 17 Nr. 295. Düsseldorf: VDI Verlag 2017.
158 Seiten, 97 Bilder, 30 Tabellen.
ISBN 978-3-18-329517-3, ISSN 0178-9600,
€ 51,00/VDI-Mitgliederpreis € 45,90.

Für die Dokumentation: Finite Element Analysis – FEA – Finite Element Method – FEM – Multi Body Simulation – MBS – Hip Joint – Femoroacetabular Impingement – FAI – Femur Head Necrosis – FKN – Orthopedic Medical Engineering

Die vorliegende Arbeit wendet sich an Ingenieure und Mediziner im Bereich der orthopädischen Medizintechnik mit speziellem Fokus auf zwei Hüfterkrankungen, dem Femoroacetabulären Impingement und der Femurkopfnekrose. Zur Untersuchung dieser Krankheitsbilder wurden patientenindividuelle 3D Modelle der Hüfte aus MRT-Datensätzen erstellt. Diese Modelle wurden anschließend in FEM- und MKS Simulationen weiter untersucht, um einen besseren Einblick in die Biomechanik der Hüfte zu erhalten und neue Therapien für diese Erkrankungen zu entwickeln.

Bibliographische Information der Deutschen Bibliothek
Die Deutsche Bibliothek verzeichnet diese Publikation in der Deutschen Nationalbibliographie; detaillierte bibliographische Daten sind im Internet unter http://dnb.ddb.de abrufbar.

Bibliographic information published by the Deutsche Bibliothek
(German National Library)
The Deutsche Bibliothek lists this publication in the Deutsche Nationalbibliographie (German National Bibliography); detailed bibliographic data is available via Internet at http://dnb.ddb.de.

Von der Fakultät für Ingenieurwissenschaften,
Abteilung Maschinenbau
der Universität Duisburg-Essen
genehmigte Dissertation
Referent: Prof. Dr.-Ing. Wojciech Kowalczyk
Korreferent: Prof. Dr.-Ing. Markus Wimmer
Datum der mündlichen Prüfung: 23.10.2017

Als Manuskript gedruckt. Printed in Germany.
ISSN 0178-9600
ISBN 978-3-18-329517-3

Vorwort

Der Grundstein dieser Arbeit wurde bereits während meines Masterstudiums Maschinenbau an der Universität Duisburg-Essen gelegt. Dort wurde ich zum ersten Mal mit dem Thema der Biomechanik konfrontiert und schrieb meine Masterarbeit über den Verschleiß künstlicher Hüftgelenke am Rush University Medical Center, Chicago. Das Angebot von Prof. Dr.-Ing. Wojciech Kowalczyk im Bereich des Hüftgelenkes weiter zu forschen konnte ich im Anschluss meines Auslandsaufenthaltes nicht abschlagen.

An dieser Stelle möchte ich nun die Gelegenheit nutzen und mich bei jenen Menschen bedanken, die durch ihre Mithilfe und Unterstützung das Zustandekommen dieser Arbeit überhaupt erst ermöglicht haben:
Mein besonderer Dank gebührt Prof. Dr.-Ing. Wojciech Kowalczyk zum einen für die Vergabe dieser Dissertation, zum anderen für die ausgezeichnete Betreuung, die gewinnbringenden Gespräche sowie die wissenschaftlichen Diskussionen zur Lösungserarbeitung. Sie haben mich immer wieder zur Weiterarbeit motiviert und mich großartig unterstützt. Herzlichen Dank!

Bedanken möchte ich mich ebenfalls bei Prof. Dr.-Ing. Markus Wimmer für sein Interesse an dem Thema meiner Dissertation und die Bereitschaft die Aufgabe des Zweitgutachters zu übernehmen. An dieser Stelle vielen Dank auch noch einmal dafür, dass Sie mir die Möglichkeit gaben, meine Masterarbeit im Bereich der Biomechanik zu schreiben und damit den Grundstein für diese Dissertation legten.

Mein herzlicher Dank gilt auch PD Dr. med. Stefan Landgraeber für die Betreuung in den medizinischen Fragestellungen während meiner Dissertation und die anschaulichen Erklärungen für Nichtmediziner während der chirurgischen Eingriffe.

Weiterhin möchte ich mich bei all meinen Kolleginnen und Kollegen am Lehrstuhl für Mechanik und Robotik bedanken, allen voran Dr.-Ing. Dominik Raab für die erfolgreiche Zusammenarbeit im Bereich des Hüftimpingements und Henrik Esche für den fachlichen Austausch. Das außerordentlich gute Arbeitsklima, das sich in den Jahren entwickelt hat, die Gruppendynamik und der thematische Austausch waren für mich und meine Arbeit sehr wichtig. Zudem werde ich das Jonglieren in der Mittagspause vermissen.
Auch danke ich den Studenten, die mir das Vertrauen entgegengebracht haben sich von mir beim Schreiben einer wissenschaftlichen Abschlussarbeit betreuen zu lassen und die damit einen spürbaren Beitrag zu der vorliegenden Dissertation geleistet haben.

Ein besonderer Dank gilt meiner Familie und meinen Freunden, die mich während meines Studiums und der anschließenden Promotion immer selbstlos unterstützt haben. Namentlich hervorheben möchte ich an dieser Stelle meinen Freund Jan Pennekamp. Großen Dank

für deine hilfreichen Kommentare, Ideen und deine Ausdauer in den letzten Wochen.

Schließlich möchte ich mich bei meiner Ehefrau Katharina für die Hingabe und Unterstützung während meines gesamten Studiums bedanken. Du warst während der gesamten, nicht immer einfachen, Zeit für mich da und hast mir die nötige Kraft gegeben um die Promotion voranzutreiben. Wenn nötig hast du ein wenig Druck ausgeübt und mir stets Mut und Durchhaltevermögen gegeben. Hierfür bedanke ich mich von ganzem Herzen und freue mich auf viele weitere glückliche Jahre mit dir und unserer Tochter Emma.

Ich liebe dich

Dinslaken 2017
Robert Cichon

"Nicht der Ruhm des Tages tut es,

Nicht das Ziel und was gelang,

Sondern, dass man frohen Mutes

Sich durch Wust und Dornen zwang."

[Ernst Zahn]

Die vorliegende Arbeit ist während meiner Tätigkeit als wissenschaftlicher Mitarbeiter am Lehrstuhl für Mechanik und Robotik der Universität Duisburg-Essen entstanden.

Contents

Nomenclature

(t)	Variable
ϵ	Strain
λ	Lagrange Multiplier
μ	Friction Coefficient
Ω	Frequency
σ	Stress
$\triangle x$	Relative Deformation
ε	Penalty-Parameter
$A(u)$	Differential equation
b	Free body forces acting per unit volume
$B(u)$	Boundary conditions
D	Dampingmatrix
F	Force
f	Load
g	Penetration
K	Stiffnessmatrix
k	Contact Stiffness
k_N	Contact Stiffness for Penalty Algorithm
M	Massmatrix
N_a	Shape function
S	Suitable linear differential operator
u	Displacement
u	unknown function
v	Arbitrary weighting function

W	Potential Energy
ACD	Advanced Core Decompression
CAD	Computer Aided Design
CD	Core Decompression
CT	Computertomography
CT	Computertomography
DICOM	Digital Imaging and Communications in Medicine
FAI	Femoroacetabular Impingement
FE	Finite Element
FEM	Finite Element Method
FHN	Femur Head Necrosis
FNA	Femoral Neck Axis
HHD	Hip Head Diameter
HJC	Hip Joint Center
MRI	Magnet Resonance Imaging
STEP	Standard for the Exchange of Product model data
STL	Stereolithography
THR	Total Hip Replacement

Abstract

Nowadays, quantity of affected patients of hip joint diseases increases. The Femoroacetabular Impingement (FAI) and the Femoral Head Necrosis (FHN) are common diseases, which can lead to a total hip replacement when they are not treated at all.

In literature is stated, that FAI is caused by an abnormal contact between the proximal femur and the acetabular rim, which leads to pain, limitation of movement, and long-term damage of the cartilage. The reason for this is a bony deformity which occurs either at the femoral head (cam-type) or at the acetabular rim (pincer) or combined. The treatment is an arthroscopic surgery in which the bones are shaped. The aim of this study is the development of a patient-individual model which combines motion capture, pain detection, MR-Imaging, FEM and multi-body simulations as well as to navigate the bone removal surgery.

In this study, patient-individual hip joint models (6 patients) are generated based on MRI data. The detection of FAI is performed using a Motion Capture system. During the examination by the physician, the patient is lying in a dorsal position labeled with markers for the marker-based motion tracking. The pain is measured using a pressure detecting bellow simultaneously. MRI data of acetabulum, femur, and labrum are manually segmented and CAD and FEM models are generated. Finally, the CAD model is synchronized with the gait lab's motion data using the maximum angles and simulated in ANSYS with appropriate material properties.

This method is able to visualize and quantify the joint movement of the hip joint. Nevertheless, a contact between labrum and femur could be identified and correlates to the patient's pain. A contact of the bony parts could not be detected. This procedure is performed before and after the surgery to evaluate the surgical outcome. Additional parameter, e.g., Alpha-Angle, an angle between the femoral neck axis and a line connecting the head center with the point of beginning asphericity of the head-neck contour, etc. are used for comparison.

In the future, a standardization of this method can optimize the the planing and the surgical outcome of the bony reduction to guarantee no squeezing of the labrum. A navigation-controlled surgery can help to perform an ideal bone reduction.

The FHN is a disease, which leads to the death of the femoral head after a trauma. An early diagnosis of this disease is essential to avoid joint destruction and to preserve the hip joint.

One possible treatment is the Advanced Core Decompression (ACD), in which a drilling is performed starting from the greater trochanter to the mass point of the necrotic area to achieve a decompression. For a healing of the hip, a complete removal of the necrotic

area is important.

In this study, FEM simulations (190 patients) are used to determine the drilling angles, in which the occurring stresses due to normal walking or downstairs walking are minimal. For this purpose, MRI and CT data are segmented to generate a patient-individual hip model. Furthermore, a neural network is generated to predict the occurring stresses. Additionally, the drilling should be adapted regarding best possible removal using specified surgical instrument.

In the future, FEM simulations should not be necessary to determine occurring stresses during walking anymore. The goal of this study is to determine the optimal drilling regarding the lowest occurring stresses and the best possible removal of the necrotic area and, hence, a navigation-controlled surgery.

Zusammenfassung

Die Anzahl der betroffenen Menschen, die unter Krankheiten am Hüftgelenk leiden, wächst stetig an und so leider auch die Anzahl der Hüftgelenkstotalendoprothetik Operationen. Die Krankheit des Femoroacetabulären Impingements (FAI) und der Femurkopfnekrose (FKN) sind in den letzten Jahren immer präsenter und erfordern bei Nichtbehandlung einen künstlichen Gelenkersatz.

In der Literatur ist festgehalten, dass es sich beim FAI um eine Funktionsstörung handelt, bei der es zu einem unphysiologischen Knochenkontakt zwischen proximalen Femur und dem Acetabulumrand kommt, welcher zu Schmerzen inklusiver Bewegungseinschränkung führt. Mit Hilfe eines arthroskopischen Eingriffs wird die Funktion des Gelenks wieder hergestellt.

In dieser Arbeit werden patienten-individuelle Hüftmodelle aus MRT-Daten entwickelt, um mit Hilfe von FEM- und Mehrkörpersimulationen mögliche Therapieerfolge zu maximieren. Das Bewegungsausmaß des Patienten und die maximal erreichbaren Winkel inbegriffen werden per Motion Capture System ermittelt. MRT-Daten von Acetabulum, Femur und Labrum werden manuell segmentiert und CAD- sowie FEM-Modelle generiert. Die Bewegung der Knochen wird anschließend mit Hilfe der maximalen Winkeln aus dem Motion Capture System in ANSYS mit geeigneten Materialeigenschaften simuliert.

Mit dieser Methode ist eine patientenindividuelle Erstellung eines Hüftmodells und die Visualisierung und Quantifizierung der Gelenkbewegung des Gelenks möglich. Ein Kontakt zwischen den knöchernen Gelenkpartnern konnte nicht festgestellt werden, jedoch kommt es zu einem deutlichen Kontakt von Labrum und Femurknochen. Der Winkelbereich, bei dem der Schmerztaster betätigt wurde, korreliert mit dem Kontakt in der Simulation. Diese Prozedur wird vor und nach dem chirurgischen Eingriff durchgeführt und so wird das Resultat objektiv bewertet. Zusätzlich werden die typischen FAI Parameter, wie Alpha Winkel etc. zum Vergleich herangezogen.

Diese Methode sollte zukünftig standardisiert werden, um den operativen Eingriff besser zu planen und die Reduktion der knöchernen Überbauten am Femurhals optimal zu entfernen, sodass es nicht mehr zur einer Quetschung des Labrums kommt. Eine navigationsgestützte Operation sollte hierbei eingesetzt werden.

Bei der FKN handelt es sich um eine Krankheit, bei der es zu einem Absterben des Femurkopfes kommt, meist ausgehend von einem Trauma. Eine frühe Diagnose dieser Krankheit ist essentiell, um eine Gelenkdestruktion zu vermeiden und das Hüftgelenk zu erhalten.

Die Advanced Core Decompression (ACD), bei der vom Trochanter Major in den Hüftkopf gebohrt wird, um eine Druckentlastung zu erreichen und das Nekroseareal zu entfernen,

hat sich bei dieser Krankheit als sehr gute Therapiemöglichkeit herausgestellt. Um diese Krankheit zu heilen, ist jedoch eine größtmögliche Nekroseausräumung von großer Bedeutung, damit diese sich nicht erneut ausbreitet.
In dieser Arbeit werden mit Hilfe von FEM Simulationen die Winkel bestimmt, bei denen die Belastung bei normalem Gehen oder Treppenabsteigen am geringsten sind. Dazu werden aus MRT- und CT-Daten patientenindividuelle Hüftmodelle extrahiert. Die Spannungen werden für unterschiedliche Nekrose-Volumen und -Orte bestimmt. Des Weiteren werden diese ermittelnden Spannungen in ein neuronales Netzwerk eingebunden, dass eine Vorhersage der auftretenden Spannungen bei vorgegebener Nekrose zukünftig ermöglichen wird. In einem weiteren Schritt muss die Bohrung noch unter dem Gesichtspunkt der optimalen Ausräumung angepasst werden. Bei vorgegebenem chirurgischen Instrument kann der Bereich bestimmt werden, der die größtmögliche Nekrosearealentfernung bringt.
Diese Methode sollte in Zukunft weiter ausgeführt werden, sodass FEM Simulationen nicht mehr notwendig sind, um auftretende Spannungen durch die Bohrung in den Hüftkopf wiederzugeben. Das Ziel dieser Studie ist die optimale Bohrung hinsichtlich niedrigster Spannung und bestmöglicher Nekroseausräumung zu ermitteln und diese im operativen Eingriff navigationsgestützt durchführen zu können.

1 Introduction

Biomechanics is a multidisciplinary area with a lot of different characteristics and special fields which makes it difficult to express a comprehensive definition. Since biomechanical studies are basically addressed to humans, animals or plants, biomechanics can be defined as the application of mechanical principles on biological systems, biological tissues and medical problems [1].

The field Biomechanics has special tasks e.g., simulations of special movements, optimization of performance, design of new implants or acquire new surgery techniques.

Many pathologic conditions can only be treated through understanding the biomechanics, hence assistant treatments of medical problems with the use of engineering techniques are essential. Thus, this graduate thesis should present a new way to look at the hip joint and to get a better understanding of the biomechanics with regard to several diseases such as Femoroacetabular Impingement (FAI) and Femoral Head Necrosis (FHN). Combining motion analysis and multi-body simulations should help to obtain a better understanding of the mechanism of FAI. Finite element simulations should create a new solution to treat the FHN.

1.1 Biomechanics of the Hip Joint

For the diagnosis and treatment, understanding the biomechanics of the natural hip joint is essential. Modern hip arthroplasty is more successful due to advances in this biomechanical knowledge, which led to a development of proper implant designs, fixation techniques, surgical approaches, and therapeutic programs. Supplementarily more valuable insights to injury mechanism, pathologies and hip preservation corrections are results of further research of biomechanical principles [2]. The human hip joint is very suitable for calculations etc. because of its nearly ball and socket-joint form which was investigated by Pauwels et al. [3].

The hip joint, which consists of the acetabulum of the pelvis and the head of the femur, has three rotationally degrees of freedom: flexion/extension, abduction/adduction, and medial/lateral rotation. [4] It is a central element in the human body as it is elementary for the human gait. Furthermore is the connection between acormus and lower extremity and is important for stability and movement. Apart from that, the hip joint is a part of a closed kinematic chain where the distal end is the foot and the proximal end the head [5]. Slight differences in architectural designs of the hip joint between humans already have implications during normal activities as well as dysfunction which can also be related to FAI [2].

For description of an exact position or movement of a body in space, linked coordinate

systems are used. In Biomechanics, special terms for axis and planes have been introduced to describe medical issues, e.g., trauma, which are fixed to the human body and obtained to a straight standing person. The axis and planes are visible in Figure 1.1. The horizontal axis moves side-to-side in the body, the longitudinal axis moves up and down and the sagittal (or anteroposterior) axis runs front to back [6]. Additionally, three planes differentiated into sagittal plane, transversal plane, and frontal plan are visible in the figure. The sagittal axis and longitudinal axis form the sagittal plane, which divides the human body into the left and right part and is perpendicular to the horizontal axis. The transverse plane is formed by the sagittal axis and the horizontal axis and divides the body into upper and lower section [7, 8]. The last plane, which lies parallel to the forehead and is built of the horizontal axis and longitudinal axis, is called frontal plane and divides the body into front and back [7, 8].

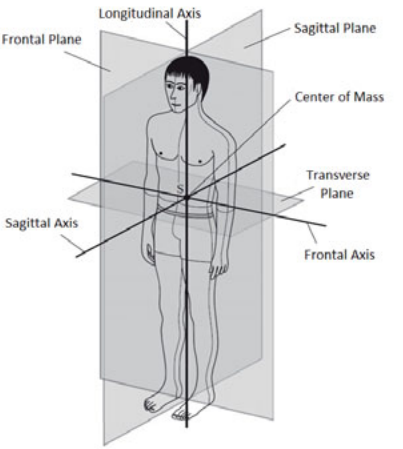

Figure 1.1: Axis and Planes in the Human Body (modified) [1]

Furthermore, the alignment of body parts to the remaining body are explained using medical terms for the directions visible in Figure 1.2. For each body axis, there are two adverse directions. Along the longitudinal axis is called superior, whereas downwards is defined inferior. Alternatively, the terms cranial and caudal are in common use, which mean towards the head and towards the buttocks. The front of the sagittal plane is defined as anterior, the back as posterior. For the rump region, ventral, which means towards the stomach, and dorsal, which means towards the back, are applied. Towards the center of the body the term medial and towards the side lateral are introduced, respectively. Finally, the direction for the legs and arms are distal (towards the hand) and proximal (towards

the body) [7].

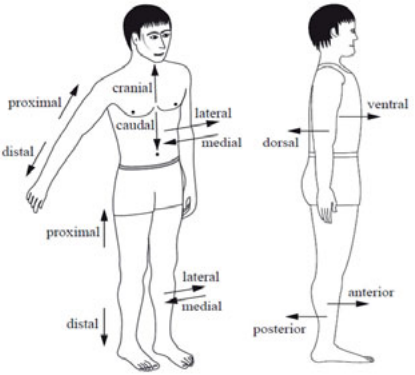

Figure 1.2: Anatomical Terms for Direction [1]

Notably, there are also the relative movements of the body as illustrated in Figure 1.3. The measurement of the active and passive range of motion (ROM) belongs to the functional examination of all joints, and to check for eventually current restrictions of motion. The ROM can be restricted as a reason of pain or palsy. Differences of the active and passive ROM are possible [9]. For each of the three planes, there are two directional movements. For the sagittal plane, flexion and extension, for the frontal plane abduction and adduction can be performed [9]. The movements for the transverse plane are the internal rotation and external rotation [9].

For the remainder of this dissertation, these terms will be used as basic knowledge.

1.1.1 The Hip Joint

The human hip joint consists of *Acetabulum*, *Femur*, *Cartilage*, *Labrum* and surrounding soft-tissues visible in Figure 1.4. Figure 1.5 shows the cuplike concave socket *(Acetabulum)*. The *Acetabulum* consists of *Ilium*, *Ischii,* and *Pubis* and creates the connection between lower and upper extremity. The tighbone *(Femur)* is connected through the femoral neck axis with the head of the joint *(Caput)*. The head of an adult hip has a diameter of 35-55 mm and a surface of around 30 cm^2 [10]. The femoral head is attached to the femoral neck, which is approximately 5 cm long. The femoral neck is attached to the shaft of the femur. In between, existing articulating cartilages which decrease the friction in the joint. The entire periphery of the acetabulum is rimmed by a wedge-shaped fibrocartilage called acetabular labrum *(Labrum)*. The extension of the acetabulum gives stability, because it deepens the socket, the concavity is increased due to its triangular shape, which grasps the

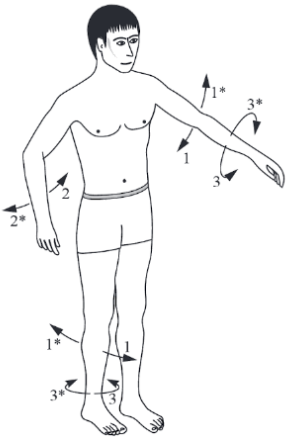

(1*) Extension
(1) Flexion
(2*) Abduction
(2) Adduction
(3*) External Rotation
(3) Internal Rotation

Figure 1.3: Relative Movement of the Musculosskeletal System (modified) [1]

femoral head to maintain the contact with the acetabulum. In addition, new studies show a hermetic closure of the joint which enables hydrostatic lubrication properties. Ferguson et al. [11] found out that hydrostatic fluid pressure in the joint was greater with labrum than without which led them to the statement that the labrum may enhance joint lubrication if the labrum adequately fits the femoral head. In addition, a working labrum hinders subluxation due to the vacuum produced.and the synovial fluid stays in the joint.

The *Femur* has a cavity, so called *Fovea capitis femoris,* which is not covered with articulating cartilage and is the connection to the *Acetabulum*, the *Ligamentum capitis femoris*. This ligament has no mechanical function. However, it is one of the blood supplies to the femoral head. The angle between femoral neck axis and femoris stem is the so called CCD-Angle *(Caput-Collum-Diaphyseal-Angle)* and, in general, is about 126°. *Trochanter major* and *minor* are the starting points for the muscles.

Both bones have neither a spherical shape nor a perfect congruence. The diameter of the head is slightly bigger than the inner diameter of the acetabulum, but due to the cartilages, this incongruity enables a perfect load distribution [13].

Another tasks of the cartilages are the load distribution and minimization of wear due to friction. Thickness of the cartilage both femur and acetabulum varies depending on stress; the thickness of cartilage typically lies between 0 and $2\,mm$ [13]. The acetabular labrum is surrounding the whole acetabulum and stabilizes the joint. Sommerfeld et al. [15] and Putz et al. [16] postulated that the labrum sustains the synovial fluid in the joint and hinders a femoral subluxation due to the vacuum. The hip joint is enclosed by the articular

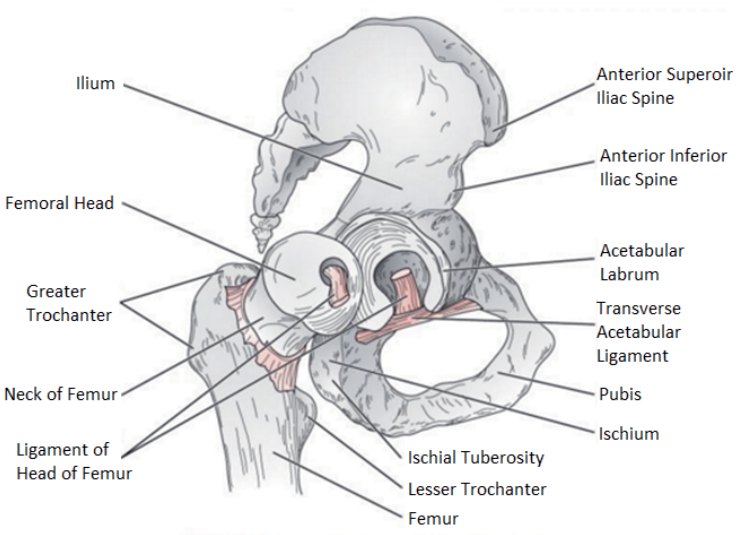

Figure 1.4: Pelvis and Femur [12]

capsule. Other anatomic elements of the hip joint are not necessary for this thesis, refer to appropriate literature e.g. [17] etc.

The ground reaction force and the gravitational force are acting through the pelvis on the human hip joint and create a force couple with a moment arm equal to the distance between the superimposed body weight on the femoral head and the ground reaction force up the shaft. A bending moment is created, which is visible in Figure 1.6a. In the femoral bone are two major and three minor trabecular systems for the transmission of forces as illustrated in Figure 1.6b. Arising from the medial cortex of the upper femoral shaft and radiating through the cancellous bone to the cortical bone of the superior aspect of the femoral head, there is the medial trabecular system. It is additionally oriented along the vertical compressive force passing through the hip joint. The lateral trabecular system is similar and arises from the lateral cortex of the upper femoral shaft and terminates in the cortical bone on the inferior aspect of the head of the femur [4]. The secondary trabecular systems, one for compressive and the another for tensile stresses, a third one is at the trochanteric area of the femur. The crossing point of trabecular systems is the strongest part regarding stress and strain. One area is free of a crossing point and, thus, weaker and has more potential for failure, the so-called zone of weakness [4].

In addition to already named parts of the human hip joint, there are several joint ligaments, e.g. *ligamentum teres*, *ischiofemoral ligament,* or *ligament of the head of the*

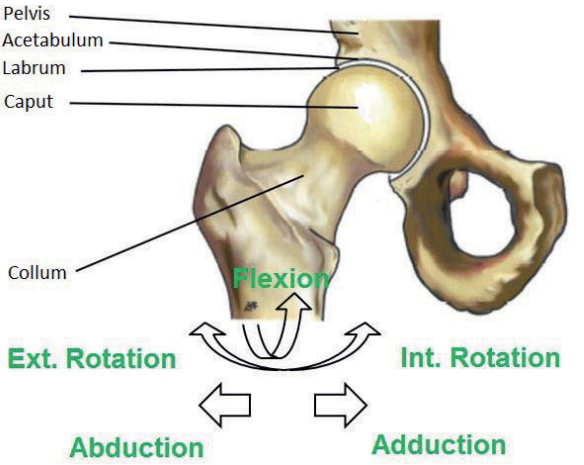

Figure 1.5: Structure of the Hip Joint (modified) [14]

femur [4, 17]. But these ligaments are not so important for the investigated diseases and, thus, not further considered.

1.1.2 Kinematics and Kinetics of the Hip Joint

The human hip joint belongs to the lower limb and its biomechanics can be categorized into kinematics, kinetics, and statics [18]. In general, kinematics describes the functional movements of any joints. Kinetics includes internal muscle forces, and external forces, and moments, which affect a joint. As described in the chapter before, the human hip joint is usually described in terms of kinematics and kinetics with angular rotations (flexion/extension, abduction/adduction, internal/external rotations (Figure 1.7)) and forces acting on the joint. The hip joint is the joint with the highest range of movement [18]. The limitation of movement, also called active range of motion (AROM), is in healthy adult joints bounded by the bony structure, soft tissue including capsule, and labrum, and at least the muscles that cross the joint. [2, 18] The angles are recorded in Table 1.1.

As walking is the most frequent activity during the day, the movement of the hip joint is very important for adults. It has been observed that an adult achieves around 10,000 steps with an average age of 65 during a single day [19]. According to Morlock et al. [20], this accounts for around 85% to 90% of the daily activity spectrum. During gait-activities, relative motion of the hip includes all three angular degrees of freedom. The human gait consists of two phases: the stance and the swing phase. During the stance

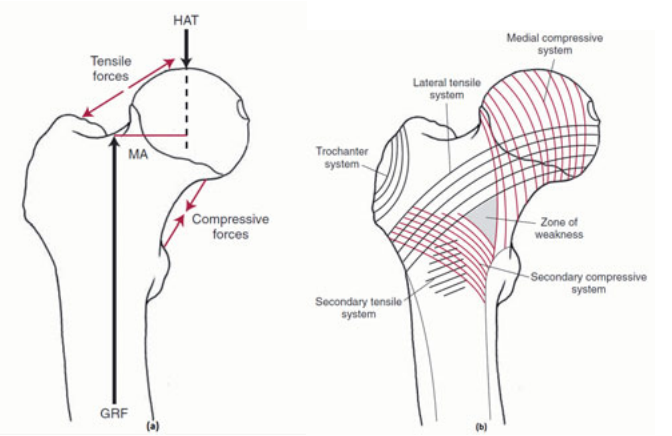

(a) weight-bearing line of the head, arms, and trunk (HAT) loads the head of the femur whereas the ground reaction force (GRF) comes up the shaft of the femur, resulting in a force couple that creates a bending moment, with a moment arm (MA) that is dependent on the length and angle of the neck of the femur. The bending moment creates tensile stress on the superior aspect of the femoral neck and compressive stress on the inferior aspect.

(b) two major (the medial compressive and lateral tensile) trabecular systems show the primary transmission of forces. Additional lines of stress are evident at the secondary compressive tensile systems and at the trochanteric system.

Figure 1.6: Weight-Bearing Systems and Trabecular Systems of the Hip Joint [4]

phase, the hip joint is in a flexed position and consistently extends. During the swing phase, the hip joint change into flexion and stays until heel strike. A healthy adult has a flexion/extension range of about $+30$ degrees flexion and -10 degrees extension during walking. Gait patterns with a decreased range of motion can be the result from illness such as cartilage loss, arthrosis, etc [21].

The joint center lies in the midpoint of the femoral head, the so-called hip joint center. In this point, a Cartesian coordinate system can be arranged to quantify the movements of the human hip joint.

Contrary to kinematics is the kinetics which takes the forces or loads that influence a body into account [8]. The forces coming from the superior and inferior part of the body, which react on the hip joint, are distributed from the pelvic ring. In an upright standing position, the body-weight presses on the promontory of the sacrum which transmits the load through the sacroiliac joint and then to the acetabulum. The hip joint separates the force into caudal (pressure load) and lateral force (tensile load) as illustrated in Figure 1.8a. [22]. The distribution of the forces in the pelvis by the alignment and density of the trabecular structure is shown in Figure 1.8b. The *Linea arcuata* indicates with its

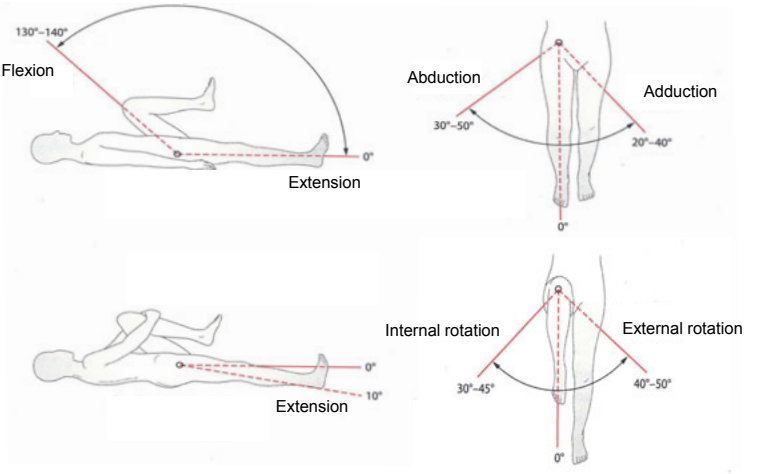

Figure 1.7: Movement of the Hip Joint [17]

Table 1.1: Maximum Angles of Movement for a Healthy Adult [4, 17]

Movement	Maximum Angle in [°]	
Flexion/Extension	130 - 140	10
Abduction/Adduction	30 - 50	20-40
Internal/External Rotation[1]	30 - 45	40-50

[1]with 90° flexed hip

density the magnitude of the force which is transmitted at this area. Compressive stresses can be resisted by one trabecular meshwork pattern going through the femoral head from the superior head across the femoral neck to the medial cortical bone. The other pattern runs from the superior area of the femoral neck towards the greater trochanter, which resists to the tensile stresses [16]. Highest compressive and tensile stresses are located between and below both trochanter [23]. In Figure 1.8c the pressure trabecula is visualized. It is shown that by compressing laterally and medially, bending stresses are absorbed. The Ward's triangle is the area where a less density of the trabecula exist [16].

Bergmann et al. [24] investigated by in-vivo measurements depending on different movements (e.g., slow walking, taking stairs, or sitting), the magnitude of the forces varies highly, however, walking downstairs, each patient reached the highest peak at about 300% of their body weight. The CCD angle may be a reason for a high contact force as suggested by Hochschild et al. [22]. A higher angle than 130° causes an increase of the weight

bearing in the joint and a resulting damage to the cartilage, the so-called *coxa valga* [22].

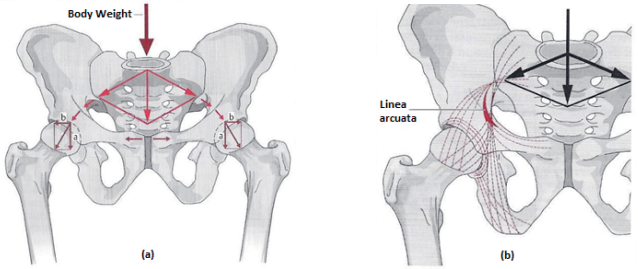

(a) Compressive Load in Standing Position (b) Pattern of Trabecula in Pelvis Area

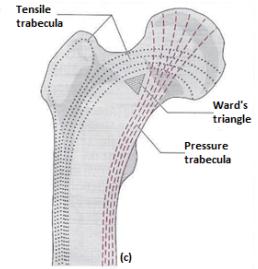

(c) Pattern of Trabecula at Proximal Femur

Figure 1.8: Loading Conditions in a Human Hip Joint [22]

Both diseases, FAI and FHN, may cause a disorder during daily life and physical activities, hence, a limitation of kinematics and kinetics, and generation of pain, which is a reason to investigate these problems and to propose new solutions.

1.2 Diseases of the Hip Joint

Diseases of the hip joint have caused pain, ambulation difficulties, gross deformities, and progressive invalidity for children, teenager and adults. Several different diseases have developed over years such as pseudoarthrosis of the femoral neck, the adult osteoarthritis hip, the femoroacetabular Impingement, the femur head necrosis, etc. [14, 25].

Deterioration of the articular cartilage and the subsequent related changes in articular tissues are the most common painful conditions of the human hip joint. Osteoarthritis (OA) and degenerative arthritis rates lie about 10% to 15% in those older than 55 years men and women. Davis et al. [4] showed that 50% of the cases are considered to be idiopathic, which means that the cause is unknown. The other half of the cases have no evident underlying pathology.

In this thesis both last-mentioned diseases are focused and investigated further to get a better understanding of the mechanism and the treatments.

1.2.1 Femoroacetabular Impingement

Impingement has to be differentiated into the femoroacetabular impingement and extra articular impingement. The femoroacetabular impingement describes a contact between bones in a joint, the extra articular, a contact beyond the joint. The extra articular impingement specifies a contact of the greater trochanter with the pelvis [26, 25]. This study only focuses on the femoroacetabular impingement.

From a medical point of view, the femoroacetabular impingement (FAI) describes an unphysiological contact between Femur and Acetabular caused by a geometrical deformity at the head of femur or acetabulum. Damage of the cartilage and labrum are the result of a not-treated FAI [14]. In the late 1990s, Ganz et al. [27] defined FAI and later found out that FAI is based on a bony deformity of one or both parts of the joint. Patients often suffer from pain and limitation of movement. This restriction is especially evident if the patient performs flexion and/or internal rotation [28]. Nowadays FAI is an admitted disease for hip arthrosis *(Coxarthrose)*.

Today, FAI is differentiated between pincer-type-and cam-type impingement. If the acetabulum is excessively distinctive, and consequently, the reason for the collision, it is named pincer-type impingement (cf. Figure 1.9c). Contrary to the pincer-type, the occurring collision of the cam-type is existing due to an atypical geometry of the proximal femur (cf. Figure 1.9b) [27]. In ca. 75% of the cases, both types appear in a combined manner (cf. Figure 1.9d) [29].

1.2.1.1 Cam-Type Impingement

The cam-type impingement, termed in 2001, is characterized by anatomic deformation of the femoral neck-head junction [31]. This phenomenon is more common in young men aged 20 to 30 [32, 33]. Additionally, new studies reported a higher risk caused by intensive sporting activity in younger age [34, 35, 36]. Typically cam-type is caused by an aspherical femoral head and, hence, a faulty neck-junction compared to the healthy femur, in literature called pistol grip [37]. This aspherical part gets jammed into the acetabulum during defined movement and generates pain and limitation of movement visible in Figure 1.10 [32, 38]. Another cause can be a retroverted femoral head or neck [28]. The labrum is stretched and pushed from the acetabular rim which caused damage to the labrum. The cartilage is pressed into the acetabulum which can also result in damage of the cartilage until cartilage is even sheared off the subchondral bone [37]. Impingement cysts, formerly called herniation pits, can occur at the head-neck junction due to the permanent

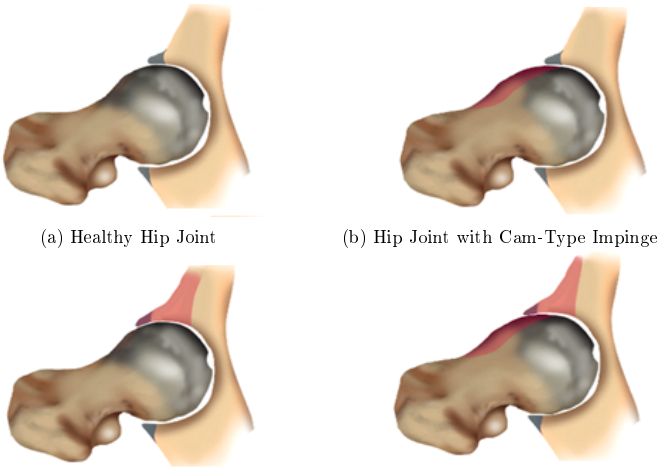

(a) Healthy Hip Joint

(b) Hip Joint with Cam-Type Impingement

(c) Hip Joint with Pincer-Type Impingement

(d) Hip Joint with Combined Impingement

Figure 1.9: Different Types of FAI [30]

contact of the two bones [39]. At a flexion of 90° with a current internal rotation the cam-type impingement mostly occurs. The pain increases by passively adducting the leg which might be a sign for an anterior impingement of the neck on the labrum [40]. In Figure 1.10 the mechanism is shown. The bony deformity is colored in grey, the labrum green, cartilage yellow and the pain in red. Through movement of the femoral bone the labrum and the cartilage is damaged.

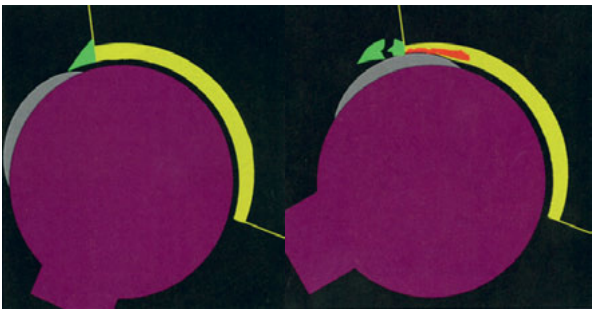

Figure 1.10: Mechanism of Cam-Type Impingement [37]

Geometric parameters are needed, and were established over the last decades, to quantify the abnormality which is causing the cam-type impingement [14].

Nötzli et al. [40] introduced the alpha-angle in 2002, which is the angle between the

femoral neck axis and a line connecting the head center with the point of beginning asphericity of the head-neck contour as illustrated in Figure 1.11.

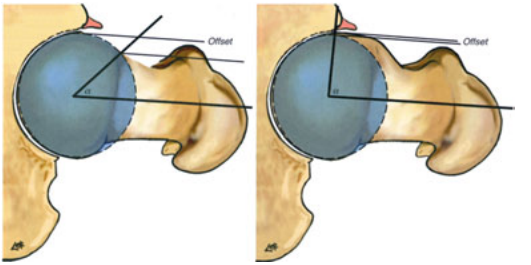

Figure 1.11: Alpha-Angle and Head Neck Offset of the Healthy Hip Joint (left) and a Cam-Typed Hip Joint (right) [41]

The Alpha-angle can be determined around the femoral neck axis, while surgeons classify the femoral head clockwisely in 12 areas with 30° intervals as visible in Figure 1.12, where the femoral head axis represents the center. Evaluation is normally performed on typical areas for FAI, consequently, in the superior or anterior areas (between 12h and 3h) [25]. However, Siebenrock et al. [34] reported that the typical maximum angles can shift as a result of intensive sports such as basketball etc. Nötzli et al. [40] noted that the healthy hip joint state an average value of $42 - 43°$, but often a lower limit is considered as a normal alpha-angle. Values above 50° can indicate cam-type impingement. Ezechieli et al. [29] postulate 44° as a good post surgery result. In general, this parameter is still very controversial.

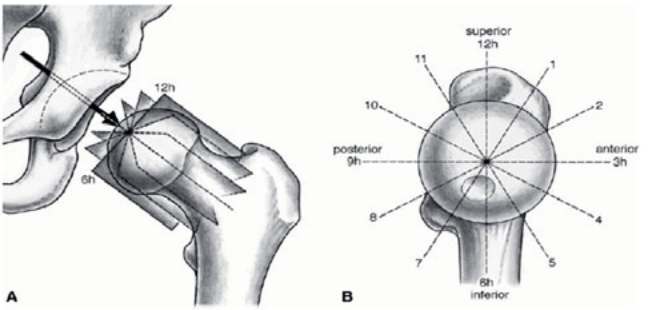

Figure 1.12: Classification of FAI into 12 exact same Areas [34]

To quantify the cam-type impingement, Eijer et al. [42] developed another parameter is the anterior femoral head neck offset (anterior offset or Eijer's offset), which is defined

as the difference in radius between the anterior femoral head and the anterior femoral neck on a cross-table axial view of the proximal femur [32, 43, 42]. For this purpose, two lines in parallel with respect to the femoral neck axis are drawn and the distance between them is measured. The first line starts from the centerline to the furthermost point of the femoral head. The second is similar to the alpha-angle at the point where the asphericity starts. The use of the absolute value of this parameter is limited with regard to the dimensions of each patient. Therefore, a relation between the offset and femoral head diameter is used, called offset-ratio. Affected hips exhibit a ratio smaller than 0.18 [28].

Additionally, Gosvig et al. [44] developed the triangular index which also uses the radius r of the femoral head. The radius is drawn along the femoral neck axis with the center joint center. The height H of the femoral neck is measured as illustrated in Figure 1.13. By drawing hypotenuse R and using Pythagorean theorem, the triangle can be evaluated. Gosvig et al. [44] defined the relation of R and r as a threshold value. If R is bigger than $r + 2mm$, the hip joint is affected. This method is not as rotationally dependent than the alpha-angle.

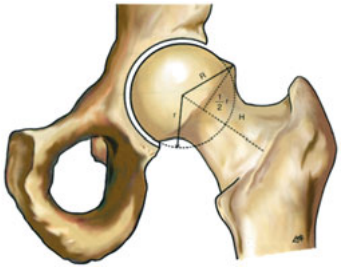

Figure 1.13: Determination of the Triangular Index [41]

Besides these bony additions, another cause for cam-type impingement is a too small femoral neck angle (coxa vara, CCD-angle $< 125°$ (cf. Figure 1.14)) Furthermore, femoral neck fractures can be the reason for a cam-type impingement and even the disease Morbus Perthes, which is responsible for a disturbed blood flow and hence necrosis of the bone [37].

Further causes will not be topic of this study.

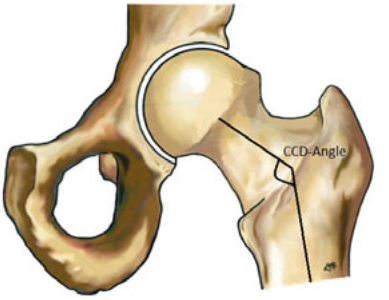

Figure 1.14: Determination of the CCD-Angle (modified) [41]

1.2.1.2 Pincer-Type Impingement

As mentioned in Section 1.2.1, an excessively distinctive acetabulum causes the pincer-type impingement. Especially women with an age of 30-40 are affected [45]. During the contact the labrum, is squeezed between femur and acetabulum and works similar to a damper. This damping prevents further damages of the cartilage, but, unfortunately, the labrum can fossilize after a while (cf. Figure 1.15) [46].

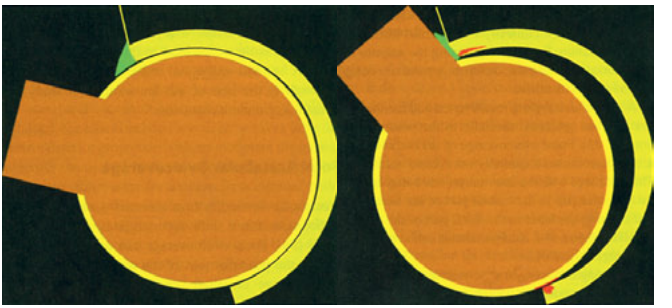

Figure 1.15: Mechanism of Pincer-Type Impingement [37]

A reason for this type of impingement can be a acetabulum, which is too deep. This is the case, if the end of the acetabulum (Figure 1.16F) viewed from the anterio-posterior perspective (so-called linea ilioischiadica in Figure 1.16IL) crosses the line IL. If the femur exceeds the line, doctors call that protrusio acetabuli [41]. New studies show that diagnosing a coxa profunda does not necessarily mean pincer-type impingement [47, 48]. Hence, other indicators such as e.g. CE-angle, acetabular index, or extrusion index, have to be controlled in addition.

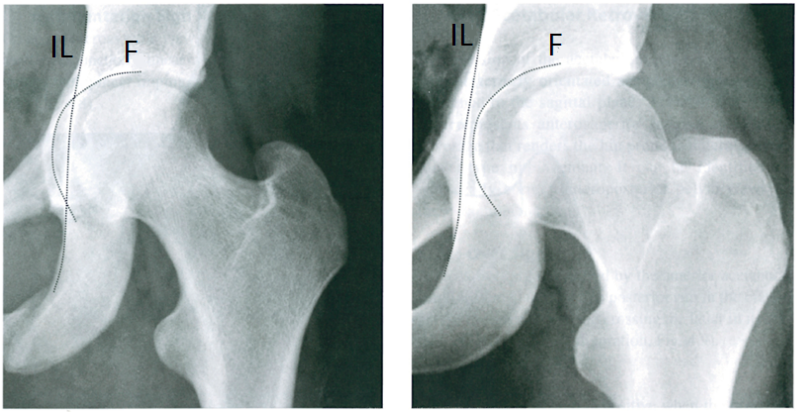

Coxa Profunda Healthy Hip Joint

Figure 1.16: Disease Pattern of Coxa Profunda (modified) [41]

The centre-edge-angle (CE-angle), also called angle of Wilberg [49], is defined as the angle formed by the line passing from the center of the femoral head to the lateral edge of the acetabulum and a vertical line drawn through the center of the femoral head as it is illustrated in Figure 1.17.

Another important anatomical parameter is the alpha angle, defined by Nötzli et al. [40], which describes the relationship between the femoral head and the neck geometry. Combining both parameters, Beck et al. [37] presented that it is feasible to create a computational mode representing a normal joint ($CE = 20°$, $\alpha = 50°$), a dysplastic joint ($CE = 0°$, $\alpha = 50°$), a cam-type joint ($CE = 20°$, $\alpha = 80°$), a pincer-type joint ($CE = 40°$, $\alpha = 50°$), or a combination of cam-type and pincer-type ($CE = 40°$, $\alpha = 80°$).

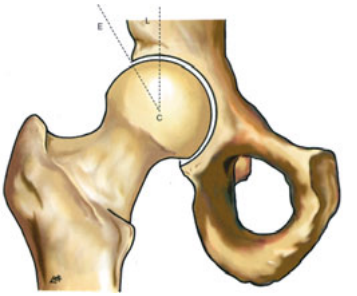

Figure 1.17: Defining the CE Angle [41]

Acetabular index also describes the “coverage” of the femoral head and is determined

as visible in Figure 1.18. The dependence of the femoral head's spherical forming and depth of the acetabular is crucial [41]. Hips with an "over-coverage", e.g., coxa profunda or protrusio acetabuli have an acetabule index of 0° or lower [28].

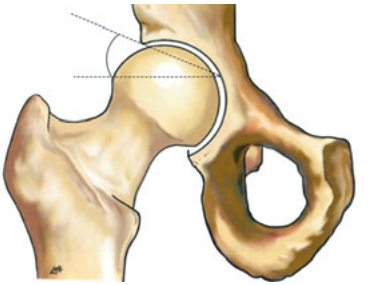

Figure 1.18: Determination of the Acetabular Index [41]

Heyman and Herndon [50] introduced the extrusion index, the percentaged relationship between covered and not-covered femoral head as illustrated in Figure 1.19. Primarily, this anatomic parameter was developed for the evaluation of morbus perthes, however, nowadays, it is still to judge about dysplasia or over-covered hip joints, i.e. so an indicator for FAI. If the value is bigger than 25%, a dysplasia exists. If is it smaller than 10%, it is a over-coverage [32].

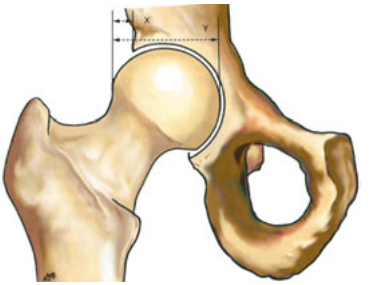

Figure 1.19: Determination of the Extrusion Index [41]

An acetabular retroversion, a backward oriented acetabulum, can be a reason for a pincer impingement. Three signs are essential: the cross-over-sign, the posterior-wall-sign, and ischial-spine-sign. Siebenrock et al. [41] developed the cross-over-sign which means that the anterior and posterior acetabular rims crosses each other. Usually, the anterior acetabular rim is medial compared to the backwards part which is visible in Figure 1.20 [28].

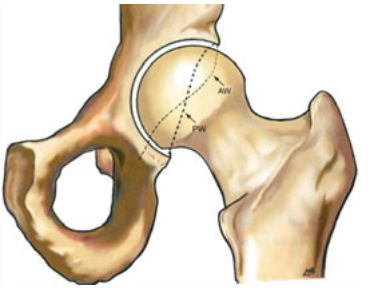

Figure 1.20: Determination of the Cross-Over-Sign [41]

The posterior-wall-sign acts as an FAI indicator, if the hip joint center is closer to the body midpoint than the posterior acetabular rim. Healthy people typically have this sign in the hip joint center. A sign for dyplasia is shown in Figure 1.21, where the posterior-wall-sign lies more medial (Deficient posterior wall) [28].

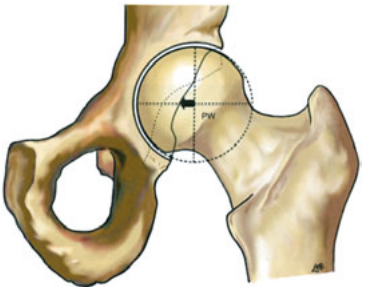

Figure 1.21: Determination of the Posterior-Wall-Sign [41]

The third indicator for a acetabular retroversion is the ischial-spine-sign, introduced by Kalberer et al. [51] in 2008. It describes in a frontal plane, a relevant progress of the spina ischiadica IS medial to the other bony structures (cf. Figure 1.22). However, new studies of Zaltz et al. [52] reported that it is not always an acetabular retroversion, if cross-over-sign and ischial-spine-sign occur.

Figure 1.22: Determination of Ischial-Spine-Signs [41]

After introducing all types of FAI, an overview is illustrated in Table 1.2. All introduced variables are based on static single plane x-rays, which only show one plane of the hip joint and, hence, FAI indicators probably are not visible.

Table 1.2: Geometric Indicators of FAI

Cam-type impingement	Pincer-type impingement
Alpha-Angle (Figure 1.11)	CE-Angle (Figure 1.17)
Anterior Offset (Figure 1.11)	Acetabular Index (Figure 1.18)
Triangular Index (Figure 1.13)	Extrusion Index (Figure 1.19)
CCD-Angle (Figure 1.14)	Cross-Over-Sign (Figure 1.20)
	Posterior-Wall-Sign (Figure 1.21)
	Ischial-Spine-Sign (Figure 1.22)

1.2.2 Osteonecrosis of the Femoral Head

The osteonecrosis of the femoral head or femur head necrosis (FHN) is a disease in which the femoral head dies. This can occur due to various reasons. In general, the death of a bone, called osteonecrosis (ON), in medical terms also aseptic osteonecrosis (AON), means that the reason is not a bacterial infection [53]. The femoral head is dying right under the cartilage and, hence, a reason for a total hip replacement (THR). In Figure 1.23, a pronounced necrotic area is visible.

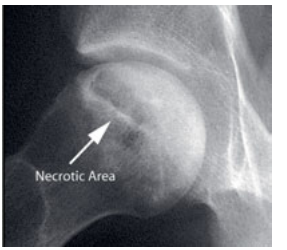

Figure 1.23: X-ray of Hip Joint with Femoral Head Necrosis [54]

This disease is not only a problem of aging, but instead has different causes. A disruption of the bone vascular supply is deemed to be the main cause for femur head necrosis. Apart from that idiopathic case, trauma and systemic conditions, such as alcoholism, steroid use, systemic erythematous lupus, diabetes etc. [55], can be the reason for a osteonecrosis of the femoral head [56].

Mainly two different kinds of ON appear: medullary bone infarction, which attacks the trabecular architecture and marrow cavities in metaphyseal sites, and juxta-articular infarction, which mainly attacks the subchondral bone at major bones (most cases). A special type of FHN is Legg-(Calve-) Parthes Disease (*Osteochondrosis deformans coxae juvenilis*), an avascular necrosis disease introduced by Calve et al. [57], caused by an abnormality of the femoral capital epiphysis in children aged between 5 and 9. Adults, mainly 30 to 60 aged men (occurrence $7:3$), sicken. In Germany, every year around $6,000$ people fall ill [58, 59].

In general, the progress of the femoral osteonecrosis is difficult to predict, however it takes around three years. Both hips are affected mostly within two years as a consequence of wrong load during walking etc. [58]. If this disease is not treated, a collapse of the femoral head is common which ultimately requires THR [60].

Early stages of femoral osteonecrosis patients feel pain around the groin which does not soften and has no trigger, e.g., wrong movement or overloading during sports [58]. Additionally, the pain increases after a while and the internal rotation becomes limited [61]. Due to wrong loading during movement, the pain can transverse into area of the back or even to the knees. Diagnosing FHN, the patient firstly has to be investigated by the attending doctor by palpation and checking the moving possibility. Subsequently, X-rays are performed, an overview of pelvis and most importantly the Lauenstein projection in which the sick hip is $45°$ flexed and $45°$ adducted. In general, this is an axial projection of the hip joint in which particularly the femoral neck is visible uncovered and unshortened (Figure 1.24) [62].

Figure 1.24: Lauenstein Projection of a Healthy Hip Joint [62]

If it is not possible to clear the cause for the pain using a X-ray, additionally, a scintiscan

and MRI are taken. Hence, it is not only possible to see the necrotic area but also a collapse of the femur can be predicted [58]. An alternative method is a CT for patients with cardiac pacemaker etc.

In 1992, the Association Research Circulation Osseous (ARCO) proposed a general classification based on the former Ficat and Arlet system to judge the stage of FHN (Table 1.3) [63, 64, 65].

Table 1.3: Ficat-Arlet Staging System Modified According ARCO [65]

Stage	Characteristics
0	Bone-biopsy results consistent with avascular necrosis; normal findings on all other tests
1	Positive scintiscan or magnet resonance image, or both; lesion subdivided into medial, central, or lateral depending on location of involvement of femoral head
I-A	$< 15\%$ involvement of femoral head
I-B	$15 - 30\%$ involvement of femoral head
I-C	$> 30\%$ involvement of femoral head
II	Radiographic abnormalities (mottled appearance of femoral head, osteosclerosis, cyst formation, and osteopenia); no signs of collapse of femoral head on radiographs or computerised tomography scan; positive scintiscan and magnetic resonance image; no changes in acetabulum; lesions subdivided into medial, central or lateral
II-A	$< 15\%$ involvement of femoral head
II-B	$15 - 30\%$ involvement of femoral head
II-C	$> 30\%$ involvement of femoral head
III	Crescent sign; lesions subdivided into medial, central, or lateral depending on location of involvement of femoral head
III-A	$< 15\%$ crescent sign or $< 2mm$ depression of femoral head
III-B	$15 - 30\%$ crescent sign or $2 - 4mm$ depression of femoral head
III-C	$> 30\%$ crescent sign or $4mm$ depression of femoral head
IV	Articular surface flattened radiographically and joint space shows narrowing, changes in acetabulum with evidence of osteosclerosis, cyst formation and marginal osteophytes

The first ARCO stage is reversible. Is the blood flow still disturbed interstitial fluid accumulates in the medullary cavitiy of the bone, an edema is formed, which degrades the situation in the bone by reason of a higher pressure in the joint. The body tries to repair this, which generates pain [53]. MRI and scintiscan are performed to check the difference in the medullary cavitiy; X-ray and CT show no clinical evidence. [66] Drugs, such as Iloprost, can help to reduce pain and treat the edema. Former treatments with anticoagulants and cholesterol-lowering medicine is not recommended anymore due to non-sufficient effects [58].

Identified as the second ARCO stage, the disease is irreversible and some areas of the hip are already dead the repair mechanisms of the human body failed. In the later stages of ARCO II, the necrosis is visible in X-rays and CT. MRI can clarify the diagnosis within an accuracy of 95% [66].

In stage III, death of the bone increases and the stability decreases. Mechanical collapse of the femur with subchondral fractures starts. The femoral head flattens [66].

The last stage is characterized by cracks of the femoral head. Apart from that, the cartilage at the acetabulum can also be damaged. Finally, a collapse of the femoral head is caused by this disease. The deformation is visible in all imaging techniques. The femoral bone cannot be preserved anymore: a THR is now necessary.

1.3 Goal of this Study

Biomechanics of several joints is very important as described in the following chapters of this thesis. Understanding the Biomechanics of the human hip joint is essential to understand the mechanism which most likely cause FAI and FHN. The ultimate goal is to discover a method to eliminate or prevent the occurrence of these diseases. Total hip replacement might be obsolete afterwards.

Regarding FAI, the function of the labrum must be clarified. Does the pain and the limitation of movement really occur as a result of a bony contact of both joint parts, i.e., the femur and acetabulum, or is it caused by a squeezed labrum? In this part of the dissertation, the bony model is generated based on MRI data, which is manually segmented. In addition, motion analysis is performed to determine the maximum reached angles and the area of pain. Subsequently, the center of the hip joint is determined and by using the angles, the multi-body and finite-element simulations are performed to investigate the Biomechanics of the hip joint. Especially, the function of the labrum in a FAI patient. A comparison between pre-surgery and post-surgery is made to evaluate the surgical outcome. Regarding FHN, one primary goal is to combine FEM calculations with the optimal drilling to get necrosis out of the bone (at least 90%) to guarantee the healing of the femoral head and to prevent the insertion of an artificial joint. In the second part of the dissertation, the hip model including the necrosis area is generated from either MRI or CT data, which has to be segmented. Furthermore, the center of mass of the necrosis has to be calculated to determine the end point of the drilling. A coordinate system is placed at the trochanter major, which is the entrance point for the drilling. FEM simulations are performed to calculate the occurring stresses due to normal and downstairs walking. Finally, a neural network is generated to predict the occurring stresses at the femoral neck and the entrance point, which are the main regions for failure after surgery. The prediction of the neural network is time saving compared to the FEM simulations. Additionally, a

software can be developed which can determine the optimal angle regarding removal of the necrotic area with the known geometry of the used surgical instrument.

For the patient, an improvement in this area might result in a better treatment. While doctors benefit from a decreased treatment period. The cost for treating the human hip joint is significantly lower, as an artificial joint and the respective complicated operation becomes obsolete. These medical and technical problems are important to investigate and I want to contribute towards a new treatment for these diseases by showing that engineering in medical areas is a reasonable approach to improve the currently applied methods.

2 State of the Art

In this section the State of the art is presented which means describes the state before this study is performed. On the one hand there are the engineering investigations, on the other hand the medical issues which are needed to develop such a study. The first part contains the engineering development for biomechanical investigations. Afterwards, the medical techniques are presented.

2.1 Biomechanical Investigation

Engineering techniques are very common in medical fields and nowadays they are being expanded into a new direction: the Biomechanics. Around the 1980s, mechanical techniques were applied on medical problems and new advances have been made such as generateing an understanding of mechanical properties of living tissues, etc. [67]. Biomechanical investigations are primarily specialized into investigations of the human beings, animals, plants, and cells [1]. Additionally, reactions of organisms related to mechanical loading are also a part of Biomechanics [1]. Investigations in the area of Biomechanics of the human hip joint are mainly separated in two parts, the theoretic numerical investigation and biomechanical experiments to validate the simulations. In this section both are briefly introduced and evaluated in the remainder of this thesis.

Generally, development of new products and techniques nowadays run in very quick cycles and customer requirements as well as complexity of technical systems increase.

2.1.1 Biomechanical Numerical Modeling

The classic technical mechanics is not able to reproduce complex, elasto-mechanical relations in real systems completely anymore [68]. For this purpose, all systems are subdivided into their individual components or "elements", whose behavior is understood and, hence, the rebuild of the complete system from such components to investigate the behavior is performed. This is the way to solve those complex problems [69]. Many situations can so be reproduced using a finite number of well-defined components, which is named *discrete*. However, in other situations subdivision are continued indefinitely and the problem can only be defined using mathematical fiction of infinitesimal, which leads to differential equations or equivalent statements which imply an infinite number of elements. These systems are called *continuous* [69]. Using digital computers, *discrete* problems can be easily solved, even if the number of elements is very large and the capacity of all computers is finite, *continuous* problems can be solved exactly by mathematical manipulation [69]. Engineers developed various methods of *discretization* including approximations which approaches in the limit the true continuous problems (continuum) solutions as the number

of discrete variables increases [69]. Mathematicians approached the discretization of continuums using methods such as finite difference approximation, various weighted residual procedures, or approximate techniques, whereas engineers often solve these approaches the problems more intuitively by creating an analogy between the real discrete elements and finite portions of a continuum domain [69].

In the field of solid mechanics, McHenry et al [69] showed good results in elastic continuum problems by replacing small portions of the continuum by an arrangement of simple elastic bars. Afterwards, Turner et al. [69] introduce that small portions in continuums behave in a simplified manner due to considering a more direct substitution of properties. Clough [70, 71] froms the name "FEM" in 1960, where he connected the model of a continuum as a composition of smaller portions (finite elements). Every portion describes the behavior using a function which includes the deformations, elongations, and stresses. Thus, the behavior of the whole system can be described [68]. The goal of FEM is to transfer the problem-describing differential equation into a linear equation systems, which is performed using the variation principle [68]. However, the transfer of the results to the complete system still remains critical, due to the fact that the deviation might be computationally unsolvable [68].

In recent years, many investigations in the biomechanical field were performed, e.g., by Holzapfel et al. [72, 73, 74], who investigated the Biomechanics of soft tissue and arterial walls using numerical models. They investigated among others things the biomechanical behavior of arteries under passive state of the vascular smooth muscles developing a new material model based on FEM. They showed that the numerical approach can describe the theoretical results in remarkable accordance, however, compared to the experimental data there were significant differences and, hence, these can be better reproduced by means of a two-term potential than the classical potential [73]. Furthermore, they developed new material models for arteries, e.g., for the passive state of a healthy and young artery [72].

Other groups, e.g., Ehlers et al. [75], do research on modeling of the human brain tissue and provide a simulation environment to investigate the influence of irregular distribution of infused drugs, which were observed in clinical studies and should help attending surgeons in crucial decisions.

In the orthopedic field, Bergmann et al. [76] conducted studies such as the investigation as well as FE analysis and experimental validation of the femur with an endoprosthesis to determine the strain and stress distributions. The results, generated for different loading conditions, show good accord between experimental and analytical data [76]. Furthermore, differences of maximum and minimal principal stresses in the proximal part of the cement sheath indicate high shear stresses [76]. Supplementary, there were differences in the stress pattern occurring in treated and untreated femurs, which were indicative of increased

stiffness at the proximal end concerning stress-shielding [76]. Apart from that, they found out that prosthesis, cement, and femur were not loaded in a symmetrical way which leads to considerable stress components perpendicular to the stem surface [76].

The same researchers also investigated the deflection, principal, and comparison stresses occurring in a femur for six different loading conditions and found out that in general, the results are very dependent from the assumptions on which they are based, e.g., material properties, geometry, etc. [77]. They confirm that errors occur due to the transfer of bone geometry to a model [77]. They suggested that FEM should only be used for comparative studies in orthopedic area. [77] Quantitative research should be validated by experimental measurements [77].

Woiczinski et al. [78] investigated the knee joint and developed a finite element model of a weight-bearing for total knee replacement to get a better understanding of the clinical aspects after a total hip arthroscopy. The results of the FEM simulations were comparable to the experimental result and, hence, a valid model could be developed [78]. Further work on this project was performed by Steinbrück et al. [79, 80, 81, 82]. Previously, they investigated the patellofemoral contact patterns including the effect of trochlea tilting, the influence of tibial rotation, and the function of the posterior cruciate ligament using appropriate FE models to iteratively develop the optimal knee model [79, 80, 82, 81]. The results of the contact patterns-investigation show an increase of the retropatellar pressure which leads to the anterior pain after the surgery [79]. Additionally, the trochlea of the femoral component might highly influence the pressure distribution of the non-resurfaced retropatellar surface [79]. Patella maltracking can be related to a lower femorotibial rotation and, thus, a new design of the total knee replacement could maintain natural contact patterns due to more conformity of the patella to trochlea [79]. After this study, they investigated the effect of trochlea tilting on patellofemoral contact patterns and identified that the implantation of the femoral component by 3° internal trochlea rotation to transepicondylar line leads to a significant increase of retropatellar pressure compared to 6° external rotation of the trochlea of the femoral component [80]. Ultimately, this results in anterior knee pain after surgery [80]. This maximal retropatellar pressure can be minimized by inserting the femoral component between 3° and 6° to anatomical transepicondylar line, while adequate soft tissue balancing and stable knee kinematics are provided [80]. Subsequently, they investigated the balancing of the posterior cruciate ligament using FEM and showed that a tight posterior cruciate ligament in silico leads to more anterior tibia translation, a higher collateral ligament and inlay stress while the retropatellar pressure remained unchanged [81]. Finally, Steinbrück et al. [82] examined the influence of the tibial rotation in vitro and determined that the rotational alignment of the tibial component to the medial third of the tibial tuberosity or even more externally beyond

that point the anterior pain after a total knee replacement can be avoid.

The group of Bader et al. [83] mostly investigated the cemented ceramic total knee replacements and the load situation and mechanisms, which lead to stress fractures using FEM. Additionally, they investigate the influence of femoral head size on impingement, dislocation and stress distribution in total hip replacements and discovered that an optimal implant position of an artificial hip and a larger femoral head size joints are essential and can reduce the risk of impingement by developing a FEM model [84]. Furthermore, they showed that a hip resurfacing arthroplasty leads to a decrease of range of motion compared to conventional stemmed total hip prosthesis and a large diameter of the femoral neck to an impingement in all movements [85]. In another study of this group, a finite element analysis of the implant bone interface was developed to predict the bone strains and mechanics [86]. To this end, a validation was set using a acetabular cup and a frozen hemipelvis and the results show a good correlation between measurement and calculation except for the micromotion which could not be validated due to a limited accuracy of the motion tracking system [86].

2.1.2 Biomechanical Experiments

Biomechanical experiments are essential to validate simulations results. The combination of experimental testing with multi-body simulations and FEM simulations, so-called evidence-based research, is important to validate the determined results. Biomechanical experiments can be performed in many different fields, e.g., loading investigation of joints during certain activities, investigation of wear particles in artificial joints, muscle forces, and studies on ligaments etc. In this study, the investigation of the FAI requires the maximum angles to simulate the movement which makes a gaitlab analysis necessary. For the necrosis study, the use of forces acting on the hip joint are necessary.

Many studies on artificial joints and wear were performed in the last decades. Morlock et al. [20] performed studies on the human hip joint, where they researched the duration and frequency of every day activities of patients with a total hip replacement. Afterwards, they reported the clinical outcome using the Harris Hip score, which is an indicator used for each hip pathology [20]. They determined that the most frequent patient activity was sitting (44.3% of the time), followed by standing (24.5%), walking (10.2%), lying (5.8%), and climbing stairs (0.4%), however, the the Harris Hip score significantly correlated to the number of stairs [20]. Additionally, they showed a positive tendency with the number of steps per day, respectively [20]. In other studies, Nassutt et al. [87] investigated the influence of resting periods on friction in all common articulation pairings of artificial hip joints using a pin-on-ball testing device. The results showed that initial friction increases with increasing resting duration, especially for metal-on-metal pairings [87].

Biomechanical experiments can also focus on the tribological area such as in an artificial joint which, e.g., Wimmer et al. [88, 89] worked on. They investigate wear and corrosion of artificial hip joints, especially metal-on-metal hip joint bearings and the tribolayer formation, which should minimize wear [88, 89, 90, 91].

Bergmann et al. [24, 92, 93, 94] performed studies on hip contact forces and gait patterns during daily activities such as walking, running, stumbling, carrying, and climbing up and downstairs using instrumented implants and synchronous analyses of gait patterns and ground reaction forces. They suggest to investigate implants mainly using loading conditions that mimic walking and climbing downstairs [24], which is essential for the necrosis study in this thesis.

Furthermore, Düselen et al. [95] study in muscle forces and external loads on ligaments of cadaver knee joints, which were tested in a testing device allowing unconstrained knee joint motion. Quadriceps, hamstring, and gastrocnemius muscle forces were simulated whereas external loads, such as varus-internal or valgus-external rotation forces, were applied and the crucial ligament strain was recorded at different knee flexion angles [95]. In general, the results show that the muscle activation significantly strained the ligaments during the different flexion angles of the knee joint [95]. Hence, a strain minimization should be performed after a surgical intervention of a posterior cruciate ligament and strong muscle contractions should be avoided beyond a knee flexion of 30° [95].

Other biomechanical experiments focus on motions of humans and animals, e.g., Kecskemethy et al. [96, 97], who uses marker-based gait analysis to investigate gait symmetry of stroke patients or worked on a tool to fuse patient-specific data of their bone geometry with an integrated gait motion [98, 99].

In this thesis, a combination of motion analysis, FEM and multi-body simulations are used to determine a new approach for FAI. Additionally, FEM and experiments are combined to develop a new approach for FHN.

As reported in this section, biomechanical investigations can contain numerical models, or experiments, or both. It is very important to validate numerical models using experiments to ensure the numerical results are comparable with the real behavior. The numerical approaches are essential to understand the Biomechanics better.

2.2 Clinical and Biomechanical Diagnostics

Diseases such as FAI and FHN have to be diagnosed using different methods. On the one hand manual investigations are needed to check the mobility of the leg, on the other hand medical imaging is very important to examine the bony structure and the soft tissue of the hip joint.

2.2.1 Medical Imaging

Medical Imaging are techniques to visualize the anatomy of animate beings. It is in combination with biomechanics is very important to get a better understanding of bone deformities. There are different possibilities to image medical problems: e.g., Magnetic Resonance Imaging (MRI), Computer Tomography (CT), or X-ray. The disease in question determines the applied medical imaging approach.

The MRI-technique is used to examine FAI patients. For necrosis X-rays and CTs are performed. It is important is to check the anatomical parameters which indicates the particular disease. Of course, X-ray and CTs are not the optimum techniques given their harmful radiation but still they are complementary imaging technologies and each offers advantages and limitations for particular applications.

2.2.1.1 Magnet Resonance Imaging (MRI)

The magnet resonance imaging (MRI), developed in 1973 by Lauterbur and Mansfield is nowadays used in nearly every medical area for diagnosing and imaging the anatomy and the physiological processes of the body in health and disease [100].

This technique uses hydrogen atoms in human bodies or other biological organisms which hold unpaired atoms. Atomic nuclei have an impaired sum of protons and neutrons in the core, which leads to a spin, so-called nuclear spin. This induces a magnetic field and the core acts as a magnet. Bodies from unpaired elements normally have no external magnetic field, because they neutralize each other by an accidentally arrangement but due to an external magnetic field the orientation of the non-directional magnets changes to parallel or anti-parallel to the magnetic flow direction [101, 102]. Finally, atomic nuclei rotates in a Lamor precession around the axis of the external magnetic field. The frequency of this movement is called Lamor frequency and is dependent from magnetic flux density of the external field and the gyromagnetic constant of the atom nuclei. By stimulating the atoms nuclei in the magnetic field using electromagnetic waves in this frequency, a reaction of the nuclei appears. Protons are deflected off the equilibrium [101]. The nuclear spin depends on the duration of the radiowave [100]. By varying the parameters of the pulse sequence, different contrasts can be generated. At the end of the pulse, the protons return to their initial position and generate a measurable, magnetic energy, called relaxation [102]. This signal gives a conclusion of the density of the protons and the tissue depended relaxation properties of the hydrogen atoms [101].

These are the techniques which are used to perform an MRI examination. The patient is exposed to a magnetic field, created by an permanent, superconducting magnet [100]. This magnetic field is interfered with a high-frequency field (HF) generated by coils. For generating images the relaxation parameters are measured and evaluated. Each tissue

corresponds to a different duration for returning to the equilibrium state after excitation. The density of photons, the number of hydrogen atom nucleus in the body, which is investigated, and the duration of longitudinal relaxation T1 (spin-lattice relaxation) and transverse relaxation T2 (spin-spin relaxation) are essential. In Figure 2.1, the graphs show the longitudinal/transverse relaxation, the time the longitudinal/transverse magnetization needs to get back to the static equilibrium after a HF pulse [102, 100]. The time between two excitation-pulses is called repetition time and can be changed such that the contrast T1 can be appointed. It determines how much longitudinal magnetization recovers between each pulse and is measured in milliseconds. T2 is influenced by the determination of time between the excitation and the recording of the response signal which enables different illustrations of the part, which is investigated [101].

T1-weighted images (T1WI) show fatty tissues bright, while T2-weighted images (T2WI) visualize fluids bright [100].

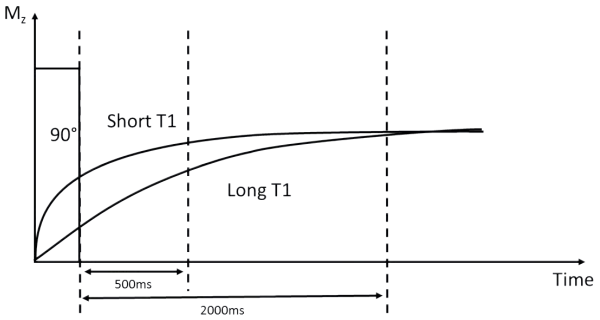

(a) Longitudinal Relaxation

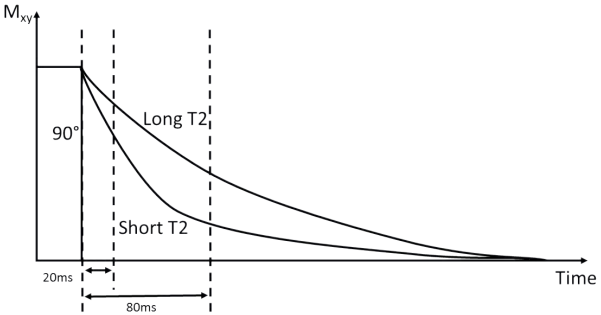

(b) Transverse Relaxation

Figure 2.1: Relaxation Time of MRI [102, 103]

For the generation of tomographies out of the MR signals, a coordinate system has to

be stamped into the model. The first definition of the imaging slice is performed in z-direction. Gradient coils are used to create gradient fields causing no resonance frequency outside of the slice during the HF pulse. The next step is to define the y-direction using the single phases of the spins by relying on another gradient field. Finally, the x-direction is defined using a third gradient field. A Fourier-analysis can split the responding signals and relate these phases to a three dimensional space [100].

An optimal adjustment of the different parameters is necessary to minimize the duration of the MRI investigation for the patients. An optimal contrast of the examined tissues is important for diagnosing, thus, special sequences were developed in the last years, using particular HF-pulses and gradient pulses. Contrast medium (gadolinium) can be used for inflammatory affection or tumors to improve the quality of MRIs. Paramagnetic properties of this medium reduce the T1-time and increase the signal for T1WI [101, 102].

For necrotic areas T1-weighted, and T2-weighted MRI sequences are recorded [104].

2.2.1.2 Computer Tomography

The Computer Tomography (CT) developed in the 1970s by Sir Godfrey Hounsfield is nowadays also very important in nearly every medical field for diagnosing and imaging of the human body. Basics for the CT, which is used today, were developed by Radon in 1917 [105]. The first investigation of a human was performed 1971 and 1979 Hounsfield was honored with the Nobel prize [106].

X-rays always show pictures of the complete structure with minor resolution of the soft-tissue compared with bones, because these have a high contrast. However, CT can generate pictures free from superpositions, which enables to visualize small density differences, e.g., soft-tissues [106].

Images are reconstructed due to the determination of how much of the attenuation coefficient of the narrow X-ray beam occurs in each voxel of the reconstruction matrix [107]. The typical slice thickness is around 0.5 to 10 mm. Gray levels are presented in an 2-dimensional image using the calculated attenuation coefficient [106]. Every object positioned between X-ray tube-detector assembly and detector reduced the intensity of the beam and the attenuation coefficient can be determined [106]. Both parts, the tube-detector assembly and detector, are moving and during this translation motion X-ray path through the subject. The determined intensities are recorded and transferred into images. Nowadays, CTs can record around 700-900 numbers of measurements [106]. After completion of the translation, the whole system rotated around the subject by 1°and the translation is repeated to collect another view. Today, CT scanner collect more than 1.000 views over 360° [107, 106]. Mathematical calculations are required to generate the typical, 2-dimensional images [106].

2.2.2 Motion Analysis

In the following, the motion analysis is introduced. Motion analysis is used in medical terms to investigate special movements of patients and to check whether movements are limited. The files are saved in the special c3d-format, a special file format for motion analysis and gait analysis data containing the three-dimensional coordinates [108].

2.2.2.1 Motion Capture

The motion capture system used in this thesis is from Vicon Nexus (Nexus, Vicon, Oxford, UK), which includes recording of movement of a patient. In this thesis, the system is used for the FAI to investigate the patient-individual range of movement of the hip joint. In Figure 2.2, the top-view of the gait lab at the University Hospital Essen with all its components is illustrated. Thirteen MX13 cameras, positioned higher than the head, are placed around the measuring zone, which includes a 10 m walking distance and a force plate in the middle, which is necessary for the kinetic data. Reflecting markers, which are placed on defined points on the human body, can be recognized by these cameras.

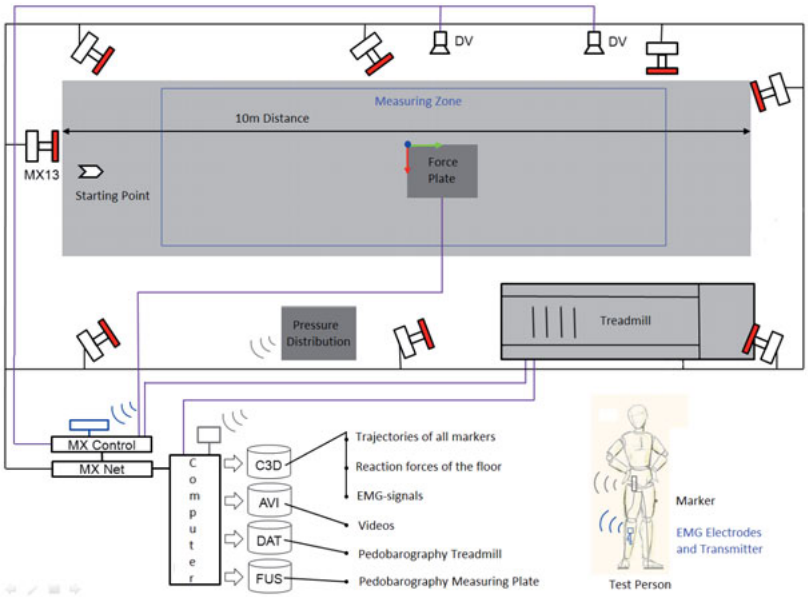

Figure 2.2: Motion Capture System in the University Hospital Essen (modified) [108]

The MX13 cameras send strobe light, which is reflected from the markers and caught from the objective with a maximum resolution of $1280x1024$ pixels. The maximum fre-

quency is eligible until 484 Hz depending on the desired accuracy (in this study 100 Hz). Coordinates of the markers can be calculated using the video file and the position of the camera which enables creating a three dimensional muscoloskeletal system using the belonging software. Quantitative analysis and archiving of movement are possible.

Before beginning with the measurement, a calibration of the cameras is required. Thus, a special tool is moved in the room and the origin of the coordinate system is defined. Additionally, anthropometric datas, such as body height, weight, and length of leg, of the test person are captured. This information is necessary for further calculations, e.g. determination of joint center etc. The width of the joints are determined, as well [108].

The plugin-gait model is a mathematical model of the human body to calculate the kinematic and kinetic data based on the measurements.

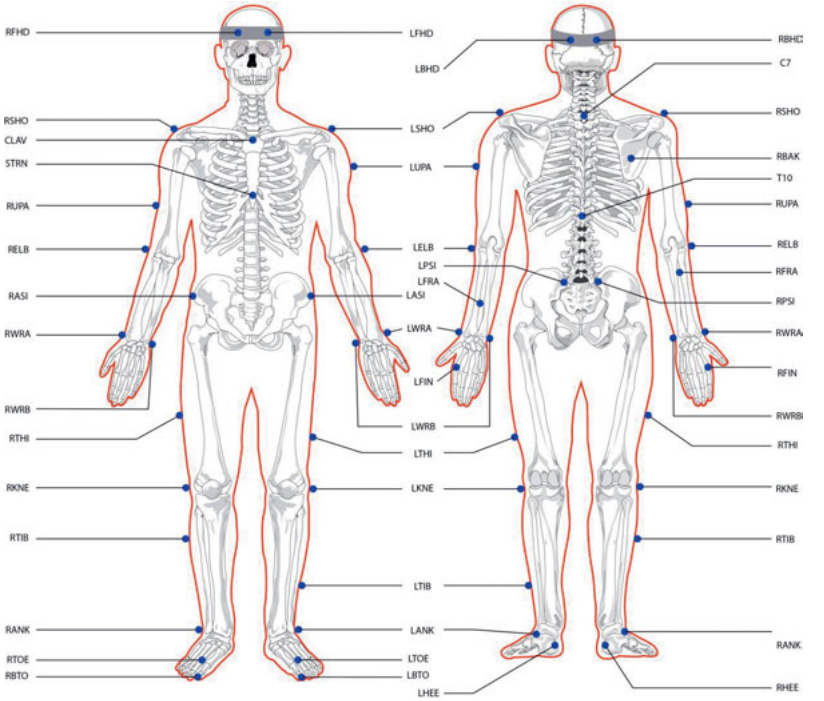

Figure 2.3: Marker-Position According to the Plugin-Gait Model [108]

Figure 2.3 illustrates the positioning of the markers on the human body. The significance of each marker can be referred to source [109]. Markers are placed on joins and other anatomic important areas. The anatomic reproducibility differs from test person to test person and during dynamic testing less skin movement is important to get more

accurate results. For the FAI study, it is sufficient to marker the lower extremity including the pelvis which is illustrated in Figure 2.4 (16 markers). The width of the ankle- and knee joint are needed in addition [108].

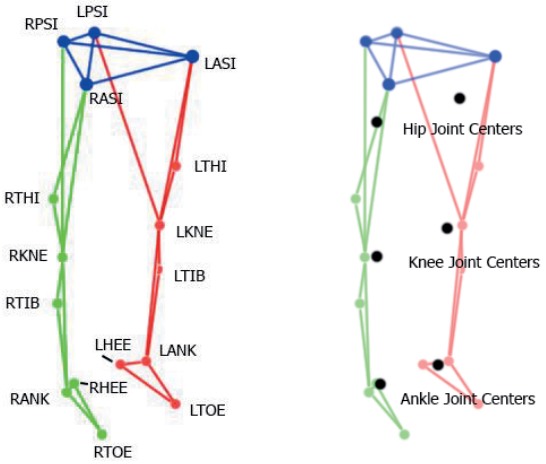

Figure 2.4: Visualization of the modified Plugin-Gait Model for FAI [108]

During the motion analysis the pain of the patient during the movement is recorded using a special developed pain sensor which uses the reflex of cramping the hand to a fist if the patient feels pain [108].

2.2.2.2 Visual Measurement

During the investigation, the patient is lying on a bench. The movement is performed by the doctor, starting from the neutral-zero position to the maximum possible movement (flexion/extension, internal/external rotation, abduction/adduction). Due to the dorsal measurement the marker on the back has to be moved to the iliac crest as illustrated in Figure 2.5 [110, 108]. A validation of this model can be find in Caspers' bachelor thesis [108].

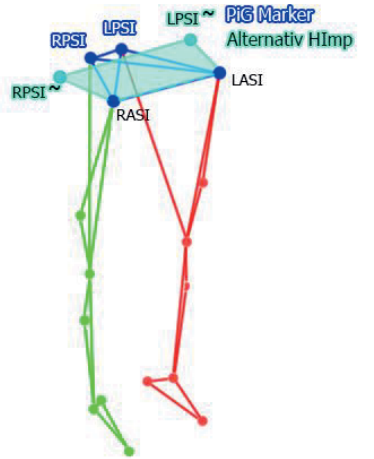

Figure 2.5: Alternative Marker Placement Because of Dorsal Measurement [108]

The maximum angles are captured by the motion capture system. These data are essential for further investigation of the FAI to determine the maximum possible movement of the hip joint for each patient.

2.3 Therapy

In the following, the therapy of FAI and FHN with the current therapy possibilities are explained.

2.3.1 Treatment of Femoroacetabular Impingement

In general, the FAI can be treated conservative with non-invasive or invasive techniques. Non-invasive, conservative treatments such as physiotherapy, electrotherapy, or fango combined with non-sterodial anti-inflammatory drugs (NSAIDs) and no extreme movement of the hip are only short-term aid and cannot solve the problem. Sports with high movements of the hip joint like soccer etc. should be avoided [111]. Patients with symptomatic FAI after being diagnosed clinically and radiologically usually start with a conservative treatment before undergoing a surgery. The favorable outcome of those non-invasive treatments may vary as a consequence of several factors, e.g., the intensity of structural impingement or the phase of secondary osteoarthritis (OA) [112].

If these conservative treatments yield no success, a surgical treatment needs to be applied. The aim is to eliminate the pathomechanism by removing the bony deformities

which causes the impingement lesion and to preserve the joint [111]. A surgery is performed in two types: the open surgery and arthroscopic intervention. Both are effective in short term and midterm, however, the arthroscopy of the hip is state-of-the-art and is often performed to correct the bony deformities and if applicable the defective position of the labrum. Important is this kind of treatment as it is joint preservative and decrease the risk of OA [113].

Surgery of pincer-type FAI was already described in 1936 by Smith-Petersen, where the rim of the acetabulum was altered, for example, from a patient with protrusio acetabuli [114]. This is similar compared to an acetabular retroversion which is performed nowadays.

An access to the acetabulum through an incision is performed, which is used to separate the labrum from the rim of the acetabulum, where the excessice acetabulum is located, without damaging the transition zone between the cartilage and labrum. Afterwards, the bony deformity on the acetabular can be carefully shaped using a burr as visible in Figure 2.6. Kling et al. [115] investigated the amount of bone which has to be removed. The CE angle is responsible and they showed that cutting off $1mm$ would decrease the lateral CE angle by 1°. After trimming, the labrum can be attached back to the acetabular rim by using bone anchors with non-absorbable sutures, also visible in the figure.

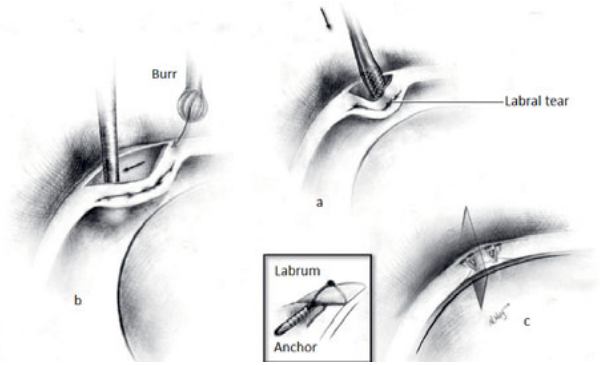

Figure 2.6: Surgical Treatment for Pincer-Type FAI [111]

In case of cam-type FAI, the surgery is concentrated on the femoral head which causes the FAI to correct the deformity. The aspherical part of the femoral head is usually located in the anterosuperior quadrant and the surface of the cartilage has a reddish look [116]. The deformity can be treated using a burr as presented in Figure 2.7. It is important is to be cautious and not to damage the retinacular vessels during the osteoplasty because it can causes avascular necrosis of the femoral head and, finally, the collapse of the joint [111].

Figure 2.7: Surgical Treatment for Cam-Type FAI [117]

Mardones et al. [118] reported that the quantity of the substraction should not exceed 30% of the femoral neck diameter otherwise it may lead to a femoral neck fracture. A failure of the labral seal can additionally appear, if the femoral head-neck junction is over-trimmed referred by Martin et al. [111]. Bone wax is used to stop the bleeding during the surgery [119]. An unsounded labrum must be repaired. Otherwise it will lead to an OA.

FAI is a precursor for hip OA but can be treated. Unfortunately, treatment can be initiated too late which leads then to early OA anyway.

2.3.1.1 History

In 1933 Elmslie [120] presented that people with an age of 40-50 years who had a degeneration of the hip joint already had preexisting undiscovered deformations of the joint which probably could be the reason for it. In 1965, Murray suggested that minor anatomical abnormalities, such as e.g. minimal counterparts of slipped capital femoral epiphysis and acetabular dysplasia resulting an incongruity and premature cartilage degeneration, can cause most cases of primary OA of the hip joint. He demonstrated that in 65% of 200 cases primary OA patients also had some anatomical abnormalities, the other 35% remain as "idiopathic" [121]. He also introduced the term "tilt deformity" of the femoral head as its abnormal relationship to the femoral neck and concluded out that this could cause premature femoral head epiphysial plate fusion, mild trauma, transient synocitis, or minor epiphysiolysis. OA can be developed by this tilt deformity because of joint incongruity. Stulberg and Harris [122] supported Murray's findings and additionally reported in 1974 subtle forms of acetabular dysplasia in more than 40% of patients with so-called idiopathic arthritis. One year later Stulberg [123], described the "pistol-grip deformity" of the proximal femur, similar to Murray's findings, characterized by flattening of the lateral neck surface, hooking at the inferomedial femoral head-neck junction, and loss of height with widening of the femoral head. Solomon postulated besides, that OA was always

secondary due to some underlying anatomical abnormalities. Additionally, he observed that evidences of subtle acetabular dysplasia, tilt deformity, and post-inflammatory OA in most cases of idiopathic or primary hip joint OA [124]. Moreover, he hypothesized that OA always occurs in joints "other things happened first".

Murray et al. [125] also postulated that some sports in a younger age can cause the early mentioned bony deformities at the femoral head are due to extreme kinetic and kinematic stress. In 1976, Resnick [126] assumed that the tilt deformity is not the cause but the consequence of another osteoarthritic process. However, the fact that other joints such as ankle or elbow rarely develop OA contradicts this assumption. Nevertheless, more evidence was required. Until the 1990s the acetabular labral tears became much more important and were increasingly described in orthopedic literature. The role of the acetabular labrum needs to be understood and whether there is a relationship between OA and a damage of the labrum. With the development of the hip arthroscopy, diagnosing labral tears became easier and hip joint articular damage was reported [127, 128]. Later, McCarthy et al. [129] suggested that a labral tear changes the biomechanical environment in the hip joint which leads to degeneration and OA.

In the last decades, clinical techniques improved and based on magnetic resonance imaging a better view on the pathomechanisms involved in FAI is possible because the labrum, cartilages and joint space can be further investigated. In 1999 the term "pincer impingement" was mentioned initially by Myers et al. [130]. Ganz et al. [131] developed a safer access "open surgical hip dislocation" in 2001, which enabled a direct access to and full view of the hip joint avoiding necrosis of the femoral head. They also showed that a small deformity of bony tissue already has a big impact regarding FAI, characterized by pain, limitation of movement and long-term also damage of the labrum and cartilage [132]. Patient studies and cadaver studies were established and Rab et al. [133] supported the trend of understanding the FAI and damage of the hip joint using computer modeling. Deep chondral injuries and secondary damage to the labrum were called "cam impingement" in contrast to "pincer-impingement", which attacks the labrum first, with subsequent lesions occurring in articular cartilage [134]. Later, they postulated that FAI is a critical factor regarding OA after observing more than 600 patients with unexplained causes [132].

However, the real mechanism of damage is not further investigated and remains unclear.

2.3.1.2 Surgery

Surgery of FAI is performed using mainly two different techniques, the open surgical dislocation (Ganz et al. [131]) and the mini-open-arthrotomie (Ribas et al. [135]).

2.3.1.2.1 Open Surgical Dislocation

Ganz et al. [131] developed the open surgical dislocation surgery, the so-called open luxation of the hip joint which is the very first technique for treating FAI and also a technique which is still in use [29, 32]. An advantage is the good accessibility of the joint and, hence, the area of FAI. Nevertheless, this surgery still represents an hard intervention into the human body and the time of rehabilitation is long compared to mini-open access.

2.3.1.2.2 Mini-Open-Arthrotomy and Arthrosopy

In 2007, Ribas et al. [135] developed the mini-open-arthrotomie which enables a more convenient access to the human body for the patient, because the muscle impairment is degraded. Permanent progress of this surgical technique of mini-open arthrotomy and arthroscopy developed a pure arthroscopic method which is less invasive and degrades the complication rate with short rehabilitation time [136, 29]. Pennekamp et al. [32] reported that combined surgery methods are often performed given the limited access to the bony deformity. The chose technique is very dependent from the competence of the attending doctor legible in a study of Garjio et al. [137].

2.3.2 Treatment of Femur Head Necrosis

Femur head necrosis is a disease which occurs in patients younger than 25 years and are most often treated with a total hip arthroplasty (THA) [138]. Unfortunately, there are many mechanical complications regarding artificial joints and patients need at least one revision surgery which leads to other methods of treatment [138, 139, 140]. Alternatively, Core Decompression was developed which enables a healing of the femoral head in early stages of the disease, as well as low morbidity and low rate of complications [138]. Also nonoperative treatments are common, e.g., pharmacologic treatments, or biophysical therapies such as electromagnetic fields, extracorporeal shock waves, or reduced weight bearing (no or partial weight). However, Mont et al. [141] postulated in 1996 after investigating 819 hips treated with nonoperative management that such treatment should be discarded due to not-satisfying results. In general, non-operative treatment is only sufficient in very early stages of FHN and it can only slow down or even halt the progression of the disease [25].

2.3.2.1 Core Decompression

Core Decompression (CD) first was described by Ficat et al. [64] in 1977 and was a technique for diagnosing osteonecrosis of the femoral head. His procedure contains introducing a 6 to 8 mm drill into the area of necrosis starting from the lateral cortex of the greater trochanter. This enables a definitive histologic diagnosis of the necrosis. A

secondary effect was a decompression of the femoral head and 94% of the patients with Ficat stage I (1.3) disease showed good results. Additionally, this decompression permits venous drainage and relieved congestion [142]. Later, Kiaer et al. [143] discovered that intraosseous pressure is elevated and the partial pressure of oxygen is lower in patients with ON so that a core decompression seems to reverse these effects.

2.3.2.2 Advanced Core Decompression

Advanced Core Decompression (ACD) is similar to CD but, additionally, the necrotic areal is removed and filled up with autologous bone and substitute material. Wright Medical (Wright Medical Deutschland GmbH, Landsberg, Germany [144]) developed the X-REAM™, a tool to remove a spherical shape of necrotic area as illustrated in Figure 2.8. PRO-DENSE® (Wright Medical Deutschland GmbH, Landsberg, Germany) is a synthetic biomaterial to fill the removed area with an osteoconductive effect [145]. This substitute consists of calcium sulfate ($CaSO_4$) with calcium phosphate ($CaPO_4$) and has a compressive strength of approximately 40 MPa. [146] Urban et al. [147] investigated that, $CaSO_4$ with β-tricalcium phosphate (β-TCP) granules have bone-forming capabilities: $CaSO_4$is resorbed in the first six weeks, primarily through simple dissolution, to allow early vascular infiltration meanwhile $CaPO_4$ forms secondary porous scaffold that is condictive to vascular infiltration and bone formation and resorbed after $CaSO_4$ by osteoclasts. Resorption and remodeling processes operate in the first 6 month, the bone is fully remodeled after 6 to 12 month [146]. Landgraeber et al. [145] postulated in earlier studies a shorter rehabilitation time and a higher stability of the femoral neck after treating with ACD.

Figure 2.8: X-REAM™ of Wright Medical [144]

The whole procedure of ACD is shown by Wright Medical [148]: Nowadays CD is started using a 2 cm stab incision for access during fluoroscopic guidance (AP and LAT

view) as illustrated in Figure 2.9. The fluted guidewire is introduced into the lesion, which mostly is located at anterior and superior. Afterwards, the tissue protector is introduced. With a 9 mm cannulated drill bit, the femoral head is decompressed by drilling a core approximately 5 mm from the endosteal surface of the femoral head under fluoroscopic view. After drilling, the X-REAM™ is used to carried out advanced debridement as visible in the figure. The blades can be spread out and the necrotic area can be cleared. The left space must be filled now with autologous bone and bone substitute [148].

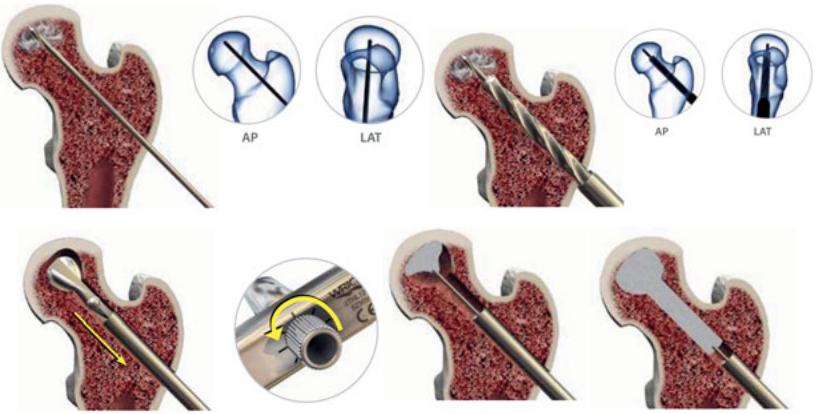

Figure 2.9: Advanced Core Decompression of Wright Medical [148]

This method rises the healing of the diseased bone extensively and, thus, avoids a THR. Furthermore, a shorter surgery time with around 60 min and smaller access of the hip are advantages [144, 148, 146]. The removal procedure must be performed with the goal to remove the highest amount of necrotic area to guarantee the healing of the hip and, hence, a successful surgery [149].

3 Materials and Methods

In this section the materials and methods used in this thesis are described. At the beginning, the theoretical model and the mathematics are presented. Subsequently, the procedure of motion analysis is shown, in particular the special methods for both diseases, FAI and FHN, are reported.

3.1 Theoretical Model

Solutions of engineering problems need a well-founded theoretical model. Important for FE models are exact CAD data, material properties, and the correct boundary conditions which have to be identified. This section describes the procedures, which are used in this thesis. First, the theory of the finite element method is described. Afterwards, both diseases including all investigation steps are mentioned. Furthermore, the contact modeling for the FAI simulations is explained. With focus on FHN, the force application and the material properties of cortical and cancellous bone is of importance.

3.1.1 Theory Finite Element Method

In the last decades, the finite element method (FEM) is well-established in many engineering processes such as mechanical engineering, construction of apparatus, and vehicle manufacturing [68]. A brief introduction to nonlinear structural mechanics is essential for all further investigations. The prediction of the physical behavior of a component after, e.g., loading, is possible using equations. For a complex geometry, this approach is limited. Thus, the basic concept of FEM is to divide this complex geometry into partitions, so-called elements with simple deformation behavior. All single solutions can be combined and a solution of the behavior for the whole system is predictable. The number of single solutions is finite, and hence, this method is called FEM . The elements are connected to nodes.

Solving structural problems using approximation methods, e.g., FEM, the internal and external forces need to be in equilibrium in a weak sense, which can be expressed by the principle of virtual work. This is considered by some as a statement of mechanics more fundamental than the traditional equilibrium conditions of Newton's laws of motion, while others state that the classical laws pertaining to the equilibrium of the particle [69]. Zienkiewicz et al. [69] reported that the virtual work statement is simply a weak form of equilibrium equations.

Basically, all numerical problems in the fields of engineering and physics, posed by an appropriate differential equation and boundary conditions, imposed by an unknown function u can be solved using the finite element method. The most general terms are

the differential equation $A(u)$ and the boundary condition $B(u)$ including the unknown function u [69]:

$$A(u) = \left\{ \begin{array}{c} A_1(u) \\ A_2(u) \\ \vdots \end{array} \right\} = 0 \tag{3.1}$$

$$B(u) = \left\{ \begin{array}{c} B_1(u) \\ B_2(u) \\ \vdots \end{array} \right\} = 0 \tag{3.2}$$

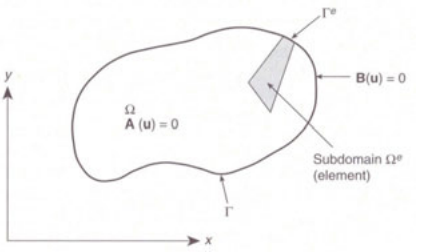

Figure 3.1: Problem Domain Ω and Boundary Γ [69]

Figure 3.1 illustrates the problem domain Ω including the boundary Γ, the differential equation $A(u)$, the boundary condition $B(u)$, the subdomain Ω^e, and the boundary of the subdomain Γ^e [69]. Searching for the solution, the finite element process will approximate

$$u \approx \hat{u} = \sum_{a=1}^{n} N_a \widetilde{u}_a = N\widetilde{u}, \tag{3.3}$$

where N_a are shape functions described in terms of independent variables and all or most of the parameters $\widetilde{u}_a$ are unknown [69].

In general, in a 3D continuum the equilibrium equations of an elementary volume can be written in terms of the components of the symmetric Cartesian stress tensor, where $b = \left[\begin{array}{ccc} b_x & b_y & b_z \end{array} \right]^T$ describes the free body forces acting per unit volume:

$$\left\{ \begin{array}{c} A_1 \\ A_2 \\ A_3 \end{array} \right\} = - \left\{ \begin{array}{c} \frac{\partial \sigma_x}{\partial x} + \frac{\partial \tau_{xy}}{\partial y} + \frac{\partial \tau_{xz}}{\partial z} + b_x \\ \frac{\partial \tau_{xy}}{\partial x} + \frac{\partial \sigma_y}{\partial y} + \frac{\partial \tau_{yz}}{\partial z} + b_y \\ \frac{\partial \tau_{xz}}{\partial x} + \frac{\partial \tau_{yz}}{\partial y} + \frac{\partial \sigma_z}{\partial z} + b_z \end{array} \right\} = 0 \tag{3.4}$$

In fields of solid mechanics, the six stress components will be functions of strain ε, which are computed using the displacement

$$u = \begin{bmatrix} u & v & w \end{bmatrix}^T. \qquad [69](3.5)$$

An arbitrary weighting function vector v is introduced to obtain a weak form

$$v \equiv \delta u = \begin{bmatrix} \delta u & \delta v & \delta w \end{bmatrix}^T. \qquad [69](3.6)$$

Since the set of differential equations (Eq. 3.1) has to be zero at each point of the domain Ω, it follows

$$\int_\Omega v^T A(u) d\Omega \equiv \int_\Omega [v_1 A_1(u) + v_2 A_2(u) + \cdots] \, d\Omega \equiv 0, \qquad (3.7)$$

where v is a set of arbitrary functions equal in number to the number of equations that are involved [69]. In a three-dimensional case, the equation is adjusted to include the volume Ω, which is the problem domain:

$$\int_\Omega \delta u^T A(u) d\Omega = -\int_\Omega \left[\delta u \left(\frac{\partial \sigma_x}{\partial x} + \frac{\partial \tau_{xy}}{\partial y} + \frac{\partial \tau_{xz}}{\partial z} + b_x \right) + \delta v (A_2) + \delta w (A_3) \right] d\Omega = 0 \qquad (3.8)$$

Each term is integrated by parts and after rearranging it, the following remains according to [69]:

$$\int_\Omega \left[\frac{\partial \delta u}{\partial x} \sigma_x + \left(\frac{\partial \delta u}{\partial y} + \frac{\partial \delta v}{\partial x} \right) \tau_{x,y} + \cdots - \delta u b_x - \delta v b_y - \delta w b_z \right] d\Omega - \cdots$$

$$\cdots \int_\Gamma [\delta u t_x + \delta v t_y + \delta w t_z] \, d\Gamma = 0, \qquad (3.9)$$

where t are tractions acting per unit area of external boundary surface Γ of the solid:

$$t = \begin{Bmatrix} t_1 \\ t_2 \\ t_3 \end{Bmatrix} = \begin{Bmatrix} n_x \sigma_x + n_y \tau_{xy} + n_z \tau_{xz} \\ n_x \tau_{xy} + n_y \sigma_y + n_z \tau_{yz} \\ n_x \tau_{xz} + n_y \tau_{yz} + n_z \sigma_z \end{Bmatrix}. \qquad (3.10)$$

The first set of bracketed terms in Eq. 3.9 shows the small strain operators acting on δu, which termed a virtual displacement (or virtual velocity) [69]. Introducing a virtual strain defined corresponding to Zienkiewicz et al. [69] as

$$\delta \varepsilon = \begin{Bmatrix} \frac{\partial \delta u}{\partial x} \\ \frac{\partial \delta v}{\partial y} \\ \frac{\partial \delta w}{\partial z} \\ \frac{\partial \delta u}{\partial y} + \frac{\partial \delta v}{\partial x} \\ \vdots \end{Bmatrix} = S \delta u, \qquad (3.11)$$

where the strain operator ε is:

$$\varepsilon = Su. \tag{3.12}$$

Afterwards, the six stress components can be arranged in a vector σ corresponding to Eq. 3.11, the Eq. 3.9 can be simplified to

$$\int_{\Omega} \delta\varepsilon^T d\Omega - \int_{\Omega} \delta u^T b d\Omega - \int_{\Gamma} \delta u^T t d\Gamma = 0, \tag{3.13}$$

which is the 3D equivalent virtual work corresponding to Zienkiewicz et al. [69]. As it can be seen, the virtual work statement precisely is the weak form of equilibrium equations and is, hence, valid for non-linear as well as linear stress-strain relations [69]. It is assumed that the shape functions N include all independent coordinates of the problem and that $\widetilde{u}$ was simply a set of constants by using the approximation to the problem of solving the differential equation 3.1 by an expression of the standard form of Eq. 3.3 [69]. A unique set of parameters can be determined using the final approximation equations due to the present algebraic form [69]. With the use of independent variables, e.g., x, y, and z, it can be assumed that all parameters $\widetilde{u}$ are functions of z and, thus, the approximation is only performed in the domain of x, y, $(\bar{\Omega})$ and, hence, the Equation 3.3 is simplified to:

$$u = N(x, y)\widetilde{u}(z). \tag{3.14}$$

After the final discretization, the derivatives of $\widetilde{u}$ with respect to z will remain and the result will be a set of ordinary differential equations with z as the independent variable, e.g., in linear problems the equation is

$$K\widetilde{u} + C\dot{\widetilde{u}} + \cdots + f = 0 \tag{69}(3.15)$$

with $\dot{\widetilde{u}} \equiv d\widetilde{u}/dz$. This partial discretization can be used in different ways, especially, when the domain $\bar{\Omega}$ is independent on z, e.g., when the problem is prismatic. For more extensive reviews in the field of basis and fundamentals of the finite element method, the reader is referred to corresponding literatures, e.g., Zienkiewicz et al. [69], Holzapfel [150], Klein [68], Rust [151], and Bonet and Wood [152].

Additionally, the basic equation of motion is:

$$M * \ddot{u}(t) + D * \dot{u}(t) + K * u(t) = f(t) \tag{3.16}$$

(M : Massmatrix; D: Dampingmatrix; K: Stiffnessmatrix; f: Load; u: Displacement)

If Ω is the frequency of the excitation, the term expands to:

$$M * \ddot{u}(t) + D * \dot{u}(t) + K * u(t) = f * e^{j\Omega t}. \tag{3.17}$$

Hence, the used simulations are linear, stationary, and static problems in which single loadsteps are evaluated. Therfore, the mass and damping terms can be neglected. Thus, the remaining equation is:

$$K * u(t) = F. \tag{3.18}$$

(F: Force; K: Stiffness; u: Displacement)

Every element can be solved using this equation, also known as spring equation, and each node ensues three unknowns, the displacements in all three directions. The displacement for each node is solved using an iterative or direct solver. By including material properties, stresses can be calculated based on the displacement [153].

There are several types of solvers, which are used to solve simultaneously equations of a system: sparse direct solution, Preconditioned Conjugate Gradient (PCG), Jacobi Conjugate Gradient (JCG), Incomplete Cholesky Conjugate Gradient (ICCG), and Quasi-Minimal Residual (QMR). Furthermore, distributed versions of named solvers are available [154]. The Sparse Direct Solver is based on a direct elimination of equations, which requires the factorization of an initial very sparse linear system of equations into a lower triangular matrix followed by forward and backward substitution using this triangular system [154].

In contrast, iterative solvers successively refine an initial guess to a solution, e.g., the Preconditioned Conjugate Gradient (PCG), which are not further discussed because they were are unused in this dissertation.

Table 3.1: Typical Applications for Sparse Direct Solver [154]

Solver	Typical Applications	Ideal Model Size
Sparse Direct Solver (direct elimination)	When robustness and solution speed are required (nonlinear analysis); for linear analysis where iterative solvers are slow to converge (especially for ill-conditioned matrices, such as poorly shaped elements).	100,000 DOF (and beyond)
Preconditioned Conjugate Gradient Solver (iterative solver)	Reduces disk I/O requirement relative to sparse solver. Best for large models with solid elements and fine meshes. Most robust iterative solver in ANSYS.	500,000 DOF to 20 MDOF+
Jacobi Conjugate Gradient Solver (iterative solver)	Best for single field problems - (thermal, magnetics, acoustics, and multiphysics). Uses a fast but simple preconditioner with minimal memory requirement. Not as robust as PCG solver.	500,000 DOF to 20 MDOF+
Incomplete Cholesky Conjugate Gradient Solver (iterative solver)	More sophisticated preconditioner than JCG. Best for more difficult problems where JCG fails, such as unsymmetric thermal analyses.	50,000 to 1,000,000+ DOF
Quasi-Minimal Residual Solver (iterative solver)	High-frequency electromagnetics.	50,000 to 1,000,000+ DOF

The setting of the solver selection is set to *program controlled*. For both, the FAI and FHN, the Sparse Direct Solver is used due to the high robustness and the nonlinear analysis as visible in Table 3.1. The other solvers are used for different simulations.

FEM is an approximation procedure. If a calculation approximates to a boundary value with increasing mesh quality, it is called convergence. However, if with increasing mesh quality, the stress value also still increases, it is called divergence.

An absolute accuracy of FE simulations is impossible, only the accuracy of the mesh quality is predictable, but FE simulations show well conformity with the reality. The correctness of boundary conditions and material properties are very important to ensure proper results of simulations. The results of a simulation should always be compared to the reality.

Contact modeling of such problems is essential to get acceptable results. The definition

of a contact is, if a body approaches an arbitrary surface during a movement and is stopped, thereby. A deformation is also possible depending on the material properties of the connecting bodies. Two bodies without any common elements can be defined as a bonded contact if they lack of relevance for the calculation [151].

A good contact modeling in this dissertation is important to prevent an intersection between body parts. In the FAI study, the connection between femur and acetabulum, and femur and labrum is with friction, while the connection between acetabulum and labrum is fixed as illustrated in Figure 3.2. The friction coefficient in biomechanic problems is $\mu = 0.01$, as described in Kotz et al. [155]. The contact in this problem is unknown, i.e., if there is any contact between the bony parts and when, at which position. The classification of this contact problem is set to *program controlled*. A generous contact surface selection should be performed, because it is uncertain at which exact point a contact will occur. In general, a complete irrelevant surface should not be selected to ensure the shortest simulation time.

Figure 3.2: Contact Modeling in ANSYS

The contact modeling is often very complicated and it is recommended to use the *Program Controlled* setting of ANSYS. For the FAI, it suffices to check, if there is a contact. Different contact algorithms are usable, e.g., *Penalty method*, *Augmented Lagrange*, *Normal Lagrange*, and *Multi-Point Constratint (MPC)*. The two main algorithms are briefly explained in this thesis. *MPC* disallows penetration wherefore it is infeasible to be integrated in this dissertation.

The Penalty algorithm uses mathematical optimization. For this purpose, it introduces a force at the contact point which is penetrated across the surface of the target part to disable a penetration. In this respect, statistical balance is reached if the potential energy is minimal, i.e., as long as the contact is not reached, the potential energy is the following [151]:

$$W = \frac{1}{2}ku^2 - uF \rightarrow Min. \tag{3.19}$$

If this condition is interfered, another term is added, which increases the energy. Any violation of the contact condition is punished by increasing the total virtual work. This results in the name penalty. [156] A term is considered a "penalty" due to the violation and the equation changes to:

$$W = \frac{1}{2}ku^2 - uF + \frac{1}{2}\varepsilon g^2(u) \rightarrow Min. \tag{151}(3.20)$$

with penetration g including ε, the penalty parameter.

The contact force of the Penalty algorithm with contact stiffness k_N [157]:

$$F_N = k_N g \tag{3.21}$$

The minimum is reached if the following equation is set to zero including the relative deformation $\triangle x$:

$$\frac{\partial W}{\partial u} = \frac{\partial}{\partial u}\left[\frac{1}{2}ku^2 - uF + \frac{1}{2}\varepsilon(\triangle x - u)^2\right] = 0 \tag{3.22}$$

$$ku - F - \varepsilon(\triangle x - u) = 0$$

$$ku - F - \varepsilon\triangle x - \varepsilon u = 0$$

$$(k + \varepsilon)u = F + \varepsilon\triangle x$$

$$u = \frac{F + \varepsilon\triangle x}{k + \varepsilon} \tag{151}(3.23)$$

In case of penetration, i.e., $g < 0$, the result is $F > k\triangle x$ [151]. The contact condition is fulfilled, if the Penalty Parameter converges to infinity, however, on grounds of numerical terms it will converge. This results in a remaining penetration of g [151]:

$$g = \left(1 - \frac{1.5k + \varepsilon}{k + \varepsilon}\right) \triangle x \tag{3.24}$$

Furthermore, it is important to update the contact stiffness after each iteration, because a certain penetration must be allowed, which is dependent on the contact stiffness. This must be chosen in such a way that the amount of status-changes remains small, which enables a small contact stiffness. However, the penetration should be as small that stresses and deformations of adjacent elements are not incorrect which enables a great contact stiffness. The contact stiffness should be chosen significantly greater than the stiffness of the adjacent systems. The system stiffness only can be determined by solving the FE-terms. Importantly, a contact leads to greater deformations [151].

Other contact algorithms are also possible such as *Lagrange*, which is not advisable due to the robustness during penetration/contact and the fact that for symmetric contacts and boundary conditions, the equation system is over-constrained [156]. The Lagrange method adds the term

$$\lambda g(u) \tag{3.25}$$

instead of the Penalty-term to the potential energy, such that the modified potential energy with the Lagrange multiplier λ results in [151]:

$$W = \frac{1}{2}ku^2 - uF + \lambda g(u) \rightarrow Min. \tag{3.26}$$

The main difference between both contact models is the calculation of the contact force. In the following, the contact force of the Lagrange algorithm is:

$$F_N = k_N g + \lambda. \qquad [157](3.27)$$

The extra term λ is the reason for the lesser sensitivity of the contact stiffness k_N [157].

The minimum is now reached if:

$$\frac{\partial W}{\partial u} = ku - F + \lambda \frac{\partial g}{\partial u} = 0 \tag{3.28}$$

which can be iteratively transformed to

$$\hat{}\frac{\partial W}{\partial \lambda} = g(u) = 0$$

$$ku - F - \lambda = 0$$

$$\hat{}\triangle x - u = 0 \qquad [151](3.29)$$

The second equation yields to

$$u = \triangle x, \qquad (3.30)$$

which leads after insertion in the first equation to:

$$\lambda = k\triangle x - F \qquad (3.31)$$

and that the Lagrange multiplier is equal to the contact force [151].

Extensions of the algorithm include, e.g., *Perturbed-Lagrange* or *Augmeted-Lagrange*. In this dissertation these extensions are not introduced due to the fact that the Lagrange algorithm did not converge, when setting the penetration to zero as visible in Figure 3.3.

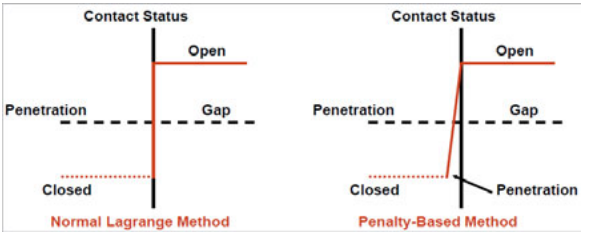

Figure 3.3: Schematic Diagram of Normal Lagrange Method and Penalty-Based Method [157]

The meshing is very important to obtain realistic simulation results. A poor mesh quality may cause a poor solution accuracy after simulation termination or a convergence problem can occur [158]. Meshing is the dissection of the whole geometry in simple describable elements [153]. For this reason, an adjustment of the correct settings for each

model is necessary. Different settings are possible to ensure the meshing quality, which is controllable using software intern tools, e.g. skewness. If there are single elements with improper quality, it is important to check where these are located, e.g. for the FAI project there should not be any elements with a poor quality in the contact area.

Another essential factor to develop correct simulation results are material properties. Using linear analysis the material properties are induced using the Hooke's law

$$\sigma = \varepsilon \times E, \tag{3.32}$$

which corresponds to the beginning of the stress-strain diagram [153]. However, if stresses occur during the analysis above the liquid limit, the right material behavior cannot be described using linear material properties anymore, because the material's property weakens, e.g., steel. Stresses increase slower and deformation increases, which necessitate another material law [153].

3.1.2 Motion Analysis

During the investigation of the patients, the attending physician determines the range of motion (ROM) of the affected hip joint. Additionally, the impingement test is performed to examine if the patient has pain during this particular movement. The investigation is performed in dorsal position, every movement is conducted three times.

Three rotational movements of the hip joint are investigated separately to determine the ROM. The leg is positioned in the neutral-zero-position and moved to the five rotational possible movements: flexion, internal and external rotation, abduction and adduction. The extension is not possible due to the dorsal measurement, but it is irrelevant for FAI mechanism. This test is separated into 5 stages visible in Figure 3.4:

- In stage one, the leg is moved to the body, flexion (x-axis).
- In stage two, the internal rotation is performed, the femur is moved around its axis (z-axis). To simplify this movement for the physician, hip joint and knee joint are flexed at 90°. The lower leg can be rotated until the maximum angle is reached.
- Stage three defines the external rotation and is similar executed like the internal rotation but the lower leg is moved inside to the body.
- In stage four, the rotation around the y-axis is conducted: abduction until the maximum angle is reached.
- The last stage, five, is the contrary movement: adduction. This movement is similar to the abduction, but in direction of the patient.

- Furthermore, the impingement test is performed to provoke an impingement of the joint parts. Pain, which potentially occurs, can be detected using the developed pain sensor, a differential pressure cell. If pain occurs, the test is positive and the patient probably suffers from a FAI. The movement contains internal rotation with a current flexion [108].

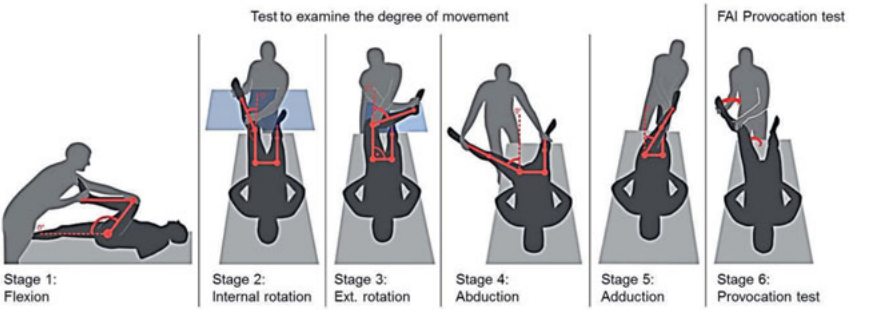

Figure 3.4: Stages of Motion Analysis [108]

3.2 Femoroacetabular Impingement

An investigation of FAI requires extensive pre-processing, e.g., determination of degree of movement, good quality MRI data etc. In the following, several methods are explained, which are performed in this study.

3.2.1 Clinical Investigation of Degree of Movement

The clinical investigation of the degree of movement is essential to diagnose some limitations of movement. The physical examination is performed by the medical doctor and separated into six basic stages: flexion, abduction/adduction, internal-/external rotation, and a FAI provocation test to ensure a possible contact between proximal femur and acetabular rim.

FAI patients have a limited range of motion, flexion, adduction and internal rotations are mainly affected [159, 160]. The physical examination should contain height, weight, and overall fitness level of patients [159]. The Impingement test is essential during a clinical investigation by a surgeon: During this test, the patient is lying in a dorsal position and the affected leg is moved internally rotated, adducted at 90° and flexed. The bony deformity impinges on the acetabular rim and causes a groin pain [132]. Hence, a specific attention is paid to the amount of internal rotation with a flexed hip [159]. Additionally, other tests

can be performed to validate the diagnosis, e.g., Apprehension test, FABER test, Dial test, and leg roll test, which are not used in this study and, hence, not deepened [14].

Furthermore, the complete range of movement for flexion, abduction, adduction, internal rotation and external rotation is determined. This complete investigation is recorded using 13 MX13 cameras of Vicon Nexus (Nexus, Vicon, Oxford, UK) in the gait lab. During this investigation, the patient is covered with reflecting markers to get the full range of motion for the patient's affected hip as shown in Figure 2.3 in section 2.2.2.1.

The markers are placed according to the plug-in gait lower-body model except of the back marker which cannot be placed because the movement is performed in a dorsal position. During the measurement, the patient's leg is moved from the neutral position in all six stages considering pain. The marker on the back cannot be placed due to the dorsal measurement why it is shifted [110]. For this study, the lower-body is marked using 16 marker as visible in Figure 2.4 in section 2.2.2.1. Furthermore, the width of ankle and knee joint are recorded as additional anthropometric data. The hip joint center is determined using the marker LASI, RASI, LPSI and RPSI and the Newington-Gage model [161]. The other joint centers are calculated using the hip joint center [108].

The maximum rotational angles are recorded by the Motion Capture system. These data are important for further investigations of the mobility of the hip and for comparison between pre- and post surgery.

3.2.2 Generation of the Computational Domain (MRI)

The data generated by the magnetic resonance imaging (MRI) are DICOM files which have to be switched into volumina for the multi-body and FE simulations, which is the medical standard format developed by the National Electrical Manufactures Association (NEMA) for image data including secondary information [162]. The MRI used in this study is the Magnetom Aera with 1.5 Tesla (Siemens, Munich, Germany) and the 4G-TIM (Total Image Matrix) technology. The slice thickness is 1.5 mm.

The segmentation software used in this thesis is MIMICS® (v16.0-18.0, Materialise, Löwen, Belgium) as visible in Figure 3.5. The MRI data is loaded into the software and arranged in position, to ensure the view of the data in all position.

The procedure of segmentation is to select the area of importance in each slice. MR images have no further information about the density compared to CT data which is the reason for the manual segmentation. CT data can be handled by several automatic solutions such as thresholding etc. An advantage of MR data is the soft tissue which is also recorded and thus, the labrum etc. can be segmented. In Figure 3.6 an example of MRI- and CT data used in this study is shown.

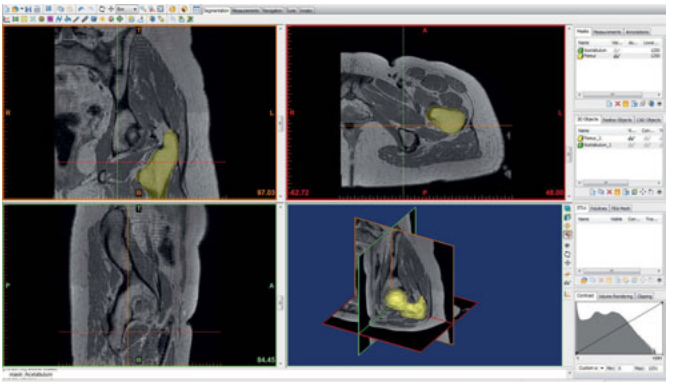

Figure 3.5: Graphical User Interface of the Software MIMICS®

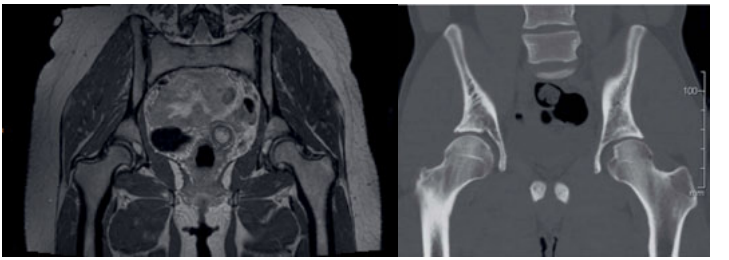

Figure 3.6: MRI (left) CT (right)

The used slice thickness is 1.5 x 0.9 mm per pixel. Different masks are used in MIMICS® to separate the different parts e.g. femur, acetabular and labrum. In cooperation with the university hospital a mostly exact bone model is developed which is extracted in the STL format (Stereolithography), a data type and an interface between CAD software. The position of the bones and the coordinate-systems still remains what enables a correct and exact positioning. The MRIs are performed in neutral position. Therefore, the leg is fixed to prevent a rotation in the hip model.

The existing STL (Stereolithography) format is a neutral format to store three dimensional geometric information. The surface geometry of a 3D object is stored without any representation of color, texture or other common CAD model attributes [163]. The surfaces of an CAD model are described with unstructured triangulated surfaces and the normal vector. Unfortunately, the quality of these models is dependent of the slice thickness and, of course, irregularity can occur which requires a post-processing e.g. smoothing. The difference between pre- and post-processing is visible in Figure 3.7.

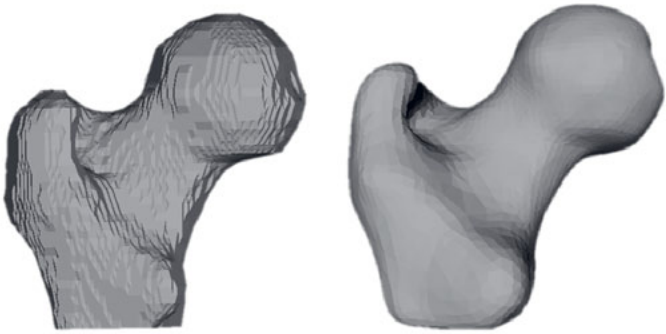

(a) unedited (b) smoothed

Figure 3.7: Smoothing using MeshLab

This post-processing is performed with the open source software MeshLab (v1.3.3, P. Cignoni, Pisa, Italy) [164]. The hip models are smoothened regarding the desired accuracy.

The surfaces are reconstructed using the Poisson method [165]. Therefore, the function in *Filters* → *Remeshing, Simplification and Reconstruction* → *Surface Reconstruction: Poisson* is used. If the values of *Octree Depth* and *Solver Divide* are high, the calculation achieves more exact results with a higher quality but also requires significant more calculating time. The values of *10* and *8* promise reasonable results. The parameter *Samples per Node* should remain 1, because higher values produce higher smoothing results which also affects the volumina. The function *Surface offsetting* adds volumina which is lost by smoothing. A value of *1* configures that nothing is added, but given a value of *0.999999* more material is added. This procedure is depended on the manual segmentation.

Facets can be reduced in the areas of no interest to ensure short processing times. This can be performed using the function *Filters* → *Remeshing, Simplification and Reconstruction* → *Quadratic Edge Collapse Decimation*. Subsequently, a mesh repairing procedure is performed. The corner points which are nearer than a given value are merged. (*Filters* → *Cleaning and Repairing* → *Merge close Vertices*). A similar correction is performed for edges and facets. (*Filters* → *Cleaning and Repairing* → *Snap mismatched Borders*). If the model has so called T-Vertices, which are groups of facets with an edge of one facet that is divided through two adjacent facets, problems may occur during the procedure. Hence, this information is removed (*Filters* → *Cleaning and Repairing* → *Remove T-Vertices by Edge Flip*). Exact same facets will be eliminated using *Filters* → *Cleaning and Repairing* → *Remove Duplicate Faces*. The same procedure is performed for double corner points (*Filters* → *Cleaning and Repairing* → *Remove Duplicated Vertexes*). All facets with an surface area of zero and the disengaged corner points are deleted (*Filters*

→ *Cleaning and Repairing* → *Remove Zero Area Faces, Filters* → Cleaning and Repairing → Remove Unreferenced Vertex).

The MeshLab function *Show Layer Dialog* shows the results of each step. The corrected model can be exported and stored as STL-File. The last step is the compilation in an volume model which is achieved by using the open source software FreeCAD (v0.14, J. Riegel, Ulm, Germany). This step is only possible, if there are no errors in the mesh.

Additionally, a second software CATIA (v5, Dassalt Systèmes, Vèlizy-Villacoublay, France) was used to smoothen and converse the geometry. This software uses a NURBS method to reconstruct the surfaces. First, the STL file was imported into CATIA and the function *Flip Edges* is used followed by the tool *Mesh Smoothing*. *Mesh Cleaner* is applied to check whether there are any issues with the mesh, hence, the tool *Fill Holes* is approached before reconstructing the surfaces. Afterwards, the surface of the model is smoothed by using the tool *Quick Surface Reconstruction*, as visible in Figure 3.8.

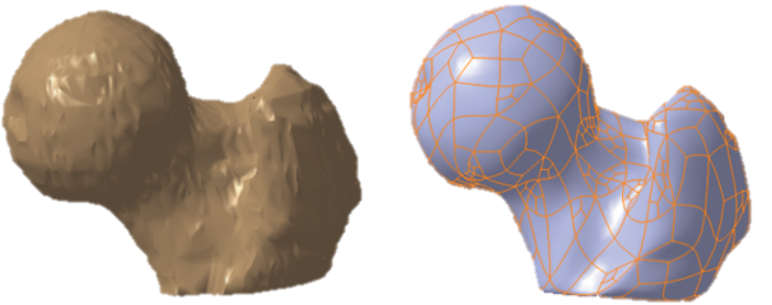

(a) unedited (b) smoothed

Figure 3.8: Smoothing using CATIA

Finally, the solid model is generated using the tool *Close Surface* and exported into a STEP file (Standard for the Exchange of Product model data), which allows the usage of the model for the simulations. All steps in CATIA are performed using default settings.

3.2.3 Important Parameter of the Hip Joint

Several patient specific parameters of the hip joint are necessary to simulate the movement of the hip joint. New methods are required to find the hip joint center, the hip head diameter and the femoral neck axis.

3.2.3.1 Determination of the Hip Joint Center

The movement simulation of the hip is controlled using angles which are determined in the motion analysis, the hip joint center (HJC) is essential to rotate the model around the center. Slight deviations can accrue great errors, e.g., rotation of the hip joint etc. and probably the impingement contact of a patient is not correctly calculated. Determination of the mass points using CAD software Creo Parametric (v3.0, PTC, Needham, Massachusetts, USA) is rather difficult because the selection of only the femoral head is very inaccurate. More exact methods are needed, such as an adjustment of a ball which is often described in literature [166, 167, 168]. In this work, several methods are developed to ensure the most precise result of the coordinates for the HJC. A viable method is the calculation of the HJC using the marker of the motion capture system. In the last years, several concepts were developed using experiential or mathematical approaches [169].

A comparison between a motion capture and a simulation model is only possible by using markers in the MRI. Unfortunately, the lying position of the patient in the MRI makes a complete marking complicated, so only two relevant markers can be placed ${}^{MRI}M_1$ and ${}^{MRI}M_2$ which corresponds to an insufficient amount of data points to rely on the mathematical approach. However, a vector ${}^{MC}M_1$ to ${}^{MC}HJC$ can be extracted from the motion capture system and integrated into the calculation. The recommended way for the determination is in the lying position during the motion capture analysis, because it is the same position as during the MRI. For the purpose to ensure that vector ${}^{MC}\bar{v}_{M1\rightarrow HJC}$ is correct, it is necessary to control both coordinate systems on the same orientation. For all views, the vector $\bar{v}_{M1-M2}$ of the markers is required to extract the unit vector by using the absolute vector $|\bar{v}|$:.

$$\bar{e} = \frac{\bar{v}}{|\bar{v}|} \tag{3.33}$$

Using both unit vectors ${}^{MC}\bar{e}_{M1\rightarrow M2}$ and ${}^{MRI}\bar{e}_{M1\rightarrow M2}$, the rotation matrix ${}^{MRI}R_{MC}$ is computed which contains the differences in the orientation [170]:

$${}^{MRI}R_{MC} = \begin{bmatrix} \bar{e}_{x_{MRI}} \cdot \bar{e}_{x_{MC}} & \bar{e}_{x_{MRI}} \cdot \bar{e}_{y_{MC}} & \bar{e}_{x_{MRI}} \cdot \bar{e}_{z_{MC}} \\ \bar{e}_{y_{MRI}} \cdot \bar{e}_{y_{MC}} & \bar{e}_{y_{MRI}} \cdot \bar{e}_{y_{MC}} & \bar{e}_{y_{MRI}} \cdot \bar{e}_{z_{MC}} \\ \bar{e}_{z_{MRI}} \cdot \bar{e}_{z_{MC}} & \bar{e}_{z_{MRI}} \cdot \bar{e}_{y_{MC}} & \bar{e}_{z_{MRI}} \cdot \bar{e}_{z_{MC}} \end{bmatrix} \tag{3.34}$$

Thus, the vector can be matched with the MRI coordinate system:

$${}^{MRI}\bar{v}_{M1\rightarrow HJC} = {}^{MRI}R_{MC} + {}^{MC}\bar{v}_{M1\rightarrow HJC} \tag{3.35}$$

The final coordinates of the HJC are calculated using the ${}^{MRI}M_1$

$${}^{MRI}HJC = {}^{MRI}M_1 + {}^{MRI}\bar{v}_{M1\rightarrow HJC} \tag{3.36}$$

Another method to determine the HJC is the *circle method* with the use of circles in different layers of each direction of the coordinate system. These circles have to be manually fit using a CAD software such that the sphericity of the femoral head is fitted. All layers are generated in each of the three directions with distances of 6 mm as it is visible in Figure 3.9. In each of 18 layers, a circle is generated such that it fits into the femoral heard (diameter and center). 18 center points are determined in this way, further the arithmetic mean is calculated and the final hip joint center can be calculated.

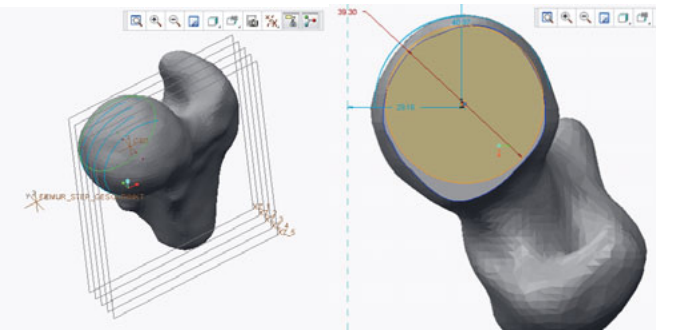

Figure 3.9: Circle-Method to Determine the HJC

An additional possibility to determine the HJC is the use of the coordinates, which are needed to measure the femoral head diameter. MIMICS® saves the coordinates of the center and can export them into a text file. Since the diameter is measured in six different angles, the average of all coordinates from each direction is calculated and the input as the coordinates of a single point, the HJC, in a CAD software as visible in Figure 3.10. The reference of this point is the coordinate system of the femur.

The last possibility for the HJC determination is the *sphere-fitting-method* whereby a sphere is fitted into the femoral head. The goal of this method is to parameterize the parameters of the sphere such that the distances to the femoral head are minimal. First, a layer is generated using Creo which is near the middle of the femoral head. All distances to the origin are defined as parameters. A semi circle is generated such that the femur adjoins it also with a diameter and distances as parameters. With the rotation of this semi circle, the sphere is generated. Afterwards, design-points are generated on the surface of the femoral head. The more points are generated, a more exact result of the determined HJC can be determined, but this procedure is also time-consuming why only 25 points were seeded. The tool *Feasibility/Optimization* in Creo is used to change the radius such that the distance between the points and the sphere is minimal. A good trade-off between calculating-time and exact results must be found (variations = 3000).

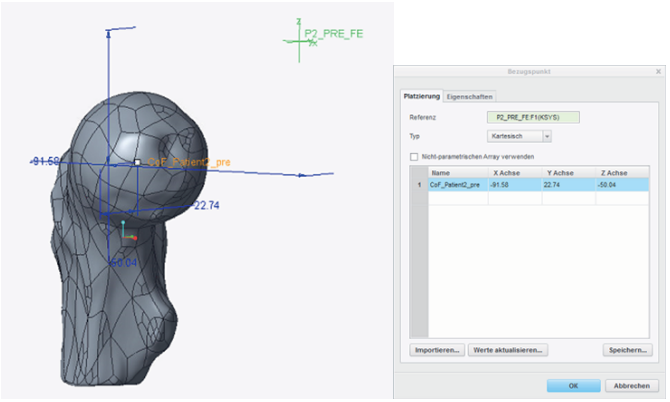

Figure 3.10: MIMICS® method to Determine the HJC

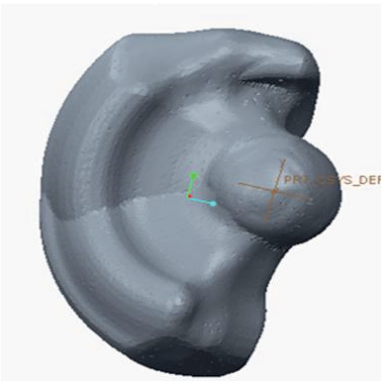

Figure 3.11: Motion Envelope Tool to Determine the Quality of the HJC

To control the quality of the HJC, a special function in Creo is used called motion envelope as described by Westermaier [171]. Goal of this tool is to move the femur around the developed HJC and save all generated areas in a new component, the motion envelope. A visual control is now possible as the femoral head should still be round after the movement (cf. Figure 3.11).

3.2.3.2 Determination of the Hip Head Diameter

The Hip Head Diameter (HHD) is a very important parameter for the determination of the impingement. Here, the method to determine the HJC is essential, because the sphere-fitting method has the advantage that the diameter of the head is saved as a parameter during the determination of the HJC. However, if the circle method described

in section 3.2.3.1 was used to determine the HJC, it is still possible to determine the head diameter with constructive effort. Several planes are generated through the HJC and in every plane, circles are drawn such that they tangent the edges of the femoral head. By calculating the average of these circle diameters, the final HHD can be determined.

3.2.3.3 Construction of the Femoral Neck Axis

For evaluation of the cam-type impingement, HJC and femoral neck axis (FNA) are of great importance. For designing this axis, Creo is used. For this purpose, a layer is defined which should be positioned in the area of the femoral neck axis. Additionally, another layer is placed in the xz-plane referring to the HJC as illustrated in Figure 3.12.

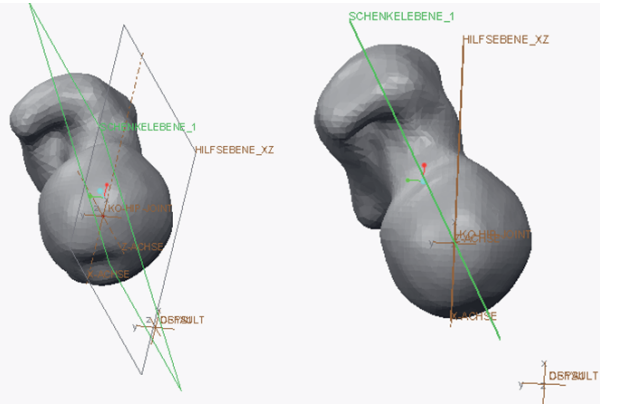

Figure 3.12: Construction of the Femoral Head Axis

The next step is to draw an axis through the HJC and the supposed femoral neck axis. For the correct position, another construction circle is drawn which tangents the edges of the femoral neck which is visible in Figure 3.13. For this purpose, this drawing has to be saved as a part. A correction of this procedure is performed. Furthermore, another plane is generated orthogonal to the previously saved part. In this plane, a drawing (ellipse or circle) is generated which also tangents the femoral neck. The origin of this drawing is the wanted construction point for the femoral neck axis. Afterwards, this point and the HJC built the femoral neck axis. An evaluation of the found FNA can be performed comparing the distanced between the FNA and the surfaces of the femoral neck. Nearly the same procedure is necessary to determine the alpha-angle, which is described in the following subsection.

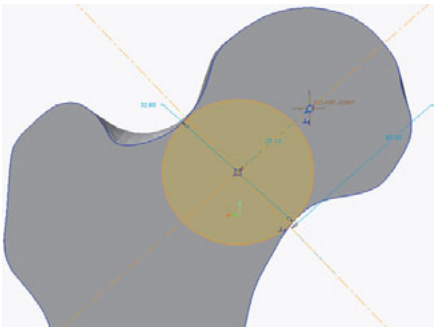

Figure 3.13: Construction of the Femoral Neck Axis

3.2.3.4 Alpha Angle

The Alpha angle is an important factor to determine the bony deformation in case of cam-type impingement. For this purpose, the convention of a clock face is necessary. Several planes have to be placed through the femoral head and the FNA which are rotated by about 30°. As reference, a plane 12/6 o'clock is essential for a sensible analysis which is placed through the FNA and the z-axis of the HJC (brown visible in Figure 3.14).

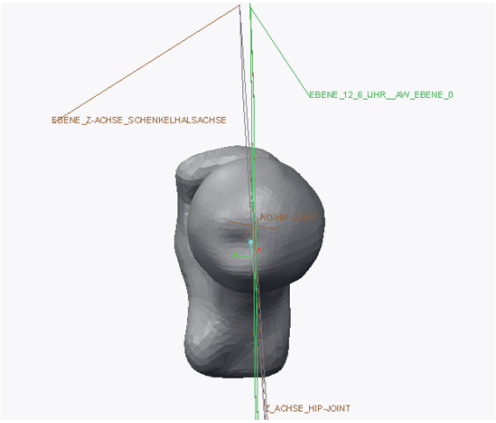

Figure 3.14: Example of Construction of the 12/6 o'clock Plane (green)

Thus, this plane is not parallel to the corpus femoris, the 12/6 o'clock can be determined by rotating around the FNA. Another five planes can be generated to determine the Alpha angle all around the femur as visible in Figure 3.15.

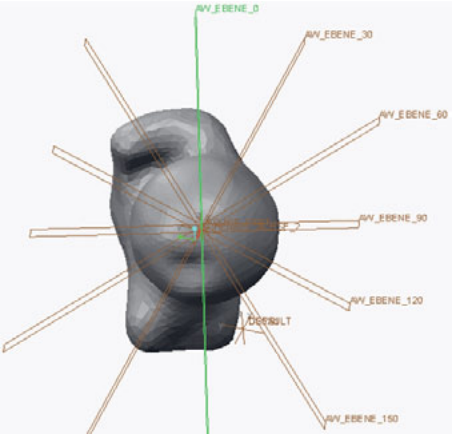

Figure 3.15: Construction planes for the Alpha Angle [171]

The determination of the Alpha angle is done in all planes. After consulting the attending doctor, the HHD is drawn in each plane, which is necessary regarding the inaccurate spherical geometry of the femoral head otherwise the angle values are inaccurate. The fitting accuracy of the HHD shows the quality of the founded HJC, in addition. For determining the alpha angle, two auxiliary lines through the HJC are drawn in which the spherical geometry is lost visible in Figure 3.16, the so-called bony deformity. Both angles between FNA and the auxiliary lines are measured.

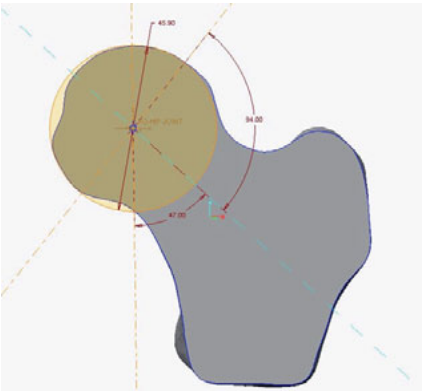

Figure 3.16: Construction of the Alpha Angle

Using these important hip joint parameters, the degree of movement for the hip joint can be described.

3.2.4 Pre-Operative Simulation of Patient-Individual Hip Joint Models

An investigation of the pre-operative degree of movement is performed using CAD-software and FEM-software to compare the results with each other. FEM software has the advantage to get additional information about occurring stresses, which can predict a failure of bone.

In the Table 3.2 the patient data are presented.

Table 3.2: Patient Data

Patient	Surgery	Age	Gender	Affected Hip
1	pre	24	m	right
2	pre	31	m	right
3	pre	52	f	right
4	pre	27	m	right
5	pre	31	f	both
6	pre	34	f	left
7	post	32	f	both
8	post	28	m	right

3.2.4.1 Geometric Simulation (CAD-Software)

For multi-body simulations using the CAD software Creo Parametric coordinate systems in both bones acetabulum and femur must be inserted at the position of the HJC according to the neutral position. A new component assembly is generated with the acetabulum in standard orientation. New studies of Kapron et al. [172] show a slight movement of the acetabulum while the femur is moved to the maximum possible angle. An investigation of this phenomena is not implemented in this study, because the required measurement of the matching acetabulum movement has to be performed, in addition. In this study, the movement of the hip joint is simplified by an only moving femur and the acetabulum is placed rigid. For the integration of the femur, the coordinate system of the HJC is used. The function *Gimbal* is used for the movement of the hip joint as visible in Figure 3.17.

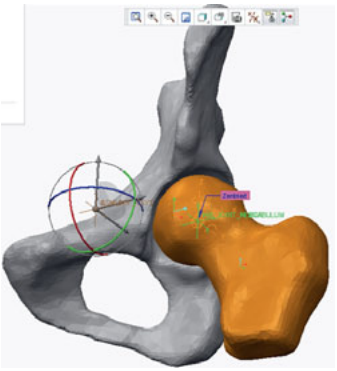

Figure 3.17: Gimbal Function in Creo

Servo motors are used to simulate the movement of the hip joint. Function *Mechanism* → *Play* is used to evaluate the motion sequence. Subsequently, a collision check is performed to analyze the contact between both bones, acetabulum and femur. The intersection status is controlled by Creo and an acoustic signal is given if a contact occurs. Furthermore, the collision parts are colored red, which is visible in Figure 3.18.

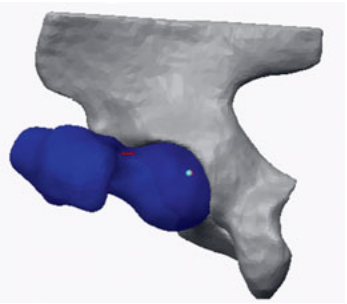

Figure 3.18: Simulation of a Collision with Creo (Collision Area is colored red)

Using this procedure it is simple to check, if the patient suffers from a bony impingement or not.

3.2.4.2 Finite Element Simulation

FEM simulations are performed because of the essential advantage that stresses and resulting deformations are additionally calculated, when compared to CAD simulations, which necessitates more time for the calculation. The software used for the simulation is ANSYS (Workbench v16.0, ANSYS, Canonsburg, Pennsylvania, USA). In the following,

the single steps for the mechanical analysis are explained. For the FAI simulations, only the kinematics are important and, thus, additional forces are negligible. The bones are fitted to the most important regions to reduce calculation time.

Realistic presentation of stresses and deformation using a simulation is only possible by implementing realistic material properties. Both bones mostly consist of cancellous and cortical bone, which makes the definition difficult. Unfortunately, MRI data have no additional information of the density, which massively hinders the classification of the relative parts. Every human being is different and so are the bones. The bones adapt to the stresses, which a human performs during life [173]. Liska et al. [173] also compare the nature to Mechanical Engineering, the human skeleton, which is developed with a hollow construction to ensure high bending stiffness by low weight.

For an exact mechanical model of the human hip, the bones have to be separated into both, cancellous and cortical, parts populated with different material data. Additionally, the properties of the different loading directions have to be considered. However, this thesis only shows the biomechanical procedures, which are the reasons for pain and limitation of movement by FAI. Therefore, the contact modeling is more important and the complex segmentation procedure of cortical and cancellous bone can be neglected, which would cause additional errors.

For the FAI, the Pure-Penalty-Algorithm is used to simulate the contact between acetabulum/femur and femur/labrum due to its multi-functional usability as described by Gebhardt [153]. The contact stiffness is essential here: A small intersection is a result of a high contact stiffness value, which can result in a divergent simulation. A small contact stiffness value will lead to wrong tensions, stresses and displacements such as described in 3.1.1. Thus, a *program controlled* update of this value (starting with 0.01) after each iteration is chosen. The friction coefficient is set to 0.01 as usual for cartilage-cartilage contacts [174] and described in Section 3.1.1.

Furthermore, the acetabulum is fixed in all directions, and all parts of the hip joint are inserted with the standard coordinate system of MIMICS®. These conditions are added to the model under *Static Structural*. The surfaces of the ilium, which are showing cranial, are fixed.

The meshing in FEM simulations is essential and, thus, the following parameters were selected:

Table 3.3: Mesh for Femoroacetabular Impingement

Part	Method	Algorithm	Max. Element Size	Feature Angle
Acetabulum	Tetrahedrons	Patch Independent	20 mm	30°
Femur	Tetrahedrons	Patch Independent	5 mm	30°
Labrum	Element Size		1 mm, Soft Behavior	

A *Patch Independent* algorithm is selected due to the high number surfaces. The *Patch Indepenedent* mesh method is used to ensure refinements of the mesh wherever they are necessary, but also maintains larger elements where possible [157]. This method allows a faster computation. Additionally, a virtual topology, consisting of tetrahedrons, is generated over all bodies [153]. During the first tries with the maximum element size is set to 2.5 mm with a feature angle of 22° [171]. However, the simulation duration increases and, thus, the maximum element size and feature angle are increased, as visible in Table 3.3. For the labrum, the *Patch Independent* algorithm is not compatible, because the geometry is very complex, wherefore the method is changed to *Element Size*.

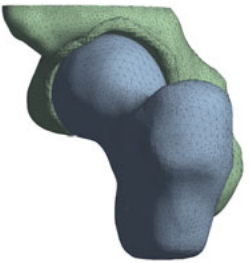

Figure 3.19: Meshing of a Patient-Specific Hip Model

One example for the mesh of a patient-specific hip model is visible in Figure 3.19. The number of elements and nodes are illustrated in Table 3.4. The finer the mesh settings are chosen, the more elements and nodes are generated and the duration of the simulation increases. It is important to find a setting, which combines an acceptable simulation duration with a reasonable accuracy of the geometry.

Table 3.4: Meshing results with and without Labrum

Method	Elements	Nodes
without Labrum	284,186	419,459
with Labrum	585,890	112,629

The mesh quality shows good results with the settings visible in Table 3.4. Only very few elements, which were not in the area of interest, showed a bad quality. The meshing of the small labrum is very difficult. The skewness of the mesh is one option to evaluate the quality. The range is between 0 and 1. The closer the value comes to 1 the worse is the quality. A value below 0.5 indicates a good quality of the mesh [157].

Since a few years, FE simulations are also essential in biomechanics. For FAI resulting deformations and stresses of the bones can be predicted and so it can be compared to patient's limitation of movement and pain during special movements. For the FHN, the FE simulations are important regarding stresses and stability of the bone and to investigate the angle for drilling with the lowest stress. More information for FEM can be found in Gebhardt, Klein and Rust [153, 68, 151].

Material properties of cortical and cancellous bone are illustrated in Table 3.5. Thus, the human bone has different material behavior in different directions, it should be considered to correctly model the bone. Unfortunately, there are no feasible bone models in ANSYS for which reason a isotropic material behavior was set in the beginning. Additionally, material properties of labrum and cartilage are not fully investigated, yet. Moglo et al. [175] and Ferguson et al. [176] found cartilage and labrum properties of a bovine sample as illustrated in Table 3.6. Cartilage material properties have been set to linear elastic.

Table 3.5: Material Properties of the Cortical Bone

Author	Cortical Bone		Cancellous Bone	
	E [MPa]	ν [-]	E [MPa]	ν [-]
Rohlmann et al., 1982 [77]	18.000	0.33	30-2000	-
Zhao et al., 2010 [177]	17.000	0.30	not used	
Anderson et al., 2010 [178]	17.000	0.29	not used	
Chengini et al., 2009 [179]	20.000	-	100	-
Speirs et al., 2007 [180]	17.000	0.30	1.000	0.3
Rudman et al., 2006 [181]	17.000	0.33	100 to 400	0.3
Tran et al., 2016 [182]	12.000	0.4	600	0.29

Table 3.6: Material Properties of Soft Tissues

Soft Tissue	Author	E [MPa]	ν [-]
Cartilage	Moglo et al., 2003 [175]	12.00	0.45
Labrum	Ferguson et al., 2001 [176]	20.00	0.40

The implementation of anisotropic material behavior of bone into finite element analysis would describe the stresses and deformation more exact, because elastic modulus, shear modulus and Poisson's ratio differ in the directions visible in the Table 3.7. Since the exact orientation of the single elements in a bone remains unknown, it is difficult to implement this in the model.

However, a better understanding of the biomechanical procedure of the FAI is important and forces are not applied into these simulations so a linear elastic material model is assumed as it was chosen by Tran et al. [183].

Table 3.7: Elastic Modulus, Shear Modulus and Poisson's Ratio for the Pelvis and Femur with a Linear Elastic Orthotropic Behavior [184, 185]

Elastic Modulus [GPa]	Shear Modulus [GPa]	Poisson's Ratio [-]
$E_x = 11.6$	$G_{xy} = 4.0$	$\upsilon_{xy} = 0.42$
$E_y = 12.2$	$G_{yz} = 5.0$	$\upsilon_{yz} = 0.23$
$E_z = 19.9$	$G_{xz} = 5.4$	$\upsilon_{xz} = 0.23$

The *Contact Tool* was used, which contains, e.g., *Status*, *Penetration,* and *Gap*. This is very useful to analyze the collision of the femur with the acetabulum or labrum.

The simulation is controlled by joints, which are generated to operate the rotations around every axis for flexion, adduction, and internal rotation, respectively. The determined angles of the motion analysis for every patient can be inserted into the particular joint as shown in Figure 3.20.

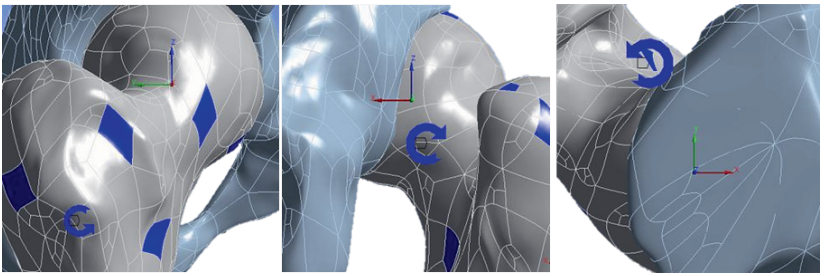

Figure 3.20: Rotation Joints for Every Axis to Control the Simulation

3.2.5 Determination of the Bone Removal

A optimal treatment for FAI patients is the removal of the bony deformity, which disables the free movement of the femur. For this purpose, CAD Tools can be used to determine the removed bone part by using CAD simulation. A free movement of the femur can be

guaranteed after removing the colliding part of the bone. CAD software is more suitable than FEM software for this project due to the fast calculation-time.

The bone removal surgery can be performed using the navigation system of Brainlab (Brainlab AG, Munich, Germany) Hence, it is possible to mark the bony deformity in the simulated model and load this result in the system of Brainlab. The Brainlab-pointer can be used during the surgery and, hence, a controlled removal of the bony deformity can be performed using the navigation-controlled surgical tool.

3.2.6 Post-Operative Simulation of Patient-Individual Hip Joint Models

The post-operative simulations are performed in the same way as pre-operative simulations. Both CAD simulations and FEM simulations can be developed using the MRI data after surgery. At the end a comparison between pre-surgery and post surgery can show the outcome of the surgery and if enough bone is removed to ensure the most possible range of movement for the patient.

3.3 Femur Head Necrosis

A three-dimensional computer aided design model of full femurs is generated from MRI scan data. The standard sequence for necrosis is used described in section 2.2.1.

3.3.1 Generation of the Computational Domain (CT and MRI)

The segmentation of the femur was performed using MIMICS®. DICOM files were processed and the 3 mm slices were manually segmented. Subsequently, the generated rough STL model was smoothed using MeshLab. Errors and irregularities of the model could be repaired with the disadvantage that the geometry is changed and, hence, is not as accurate anymore. This is necessary to guarantee an accurate three-dimensional model. Facets with errors must be eliminated and surfaces have to be smoothed using the same procedures described in section 3.2.2. The segmentation process of MRI data was equal compared with the process in the FAI study. The CT data handling is easier due to threshold-tools of MIMICS which automatically select the needed tissue, e.g., the femur in this study.

Afterwards, the 3D model is generated using FreeCAD.

3.3.2 Determination of the Center of Mass of the Necrotic Area

In this section, the determination of the center of mass of the necrotic area is described. The necrotic area is also segmented manually and converted into the 3D model using the same procedures. This point is the endpoint for the drilling path to enable the most possible removal of the necrotic area. For this purpose, the function *Analysis* → *Mass*

Properties → *Center of Gravity* is used. Finally, both models, the femur and the necrotic area, are combined in Creo Parametric with the *Component Operation* → *Cut Out* in *Assembly Mode*. The right positioning is guaranteed and the result is visible in Figure 3.21. The model is exported into STEP for the simulations. This procedure was performed using different CAD software as comparison.

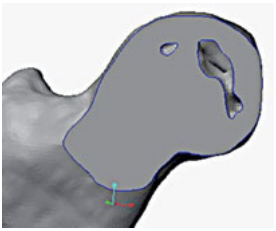

Figure 3.21: Generation of the Hip Model Including Necrotic Area

The drilling holes are generated in ANSYS. For this purpose, one coordinate origin is positioned into the center of the necrosis and at the greater trochanter region.

3.3.3 Finite Element Model

The finite element model is used to determine the optimized drilling regarding occurring stresses. In further studies, two different load cases of the femur are investigated as aggregated in Table 3.8 [183]. These load cases show daily activities and the walking downstairs-case is important due to maximum loads acting on the femoral head according to Bergmann et al. [24].

Table 3.8: Hip Joint Forces [N] During Daily Activities [183]

Load Case	F_x	F_y	F_z	$\|F\|$
Normal Walking	−411.24	−247.1	2078.14	2132.8
Walking Downstairs	−411.29	−227.98	2212.37	2261.8

A coordinate system (t,d) in which t and d correspond to posterior and distal direction is defined. The origin of the coordinate system is located at the inferior border of the greater trochanter in the subtrochanteric lateral cortex as the position of the supposed standard entrance point [183]. Twelve different entrance points were chosen corresponding to twelve models: (0,-5), (0,0), (0,5), (0,10), (0,15), (0,20), (10,-5), (10,0), (10,5), (10,10), (10,15) and (10,20). The coordinates were measured in mm. The nearest entrance points

with respect to the greater trochanter region are (0,-5) and (10,-5). The farthest distal entrance point built (0,20) and (10,20).

A mesh convergence analysis was performed by Tran et al. [183] for the (0,0) case during normal walking for different meshes with different maximum element lengths. A significant difference could not be found and the mesh with a maximum element length of 3 mm was also chosen in this work. The FE analysis for this dissertation are performed using ANSYS v17.

Generally, there is no contact modeling necessary for the FHN project. More important are the correct material properties and a program controlled generation of the drilling core to predict the drilling with the lowest stresses. Therefore, so-called points-of-interest are generated at the trochanter major and the femoral neck, because the failure always occurs in these areas [183]. The program controlled drilling generation is enabled using the parameter function in ANSYS. For this purpose, several parameters have to be defined such as the starting point and ending point of the drilling. Additionally, the center of the necrotic area and the acting force on the femoral head are also specified as a parameter which allows a simple adjustment of the values. The drilling is inserted dependently from the necrotic part as visible in Figure 3.22. Maximum Principle and Shear in the areas of the femoral neck and the entrance point of the drilling channel are calculated. This is implemented in ANSYS using a region of interest.

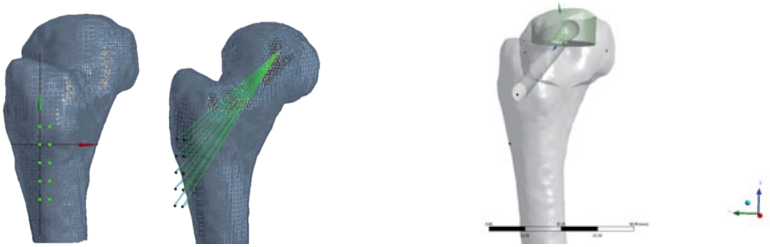

Figure 3.22: Definition of the Drilling

At the center of mass of the necrotic area and at the greater trochanter coordinate origins are inserted to ensure the parameter controlled drilling.

The limitation of this simulation is given because the whole bone is not divided into cancellous and cortical parts, however test simulations showed similar results of the stresses which leads to the hypothesis that a complete cortical bone show a very similar behavior compared with the study of Tran et al. [183]. Although, the MRI quality insufficient for a separate segmentation. The material properties used are the same Tran et al. [182] presented. Additionally, a comparison between a model exclusively using a cortical bone and a model with cancellous and cortical bone is performed in this study.

The necrosis area is inserted as a bonded contact. The same meshing settings as Tran et al.'s [183] are used in this dissertation. The meshing results are presented in Table 3.9. Thus, no significant differences were visible in the study of Tran et al. [183] comparing 4-node tetrahedrons and 10-node tetrahedrons. The second is used in this study to evaluate the nodes inside an element.

Table 3.9: Meshing results of the Necrosis Model

Method	Elements	Nodes
10-Node Tetrahedrons	736,516	1.057,709

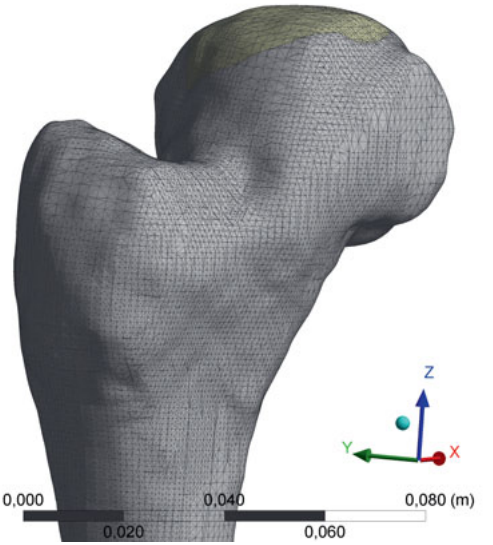

Figure 3.23: Meshing of the Necrosis Model

The skewness for the necrosis models are also mainly in the area between 0 and 0.5, which corresponds to a meshing of proper quality [157]. In Figure 3.23 the fine meshing is visible. The value of the area radius for the femoral neck is chosen $2.0\exp{-002}$ m with an element size of $1.0\exp{-003}$ m. For the entrance point the area radius is $3.0\exp{-002}$ m and element size of $1.0\exp{-003}$ m, which is the reason for the accurate mesh result (cf. Table 3.9).

Another important boundary condition is the fixation of the femur shaft. For this purpose, the bone is cut distal from the hip to ensure a similar fixation for all bones which

are simulated as shown in Figure 3.24.

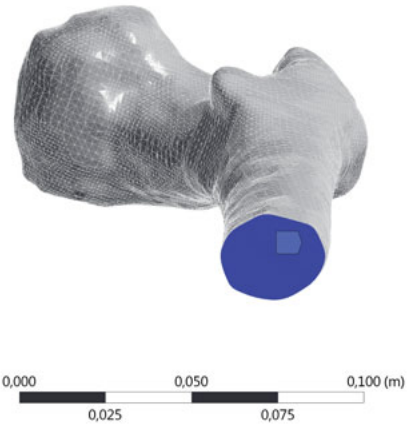

Figure 3.24: Fixation of the Femur

3.3.4 Neural Network

In this section a short introduction of learning machines and neural networks is presented. A neural network is an information processing algorithm, which is created following the way human brains work [186]. McCulloch et al. [187] already developed in 1943 the first formulations of this method, which contains a building of a computational model of the nervous system in the brain [188]. This method allows obtaining patterns and information out of complex data. Neural networks consist of artificial neurons, which are organized into layers, one input layer, one output layer, and one or more hidden layers in-between as visible in Figure 3.25 [189]. The numbers of nodes in the particular layer is given by the nature of the data being processed whereas the numbers of nodes in the hidden layers are adapted to the model which should be developed [189]. Using mathematical terms, relations between the input and output data can be generated to develop a learning machine which can determine the output data for given input data. In this thesis, the used mathematics are not presented, however, it is postulated in [190]. For the training of this system, all calculated data was divided into three sets, 80% training, 10% validation and 10% cross-validation. Subsequently, new data was tested with focus on the question whether the system can predict stresses.

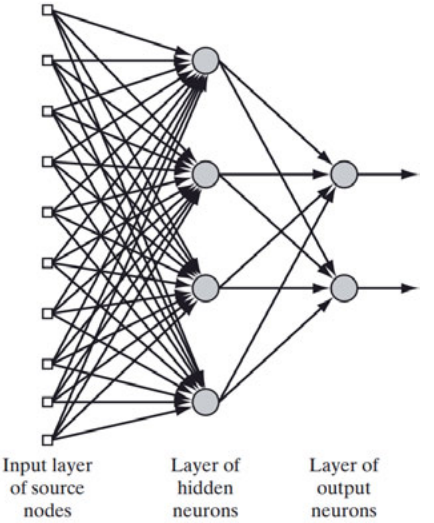

Figure 3.25: Neural Network Schema [189]

In the FHN part, the input data are the geometric data, e.g., the coordinates of the entrance points of drilling, the entrance angles, the coordinates of the center of mass of the necrosis, etc. and the output data are the determined stresses at the femoral neck and the entrance point of the drilling. After calculating the effects of different necrosis patients, it should be possible to predict the occurring stresses without calculating them. Even though a statistic method, e.g., linear regression, which provides known equations, can also be used in this study the neural networks are implemented especially due to their learning ability.

3.3.5 Planning of the optimal Drilling

With the known geometry of the tool for the removal of the necrotic area and the calculated stresses, both results can be combined and the optimal drilling to remove as much as possible of the necrotic area can be planned. For this purpose, a neuronal network is generated with all data of the FEM analysis and additional standard values of the bone were arbitrary chosen, e.g. center of femoral head, greater trochanter, etc.

3.3.5.1 Insertion of the Drill Hole in DICOM

The optimal drilling can be exported as an STL file which can be imported in MIMICS®. Using the tool *Calculate Mask from Object,* MIMICS® calculates a two-dimensional mask

of a STL model. Using the right sectional view, the drilling can be illustrated in a two-dimensional view, which is the goal of this study.

3.3.5.2 Brainlab Interface

The company Brainlab is a medical engineering company which develops navigation systems for surgeries to guarantee a high medical standard and a advanced health care and, hence, an optimal surgical outcome. This company developed a two-dimensional navigation application on trauma which enables a two dimensional navigation without any further preparations as visible in Figure 3.26.

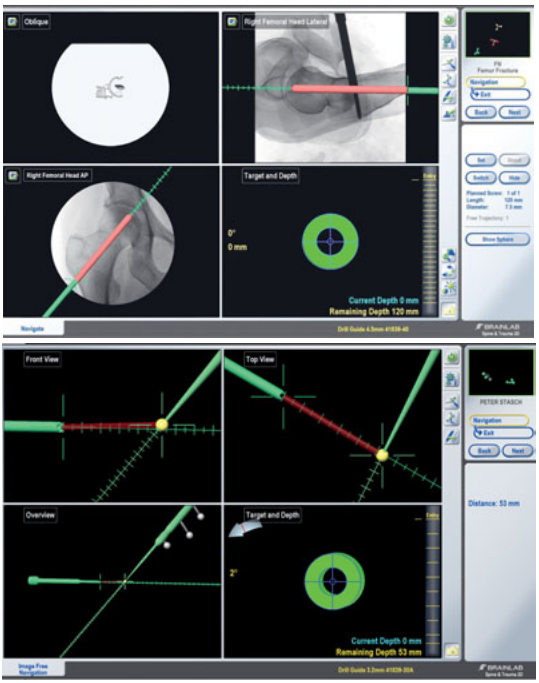

Figure 3.26: 2-Dimensional Trauma Navigation (Brainlab)

Using the therefore special developed surgery equipment, it is possible to navigate to a point which is manually set with the so-called pointer. The angle and the directions are shown on a monitor. On one window the anteroposterior view (up right) and on another the lateral view (down left) are shown. On the down right side the navigation with the target and the depth are displayed and the angle and the distance can be controlled. In combination with the calculated drilling, the optimal surgery can be performed to ensure

the best possible necrotic removal with simultaneous consideration of lowest stresses.

3.3.6 Influence of Bone Substitute

In this section the influence of the bone substitute is investigated using a static compression test and a CT scan before and after the compression test for comparison.

Static compression tests are performed to validate the model using six pairs of femoral cadaver bones provided by the Institute of Anatomy of the University of Duisburg-Essen. The test setup is visible in Figure 3.27. One femur of each pair was treated with the ACD as described by Landgraeber et al. [145]. The femur were bored with a 9 mm drill to the subchondral bone of the cranioventral part of the femoral head. With the X-REAM™ the maximum size of 21 mm were cut out of the bone and the occurred channel was filled with the bone substitute PRO-DENSE®. The contrary femur remained untreated for comparison.

The biomechanical testing was performed as described by Tran et al. [183] on a compression machine equipped with a calibrated 10kN load cell in the stance-like load configuration. The compressive force was applied to the femoral head through a metal cup, which was inclined at 20° to the shaft axis. The distal end of the femur was placed into a metal fixture to prevent sliding during the test, which was also inclined by 15° in order to guarantee physiological conditions (knee joint). Furthermore, both the cup and the fixture were filled with silicone to ensure a smoothly force transmission. The upper metal cup moved with the velocity of 30 mm/min to the fixed lower fixture until the force of 2000 N is reached. As comparison both bones were investigated using the CT, however, there were no significant changes of the interface between substitute and bone.

Figure 3.27: Experimental Setup of Compression Test

4 Results and Discussion

In the following section, the results of both studies are presented. First, the results and discussion of the FAI project are presented, subsequently, the FHN.

4.1 Femoroacetabular Impingement

In this section the results of the FAI are presented. First, the geometric parameters, e.g., HJC, HHD etc. Furthermore, the simulation results and, closing, the planing of the bone removal is presented.

4.1.1 Modeling

The single parts of the hip joint, femur, acetabulum, and the labrum were segmented from the data obtained from the MRI. Afterwards, the generated facet models were processed by the resurfacing procedure and the conversion for further steps using both described software.

The resurfacing procedure is due to the rough surface after the segmentation. This can be related to the rough slice sickness of the MRI data with 1.5 mm. Thereby, subtle bone parts might not be visualized on the images, which can cause an inaccurate model. Additionally, the smoothing procedure can reduce the model quality as well, hence, two different methods, so-called Poisson and NURBS methods, were compared with each other. The results show no significant differences regarding the degree of movement, as visible in Table 4.1, determined by the CAD software. Only the abduction angle varies. However, the NURBS method removed less material of the bone and the geometry became smoother and, hence, more natural. Due to this fact, in following studies, the NURBS method has the advantage that there are fewer surfaces and, hence, a shorter calculation time in the simulations.

Table 4.1: Comparison Between Both Smoothing Methods

Method	Poisson (FreeCAD)	NURBS (CATIA)
Flexion	120°	120°
Extension	71°	72°
Abduction	40°	30°
Adduction	39°	38°
External Rotation	79°	81°
Internal Rotation	40°	42°

Apart from that, the general quality of the images obtained from the MRI scan also affect the model quality. The difficulty is to identify parts which belong to the bone or to the soft-tissue, e.g., cartilage, labrum, etc. For that reason, it is impossible to ensure that the generated hip joint models represent only bony parts or also small areas of soft-tissue. The scan sequence which is used to generate the MRI is important to visualize different tissues, e.g., T2w water-excitation dual echo steady state, which visualize the contrast of cartilage better, however, other parts might pictured worse. A contrast medium might also help.

Table 4.2: Example of Models after Smoothing Using Different Software

Characteristics	Facet Model (STL)		Solid Model (STEP)[1]		Solid Model (STEP)[2]	
	Femur	Acetabulum	Femur	Acetabulum	Femur	Acetabulum
Edges	14,772	24,387	15,000	37,488	951	1,133
Faces	9,848	16,258	10,000	24,992	433	514
Size [MB]	0.48	0.79	24.8	62.5	10.9	11.7

[1]Model Generation Using FreeCAD (Poisson)
[2]Model Generation Using CATIA (NURBS)

In Table 4.2 are the differences between both methods listed. The NURBS generated models have fewer edges and faces and, thus, smaller file sizes. In Figures 4.1 and 4.2 examples of bones smoothed with both methods are presented. On the left is the untreated bone, in the middle the bone edit with the Poisson method and on the right is the bone with the NURBS method visible. The NURBS method in the middle retains most of the bone when compared to the Poisson method. In the neck area more bone material is retained compared to the bone smoothed with the Poisson method as illustrated on the right side. The file size of the Poisson is bigger, because a part consists of many surfaces. The complete surface of the model consists of small triangles, which makes the calculation time longer when compared to bones processed with the NURBS method.

4.1.2 Geometric Parameter

In the following, the results of the determination of the geometric parameters are presented and discussed, starting with the HJC. In general, all geometric parameters can be determined in the 3D model or in the segmentation software (MRI data). Which measurement method is more suitable will be discussed in section. Since only two patients could be investigated before and after the surgery, more patients should be investigated in future to verify the presented results on a larger scale.

Unedited Poisson NURBS

Figure 4.1: Femur Smoothed Using Different Software

Unedited Poisson NURBS

Figure 4.2: Acetabulum Smoothed Using Different Software

4.1.2.1 Hip Joint Center

Several methods are presented in Section 3.2.3.1. After comparing the vector lengths of the motions capture and MRI analysis both should have approximately the same length, however, a difference of an average of 14.1 mm was determined (8.76 to 20.57 mm) as described by Westermaier [171]. These results can be explained due to the errors of the skin as a result of the motion capture system used in this study. The patient is lying in both measurements in the dorsal position, hence, it is not possible to exclude that this position is exactly the same during the MRI scan. Additionally, different markers are used in the MRI due to the fact that the markers of the motion analysis are not visible in the MRI. Furthermore, Sangeux et al. [191] showed in their study that an standard deviation of 15 mm is common using Motion Capture system to determine the HJC. With regard to the typical hip joint diameter of ca. 45 mm, this method shows very inaccurate results and is, thus, not usable in future.

The sphere-fitting method for determination of the HJC creates based on 3000 data sets a construction study in a CAD software for calculating the nearest distance with the best solution. A criterion of maximum distance value is set to 1 mm, which yields to a

reduction of the data sets to around 30. If this criterion is set stricter, the number of possible data sets would decrease, which would influence the determination method too much, e.g., if the points placed on the sphere would not be "perfect" a whole data set would not be considered. The minimal total variance of the remaining data sets is calculated and the result of one example is visible in Table 4.3.

Table 4.3: Results of the Different Methods for the Determination of the HJC

Method	x-Coordinate	y-Coordinate	z-Coordinate
Circle Method	41.25	28.98	−3.60
Sphere-Fitting Method	41.91	29.53	−3.89

Since both methods do not vary significantly, they can be used to determine the HJC. The other method, MIMICS® method, works fine if other measurements of the hip joint are needed, e.g., the femoral head diameter. The simulations performed with both HJC showed a maximum difference of 1.2°, which is very good for the investigation of the FAI. It can be assumed that both methods for determination are not far away from the real rotation center.

The HJC can be checked using the CAD function Motion Envelope as described in Section 3.2.3.1. In Figure 4.3 a cut through the femur is visible. The femur (blue) is compared to the generated envelope using the circle method (yellow) and sphere-fitting method (grey) and some material of the envelope is visible around the femur. The amount of material is in both methods nearly the same and this also leads to the assumption that both methods are feasible to determine the HJC.

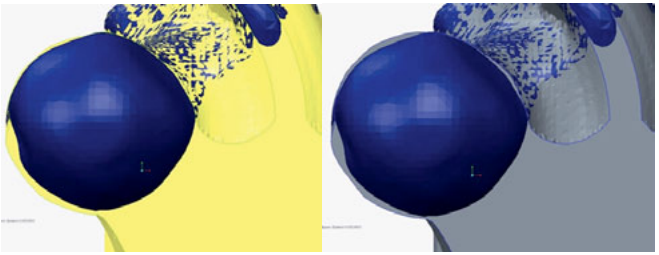

Figure 4.3: Motion Envelope to check the HJC using CAD software [171]

Concluded, all presented methods generate a HJC, which is approximately the real rotation center of the hip joint. However, the circle method has the advantage that it can be performed in a simple manner and with every CAD software. If a comparison between pre and post surgery is needed, the MIMICS® method is reasonable due to the fact that

other parameters must be determined anyway. In the next section the Hip Head Diameter results are presented.

4.1.2.2 Hip Head Diameter

In this section the results of the determination of the Hip Head Diameter are presented according to the method described in Section 3.2.3.2. The Hip Head Diameter (HHD) measurement is performed in different positions and in each position different values were determined as listed in Tables 4.4 and 4.5 for two patients.

Table 4.4: Femoral Head Diameters Measured from MRI Data and the 3D Model of Patient 1

Position	MRI Data		3D Model	
	PRE	POST	PRE	POST
1-7 o'clock	40.8	40.7	41.9	40.9
2-8 o'clock	40.7	40.4	40.3	40.2
3-9 o'clock	41.1	40.8	41.7	40.9
4-10 o'clock	40.8	40.2	40.0	40.5
5-11 o'clock	40.8	40.9	41.4	40.5
6-12 o'clock	41.1	41.1	42.0	41.0
Mean Diameter	40.9 ± 0.2	40.7 ± 0.3	41.2 ± 0.8	40.7 ± 0.3
	40.8		40.9	

Table 4.5: Femoral Head Diameters Measured from MRI Data and the 3D Model of Patient 2

Position	MRI Data		3D Model	
	PRE	POST	PRE	POST
1-7 o'clock	51.3	51.6	52.0	51.5
2-8 o'clock	52.8	51.4	52.0	51.5
3-9 o'clock	51.6	51.1	51.1	50.8
4-10 o'clock	50.5	50.5	51.4	49.8
5-11 o'clock	51.6	50.3	51.8	50.6
6-12 o'clock	52.2	51.3	52.0	51.3
Mean Diameter	51.7 ± 0.7	51.0 ± 0.5	51.7 ± 0.3	50.9 ± 0.6
	51.4		51.3	

Since this example shows a female patient's data and the average femoral head lies around 42.2 mm according to Milner et al. [192], both measurement methods show adequate results comparing the mean diameter, which differ in 0.24. The second patient's mean diameter of the femoral head is larger, because the patient is male. The average femoral head diameter of male lies around 48.4 mm [192]. A small difference can be seen comparing both methods.

Both patients show a reasonable difference between both measuring methods, however still all comparing measurements were performed subjectively which means that the diameters are not the true values.

4.1.2.3 Femoral Neck Axis

The femoral neck axis (FNA) could be determined by using the method which is presented in Section 3.2.3.3. The quality of the determined FNA can only be estimated by the length difference of both perpendicular lines to the surface of the femur. The maximum difference is around 4.1% and, thus, it is exact enough regarding any investigations in biomechanical areas.

4.1.2.4 Offset

The offset can also show if a hip joint is affected with an impingement. It describes the distance where the femoral head loses its sphericity and the highest point of the femoral head. Additionally, the offset ratio is calculated using the mean diameters measured through both, MRI and 3D model. However, for Patient 1 the results of both, MRI and 3D model, show that the required 10 mm according to the literature were not reached by the surgeon and, hence, the surgery could be performed better, visible in Table 4.6 [28]. After the surgery, there is not a significant change between pre data and post data (MRI) recognizable, except the 3 o'clock and 4 o'clock position. The results of the 3D model show similar changes as visible at the 3 o'clock and 4 o'clock position. Nonetheless, the values are still below the mentioned 10 mm. The offset ratio is also determined as visible in Table 4.7 for each position, however, the data lacks a significant symptomatic FAI in contrast to Tannast et al. [28] findings. The value of the offset ratio should be between 0.21 ± 0.03 for a healthy patient and 0.13 ± 0.05 for a patient with symptomatic FAI. Summarized, the offset and partial offset ratio values of the Patient 1 show no significant FAI outcome, which can be related to the poor subjective measurement and segmentation process.

Table 4.6: Offset Values [mm] Measured from MRI and 3D Model of Patient 1

Position	MRI			3D Model		
	PRE	POST	DIF	PRE	POST	DIF
1 o'clock	−1.2	0.6	1.8	−0.4	−0.6	−0.3
2 o'clock	0.4	0.8	0.5	−0.8	−0.1	0.7
3 o'clock	1.2	3.8	2.6	0.5	5.8	5.3
4 o'clock	4.2	5.6	1.4	4.4	8.3	3.9
5 o'clock	7.2	6.4	−0.8	7.4	7.9	0.5
6 o'clock	6.3	6.0	−0.3	5.6	6.1	0.5
7 o'clock	7.2	7.2	0.1	6.7	6.2	−0.5
8 o'clock	7.6	6.9	−0.6	8.0	6.8	−1.2
9 o'clock	7.1	6.5	−0.6	7.4	5.3	−2.1
10 o'clock	6.2	6.6	0.4	6.7	5.6	−1.1
11 o'clock	7.5	7.1	−0.4	7.6	6.5	−1.1
12 o'clock	0.7	0.2	−0.4	0.0	0.0	0.0

Table 4.7: Offset Ratio Values Measured from MRI and 3D Model of Patient 1

Position	MRI			3D Model		
	PRE	POST	DIF	PRE	POST	DIF
1 o'clock	−0.03	0.02	0.05	−0.01	−0.02	−0.01
2 o'clock	0.01	0.02	0.01	−0.02	0.00	0.02
3 o'clock	0.03	0.09	0.06	0.01	0.14	0.13
4 o'clock	0.10	0.14	0.04	0.11	0.20	0.09
5 o'clock	0.18	0.16	−0.02	0.18	0.19	0.01
6 o'clock	0.15	0.15	0	0.14	0.15	0.01
7 o'clock	0.18	0.18	0	0.16	0.15	−0.01
8 o'clock	0.19	0.17	−0.02	0.19	0.17	−0.02
9 o'clock	0.17	0.16	−0.01	0.18	0.13	−0.05
10 o'clock	0.15	0.16	0.01	0.16	0.14	−0.02
11 o'clock	0.18	0.18	0	0.19	0.16	−0.03
12 o'clock	0.02	0.01	−0.01	0.00	0.00	0

Table 4.8: Offset Values [mm] Measured from MRI and 3D Model of Patient 2

Position	MRI			3D Model		
	PRE	POST	DIF	PRE	POST	DIF
1 o'clock	6.8	7.9	1.1	4.5	6.3	1.8
2 o'clock	4.0	7.7	3.7	2.1	6.5	4.4
3 o'clock	3.4	7.0	3.6	5.0	6.6	1.6
4 o'clock	3.6	6.7	3.1	6.3	7.9	1.6
5 o'clock	8.1	7.6	−0.5	7.9	7.2	−0.7
6 o'clock	7.4	8.2	0.8	6.9	6.6	−0.3
7 o'clock	7.3	7.9	0.6	6.8	7.1	0.3
8 o'clock	9.9	8.7	−1.2	9.2	9.4	0.2
9 o'clock	10.4	8.4	−2	9.1	8.4	−0.6
10 o'clock	8.3	9.1	0.8	7.7	8.2	0.5
11 o'clock	8.9	8.4	−0.5	7.0	10.5	3.5
12 o'clock	8.9	8.2	−0.7	7.9	9.4	1.5

Table 4.9: Offset Ratio Measured from MRI and 3D Model of Patient 2

Position	MRI			3D Model		
	PRE	POST	DIF	PRE	POST	DIF
1 o'clock	0.13	0.15	0.02	0.09	0.12	0.03
2 o'clock	0.08	0.15	0.07	0.04	0.13	0.09
3 o'clock	0.07	0.14	0.07	0.10	0.13	0.03
4 o'clock	0.07	0.13	0.06	0.12	0.15	0.03
5 o'clock	0.16	0.15	−0.01	0.15	0.14	−0.01
6 o'clock	0.14	0.16	0.02	0.13	0.13	0.0
7 o'clock	0.14	0.15	0.01	0.13	0.14	0.01
8 o'clock	0.19	0.17	−0.02	0.18	0.18	0.00
9 o'clock	0.20	0.16	−0.04	0.18	0.16	−0.02
10 o'clock	0.16	0.18	0.02	0.15	0.16	0.01
11 o'clock	0.17	0.16	−0.01	0.14	0.20	0.06
12 o'clock	0.17	0.16	−0.01	0.15	0.18	0.03

In contrast, the other patient, Patient 2, shows different results when compared to

Patient 1, such that the minimum offset according to the literature is reached. The offset and the offset ratio increase after the surgical execution along the affected positions of the femoral head as visible in both Tables 4.8 and 4.9. However, the values are almost all below the desired 10 mm, and the ratios are between 0.18 and 0.24. Unfortunately, this tool is inappropriate to assess the surgical outcome, although, at some positions for the example patient, the values show an improvement.

According to literature values for the offset and offset ratio, the patients, which were investigated, underwent an unsuccessful surgery, however, they were without any pain [28]. Therefore, the alpha-angle has to be taken into account to evaluate the surgical outcome more realistically.

4.1.2.5 Alpha Angle

The most common geometric parameter used for quantifying a cam-type impingement is the alpha-angle and it is determined using the method described in Section 3.2.3.4. This method can be also used either at the CAD model or the MRI data. In Figure 4.4 the method is shown at the CAD model.

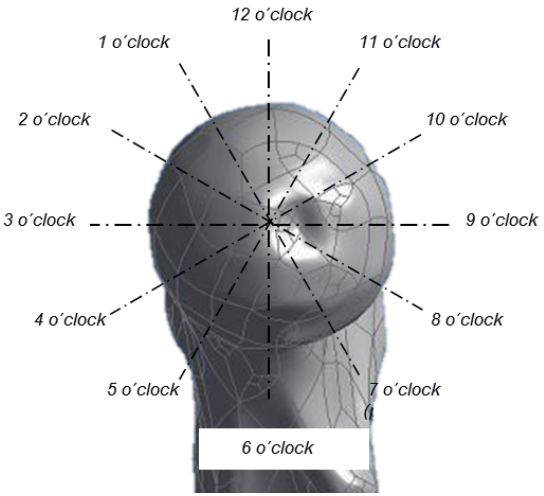

Figure 4.4: Determination of the Alpha Angle using the CAD Model of a right Leg

In Table 4.10 the measured alpha angles of Patient 1 from the MRI data and 3D model, respectively. This value can be measured using both, MRI and 3D model. However, since a patient with an average alpha angle of $42° \pm 2.2°$ is considered healthy, the patient in the example of Table 4.10 does even fails these values after the surgery at the head-

neck junction, because they still exceed the maximum alpha angle value for a significant cam-type FAI of 60° in the position from 12 to 2 o'clock [40, 193].

Table 4.10: Alpha Angles Measured from the MRI and 3D Model of Patient 1

Position	MRI			3D Model		
	PRE	POST	DIF	PRE	POST	DIF
1 o'clock	77.3	76.0	−1.3	86.6	83.5	−3.06
2 o'clock	76.3	73.1	−3.2	85.8	82.4	−3.42
3 o'clock	66.5	51.4	−15.1	71.7	44.3	−27.38
4 o'clock	49.7	45.4	−4.3	49.9	34.9	−15.01
5 o'clock	38.9	40.6	1.7	38.9	36.6	−2.29
6 o'clock	43.4	42.8	−0.6	43.5	43.9	0.43
7 o'clock	37.6	37.2	−0.4	40.2	43.8	3.59
8 o'clock	37.8	38.5	0.7	34.9	39.6	4.72
9 o'clock	36.1	41.4	5.3	35.7	43.6	7.92
10 o'clock	41.1	40.4	−0.8	41.0	42.7	1.67
11 o'clock	37.6	39.5	1.9	36.8	41.8	5.04
12 o'clock	78.4	78.1	−0.3	80.5	84.3	3.84

In Figure 4.5 two MRI images illustrate the 2-8 o'clock position before (left) and after (right) surgery. The measurement was performed by the attending physician (yellow arrow). The red line show the contour of the bump which may cause the impingement, which should be removed (green arrow). After the surgery, the bump is significantly smaller but the red arrow still shows an edge which should be removed under optimal conditions. This edge might have a negative impact for the patient, even though, the patient was painless after the surgical intervention. The surgeon would read the angle at the yellow arrows which would lead to a smaller alpha angle. The remaining bump would be neglected, the interpretation changes and so a different surgical outcome is the resulting conclusion. In fact, every measurement generates a very subjective result and is very dependent from the experience of the performing person.

The following Table 4.11 contains the alpha angle measured for Patient 2 from the MRI data and 3D model. In this example the values vary in both methods. This can be a consequence of either a poor segmentation process and, thus, a subjective determination of the parameters or an inaccurate center of femur and, hence, of the femoral neck axis, which also has a significant influence on the measurements. The MRI data show a maximum angle at the 4 o'clock position which is not reliable according to Rakhra et al. [194], because

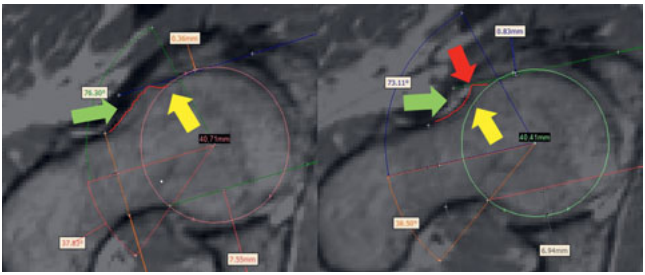

Figure 4.5: Patient 1's Alpha Angle Measurements

the highest value is more likely to be measured in the anterosuperior quadrant. However, both measurement methods do not show the significant angle limit for an abnormality of 50° according to literature [195]. This leads to the conclusion that the surgical outcome can be evaluated as successful for Patient 2, although, Neumann et al. [196] suggest an alpha angle value of only 43° after the surgical intervention at the affected positions.

Table 4.11: Alpha Angles Measured from the MRI and 3D Model of Patient 2

Position	MRI			3D Model		
	PRE	POST	DIF	PRE	POST	DIF
1 o'clock	48.2	42, 8	−5.4	53.8	48.9	−4.85
2 o'clock	57.8	46.5	−11.3	62.5	48.5	−14
3 o'clock	59.6	45.5	−14.0	50.8	47.4	−3.47
4 o'clock	60.5	47.9	−12.6	44.5	42.9	−1.56
5 o'clock	43.2	43.2	0.0	41.8	44.6	2.78
6 o'clock	43.1	40.4	−2.8	45.5	46.6	1.11
7 o'clock	43.4	42.9	−0.6	45.6	43.9	−1.73
8 o'clock	37.9	36.9	−1.0	40.3	38.4	−1.92
9 o'clock	35.8	39.4	3.6	40.2	40.0	−0.14
10 o'clock	37.8	39.1	1.3	42.1	42.1	−0.07
11 o'clock	40.8	43.0	2.1	40.9	36.9	−4.08
12 o'clock	43.0	42.7	−0.2	42.7	40.2	−2.53

In conclusion, the measurement of the alpha angle is a very subjective procedure to investigate the FAI and both methods show differences between the values. Hence, only one method should be used in future and the measurement in the MRI data is more accurate because the bones are not smoothened. For a quick view of the angle's magnitude, the

MRI data is enough, however, the 3D model provides more helpful tools and features, e.g., conditions for parallel lines, which enables a more accurate measurement of the offset. Nonetheless, the most important criterion for a successful determination of all parameters are high qualitative MRI data, which are necessary for good 3D models.

Comparing both methods, offset/offset ratio and alpha angle to quantify the FAI, the alpha angle may be more accurate to assess the severity of the FAI. The results of the offset show symptoms for a cam-type impingement even after the surgical intervention, while the alpha angle indicates no such evidence.

4.1.3 Simulation

In this subsection the results of the simulations before the surgery are presented and discussed. The simulations of several patients could be examined before the surgery. Unfortunately, only two patients were available after the surgery. In the future, more patients should be examined with respect to their surgical outcome.

The outcome of the surgery only can be compared by investigating the range of motion before and after the surgery. CAD software and FEM software are used to compare the results with each other. The advantage of the FEM software is that occurring stresses can be investigated besides the contact.

4.1.3.1 Geometric Software (CAD)

The range of motion is examined pre-surgery using Creo Parametric. For every movement, the contact of femur and acetabulum are determined and, thus, the angle of contact is determined. The calculation time for this simulation takes around 25 min. Generally, the CAD simulation, visible in Figure 4.6, is suitable to predict an impingement. For example, the flexion movement of 120° of one patient showed an impingement at the anterior position with the acetabulum, which is usually not considered to be a typical cam-type impingement. The red area marks the impingement. For the extension movement, a collision can be detected at 71° in a posterior position, which is unsuitable for a cam-type impingement. For every movement, the maximum possible angle can be determined using CAD software with low effort compared to a FEM software.

The angle, which is reached by the abduction movement is around 40°. This area of collision is important for FAI. A collision is also detectable for the adduction movement at 39°, which is irrelevant for FAI. This contact is also between complete irrelevant parts of the hip joint (femoral shaft and ischii). At least, the internal and external rotations are investigated. The internal rotation shows a contact at 40°, which can be relevant for the FAI, the external rotation shows no relevant contact.

In Table 4.12 all angles are listed and whether they are relevant for FAI.

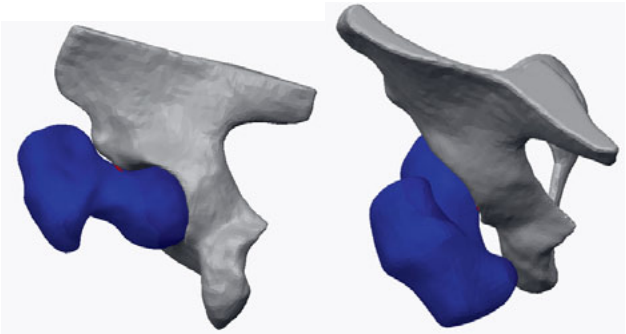

Figure 4.6: Example of CAD Simulation of Flexion Movement (right) and Abduction Movement (right)

Table 4.12: Contact Angle Determined Using CAD Simulation

Movement	Angles	FAI relevant
Flexion	120°	no
Extension	71°	no
Abduction	40°	yes
Adduction	39°	no
Internal Rotation	40°	yes
External Rotation	79°	no

4.1.3.2 Finite Element Method - Software

The results, produced with the CAD software, are similar to these with the FEM software. Simulations without the labrum were separated into four load steps with program controlled substeps and the meshing divided the two bone parts into 15.162 nodes and 74.314 elements. The FAI simulation (90° flexion with 65° internal rotation) takes 23 hours and 195 iterations to converge. The contact and angle are the identical compared to the CAD software, respectively. Using the contact tool of the FEM software, which is visible in Figure 4.7, the contact status can be determined for each angle and as visible, if a contact occurs (left), how large the penetration is (middle) and, additionally, the size of the gap (right) in case there is no contact.

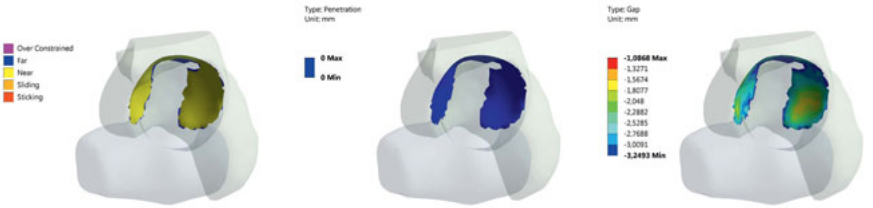

Figure 4.7: Example of Simulation Using the Contact Tool of the FEM Software

A bony contact could not be detected. However, the gap between the bones become very small which leads to the hypothesis that soft tissue might be squeezed between bones. This might be the origin to generate pain for the patient for which reason the labrum was implemented into the simulation as illustrated on the right in Figure 4.8.

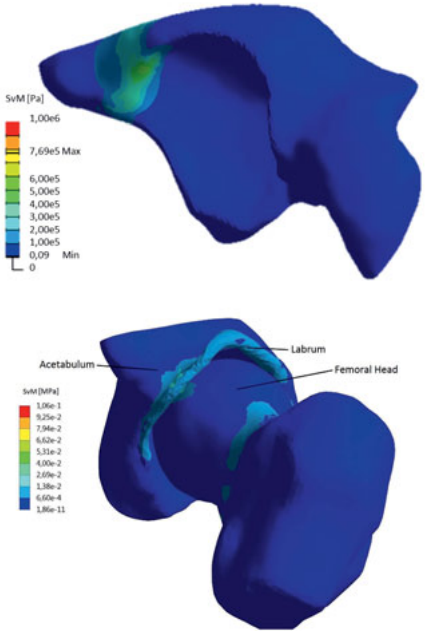

Figure 4.8: Example of Simulation Result with Stresses von-Mieses [Pa]

The contact is analyzed using the first principle stress, status modeling and gap modeling. Including the labrum, the simulation results show a contact between femoral neck and labrum at angles, which correspond to the pain area of the gait lab. Additionally, the status modeling show a sliding contact and the gap decreases to zero.

Figure 4.9 shows the results of the impingement test, which can be simulate until 33° of flexion and 11.5° of internal rotation. At this point, the femur and the labrum collide with each other.

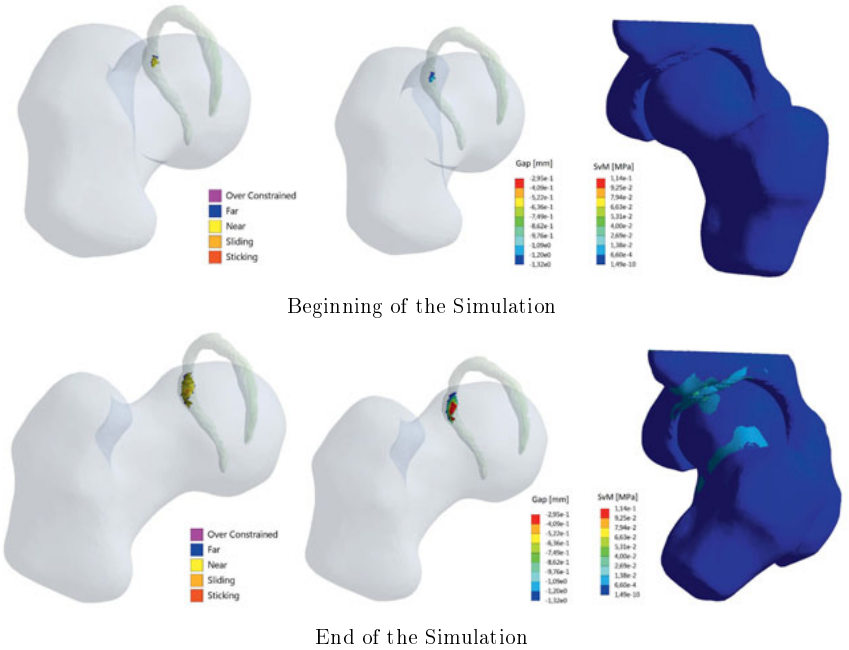

Figure 4.9: Results of Status and Gap Simulation and Occurring Stresses Including the Labrum

On the visible report in Figure 4.10 the results of the impingement test for each the left and right hip are illustrated. A complete report of each motion of this patient is visible in the Appendix 6.1. The red area is the area for the left hip joint, in which the patient pressed the pain sensor. The right leg can be moved by the attending physician without any signaled pain. During the investigation of the physician in the gaitlab, the movement could be performed further, compared to the simulation, which interrupts because a convergence problems occurs. Most likely, a large deformation of the elements, which are in contact with each other, is the reason for this.

Consequently, stresses and the gap between both components, the femur and the acetabulum, are investigated.

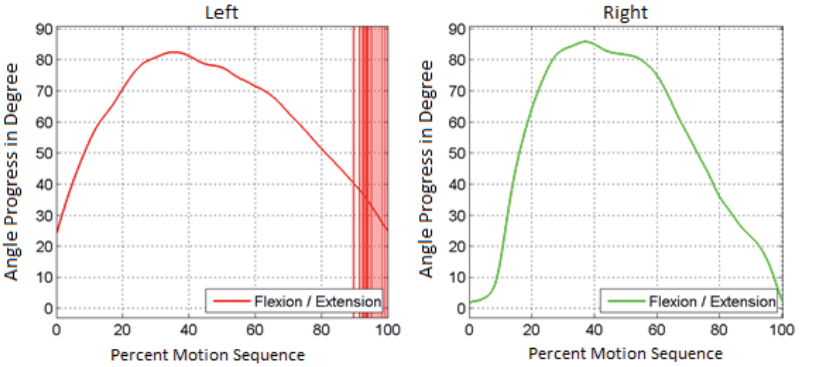

Figure 4.10: Determined Angle of the Motion Capture System [108]

Additionally. the advantage of FEM analysis is that stresses can be determined as visible in Figure 4.8.

The evaluation of stresses and deformations are not advisable due to the fact that only the movement and not forces are implemented into these simulations. In the future, the model can be added by muscle forces, which would improve the whole simulation. In general, a model including the labrum can be generated, however, smaller slice thickness of MRI data is appreciated, which would generate more smooth models and, thus, more natural models of the human hip joint.

The comparison between pre and post surgery was performed without the labrum, because the MRI data quality was not as good to segmentate the labrum as well. Table 4.13 shows the determined maximum average angle of the motion analysis for both patients, which were used for the simulation.

Table 4.13: Maximum Average Angle for Each Movement during the Impingement Test when Pain was Noticed

Movement	Patient 1	Patient 2
Flexion (x-axis)	89.3°	87.9°
Adduction (y-axis)	11.0°	11.7°
Internal Rotation (z-axis)	0.0°	22.3°

The following Tables 4.14 and 4.15 show the model quality. As seen, the computational

time varies due to the number of elements.

Table 4.14: Model Quality of Patient 1

Aspects	Patient 1_{PRE}			Patient 1_{POST}		
	Femur	Acetabulum	$\sum$	Femur	Acetabulum	$\sum$
Nodes	32,198	56,191	88,389	31,346	60,637	91,983
Elements	172,315	281,068	453,383	167,647	302,178	469,825
Mesh Quality Skewness		0.19			0.19	
Computational Time [h]		13.5			19	

The model was imported into ANSYS to simulate the movement with the motion analysis data. The simulation was configured using the settings listed in Section 3.2.4.

Table 4.15: Model Quality of Patient 2

Aspects	Patient 2_{PRE}			Patient 2_{POST}		
	Femur	Acetabulum	$\sum$	Femur	Acetabulum	$\sum$
Nodes	34,372	48,677	83,049	45,875	62,356	108,231
Elements	182,847	243,456	426,303	251,686	318,614	570,300
Mesh Quality Skewness		0.20			0.15	
Computational Time [h]		9			19	

The simulations of Patient 1 show no contact between both bony elements. The motion analysis data show no pain, which confirms the results of no contact. In Figure 4.11 the results are shown in different planes. The left column shows the simulation before, the right column after the surgical intervention. The first row is the isometric view, the second row the axial view and the last row shows the frontal view. Most notably, the fact remains that there is no contact between the bony parts of this hip joint. Generally, a lack of approximation visible except in the frontal view, where the yellow area is larger than before the surgery. This might be related to a poor segmentation of the bony parts or bad MRI data quality. Another possibility is that a vague femoral head center is the reason for the small narrowing.

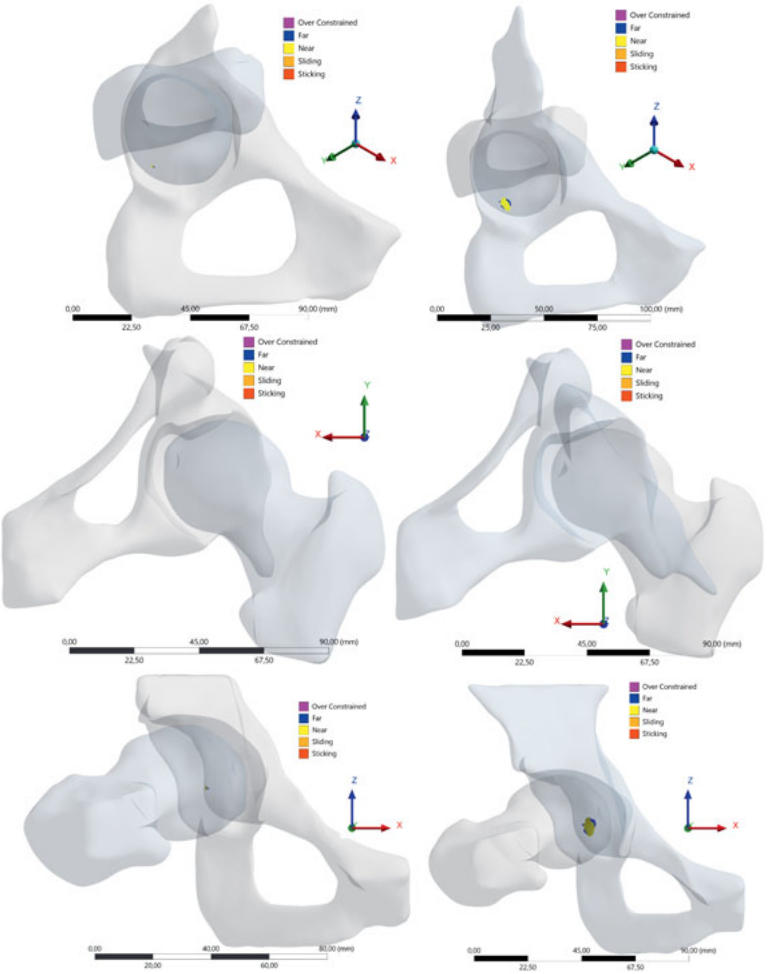

Figure 4.11: Status Modeling of Patient 1 before and after Surgery

Thus, the internal rotation value for Patient 1 is 0°, which might be a sign of a bad performance of the physician's investigation in the gait lab or an error of the motion capture system. Due to the fact that good simulation results require a correct performance of the motion analysis is needed. The lack of an internal rotation might also be the reason why the patient felt no pain during the examination. Hence, another simulation was set up using the same values for the flexion and adduction, supplemented with an internal rotation of 19.3°, which was determined by calculating the average of the maximal achievable angle

of the single movement.

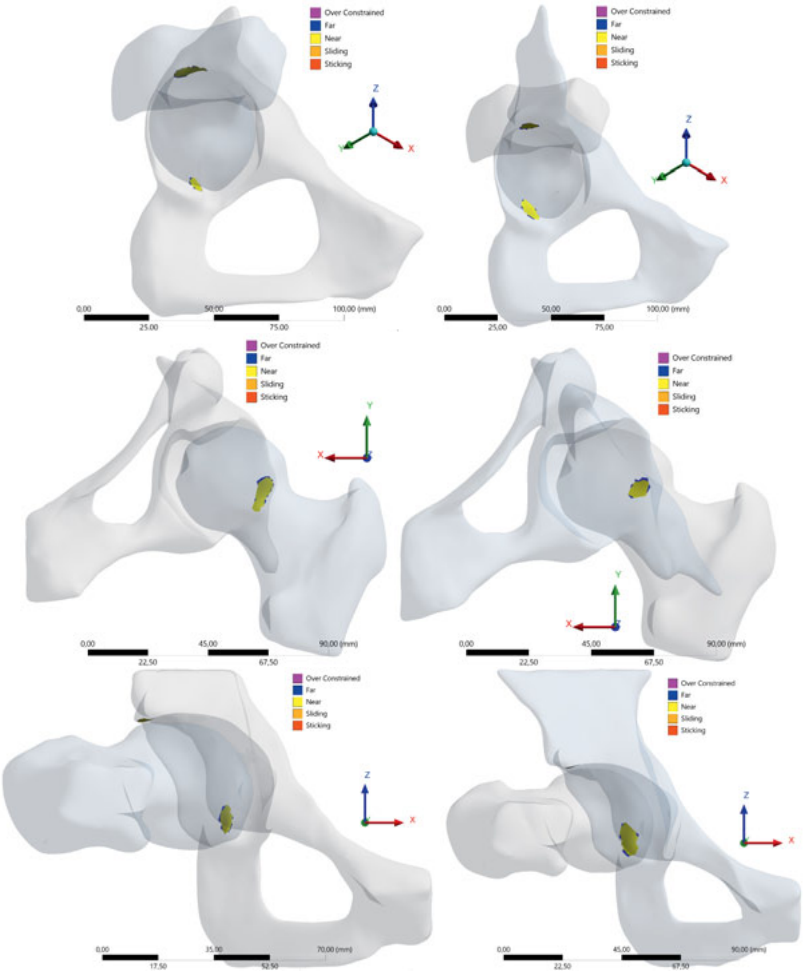

Figure 4.12: Status Modeling of Patient 1 Including the Internal Rotation of 19.3°

The new results show a closer approximation of the two bones, however, a contact is still missing. In Figure 4.12 the narrowing is visible, however, there is no significant change visible after the surgery, except on the axial view. The impingement area became smaller there, nevertheless, it should vanish completely.

Hence, this patient exhibits an abnormal bony structure medial at the femur as visible in Figure 4.13. This atypical shape of the femoral head, indicated by the red arrow, can

be congenital and, thus, normal or it might be the result of a degeneration and, hence, can cause a different moving behavior of the hip joint.

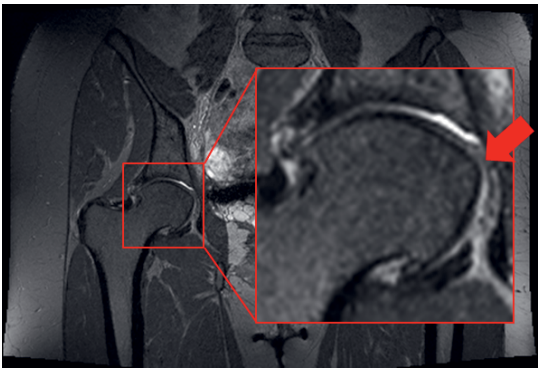

Figure 4.13: Bony Deformity of Femoral Head

The evaluation of the surgical outcome can be only performed based on the simulation including the internal rotation, because there an approximation of both bony parts is visible and it can be assumed, that the soft tissue between these bones could be squeezed and would produce pain. After the surgery, the area decreases. Furthermore, the smaller impingement area supports the results of the alpha angle, which decreased only at the 3 o'clock and 4 o'clock positions.

Additionally, the gap analysis was plotted to determine the distance between both bones and to check whether it decreased or not. Before implementing the internal rotation, the pre-surgery gap was 1.1639 mm, the post-surgery 1.4103 mm and they were located in the medial posteroinferior position of the acetabulum. Visually the area in the frontal view increases after treatment, however, the gap became larger which corresponds to a successful surgical outcome. Unfortunately, the segmentation process can be evaluated as inaccurate due to the fact that the surgery was not performed on the medial femoral head according to the attending surgeon. Including the internal rotation of 19.3° the gap shows no difference in the results compared to no internal rotation, as visible in Figures 4.14 and 4.15.

Lequesne et al. noted that the gap on the superolateral side between femur and acetabulum in straight position is on average 4.69 ± 0.95 mm for women and 5.00 ± 1.15 mm for men [197]. Patient 1 showed distances between both bones of 3.8 mm before and 3.3 mm after the surgery, which can only be a result of a poor segmentation process and bad MRI data quality, because another bony deformation cannot appear in such short time. This also affects the reliability of the simulation results. If the results are correct a narrowing

from 3.8 mm and 3.3 mm to 0.99659 mm and 1.1478 mm, respectively, at the abnormal femoral head shape and a movement to the terminal position of the impingement test including the internal rotation, the patient would feel pain and any damage could not be excluded.

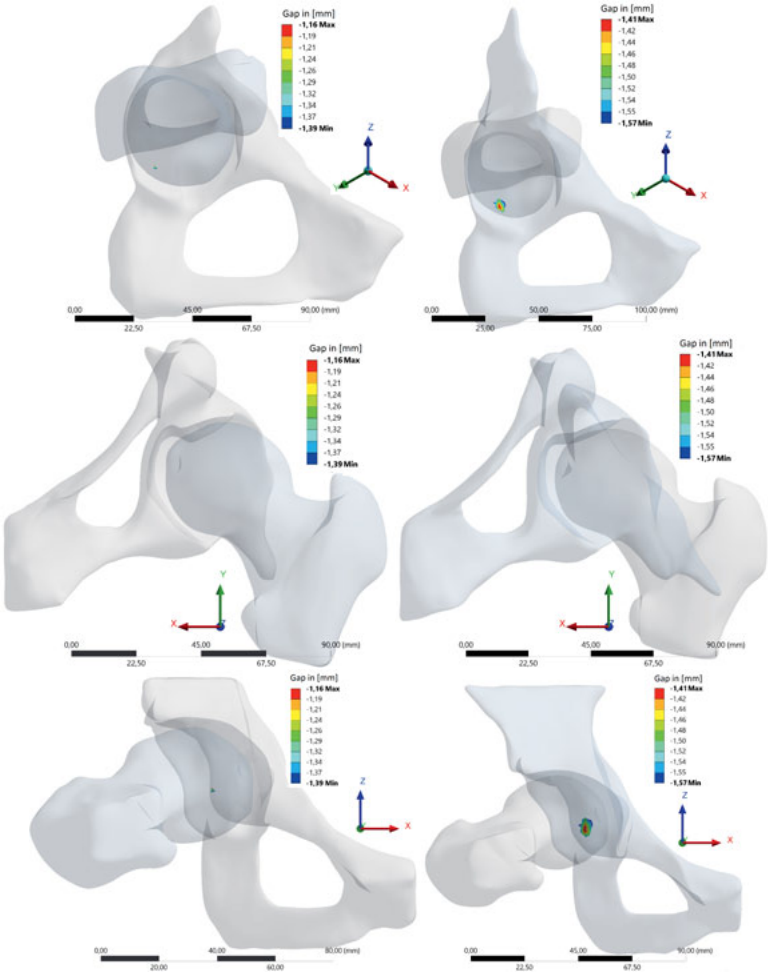

Figure 4.14: Gap Modeling of Patient 1 before and after the Surgery

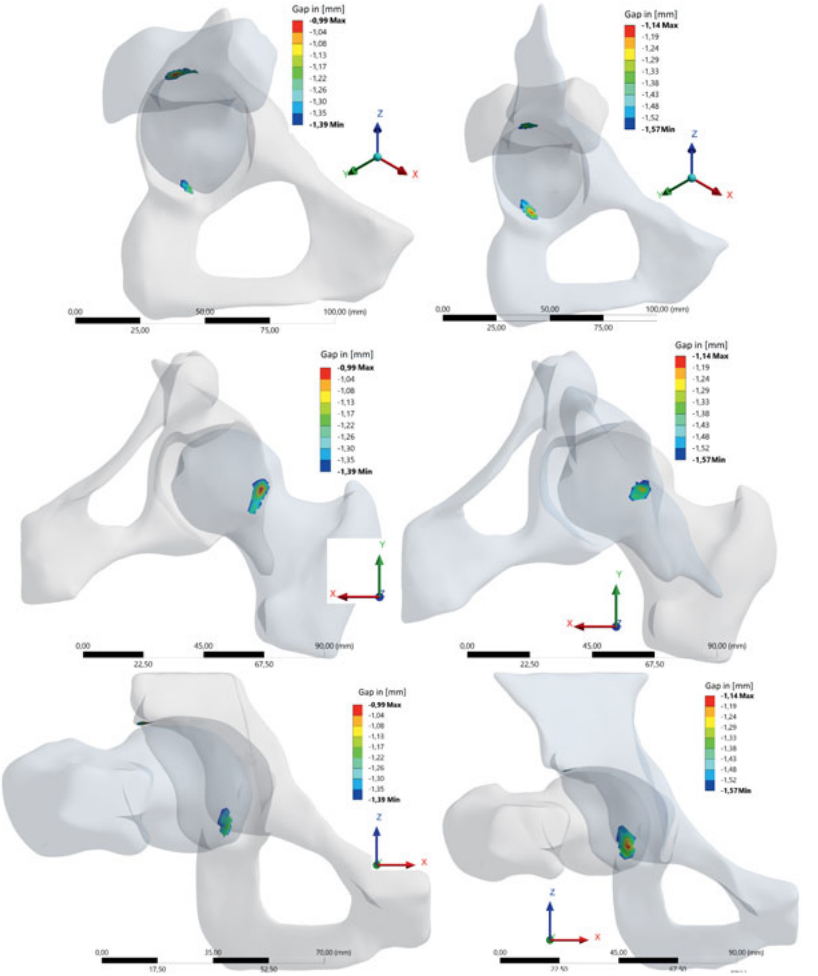

Figure 4.15: Gap Modeling of Patient 1 Including Internal Rotation before and after the Surgery

The simulations of Patient 2 were performed similar to Patient 1 and the results are visible in Figure 4.16. The same views are recorded, first the isometric, then the axial and finally the frontal view. It is visible that in the frontal view of the xz-plane, the only narrowing area appears between the femur and acetabulum is unrelated to the impingement. However, after the surgery, this narrowing has vanished. The axial view shows no impingement of the bones at the marked impingement areas, although, the patient

describes pain during the examination in the gait lab. Again, this can be related to the segmentation process or an inaccurate center of femur. The results of the gap modeling are visible in Figure 4.17. The determined smallest gap before the surgical treatment is 1.3317 mm, however, after the surgery, the gap detection was infeasible because the distance was too large. This can also be related to the segmentation process since the surgery was not performed in that area.

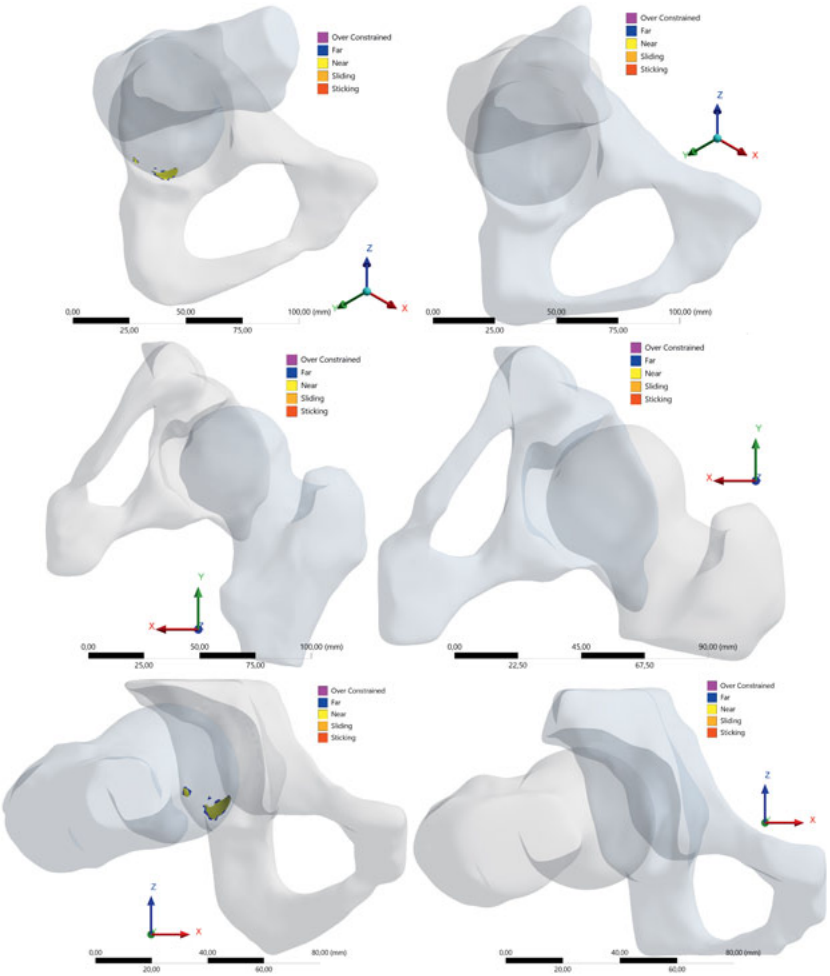

Figure 4.16: Status Modeling of Patient 2 before and after the Surgery

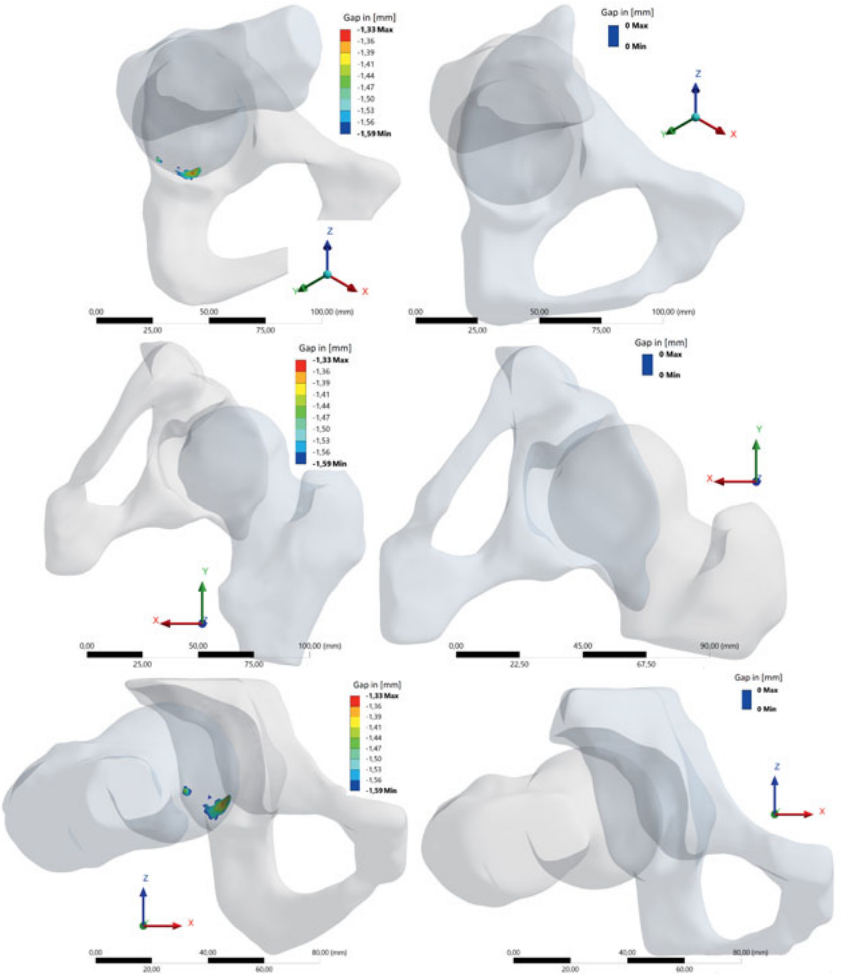

Figure 4.17: Gap Modeling of Patient 2 before and after the Surgery

Additionally, another reason can affect the results, because the very important neutral zero position during the MRI scan was not ensured and due to gravity and comfort for the patient the leg rotates externally, which indicates an incorrect starting position for the simulation [198]. Hence, the internal rotation results of the simulation might be wrong. Sutter et al. [199] reported that every human's femur has an anteversion as visible in Figure 4.18, which means the femoral bone is externally rotated while being in neutral zero position with an average of 16.4° for women and 9.75° for men, respectively. Creo

Parametrics is used to determine the entire external rotation for Patient 2 before and after the surgery, which are 22.5° and 18.7°. Subsequently, the difference between the calculated value and the average external rotation of 9.75° was added to the internal rotation of 22.3° .

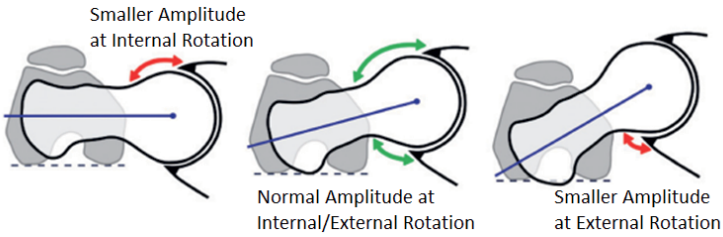

Figure 4.18: Anteversion of the Femur [199]

In Figure 4.19 the new artificial neutral zero position for both before on the left and after surgery on the right are presented. This is only an approximation to the natural neutral zero position. Consecutively, the new internal rotation of 35.05° and 31.25° have to be implemented into the simulations, however, there is still no impingement approximation of the femur and acetabulum recognizable. In Figures 4.20 and 4.21 the results of the adjusted simulations are visible. Exclusively, the status modeling and the smallest gap slightly changed in the frontal view from 1.3317 mm to 1.3142 mm. After surgery no narrowing occurs. The femoral neck axis and the x-axis were used to determine the external rotation degree. An inaccuracy of the femoral neck axis determination can also have an impact on the results and, hence, the approximation of the femur to the acetabulum is still too small. Furthermore, inaccuracies of the gait lab of about ±3° occur on the basis of technical conditions [171].

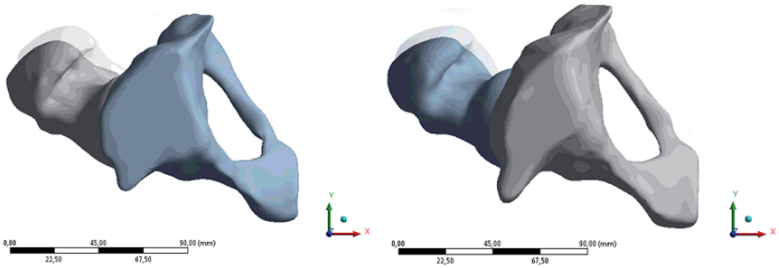

Figure 4.19: Artificial Setup to Neutral Zero Position before and after Surgery

The distance between femur and acetabulum in the superolateral side was also measured and the joint space before surgery was 5.4 mm and after 4.9 mm and can be rated as appropriate since Patient 2 is a male [197]. The values differ form each other which leads to the assumption, that the segmentation process was not accurate such as it was for Patient 1.

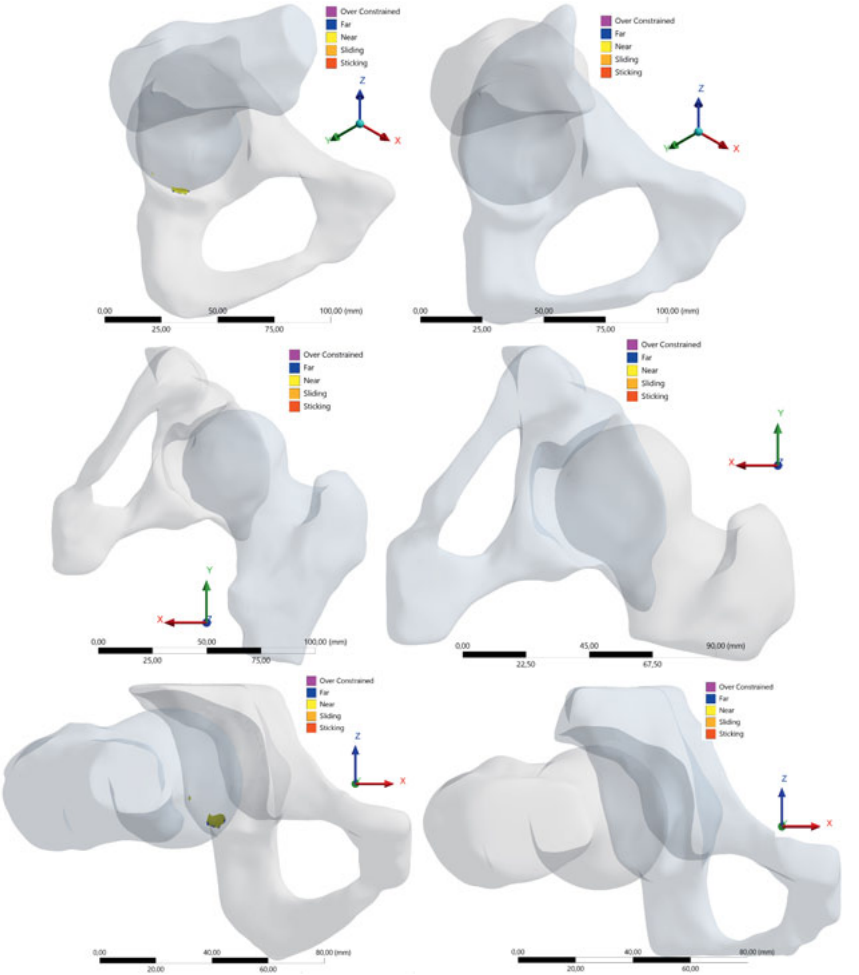

Figure 4.20: Status Modeling of Patient 2 Including Anteversion Rotation before and after Surgery

This and the fact of the low severity of the bony deformity could be a reason for the

unrecognizable detection of any narrowing. Hence, soft-tissues should be added into these simulations in the future to determine also the behavior of the labrum and the articular cartilages. Unfortunately, FEM software was not able to find a significant difference between both pre-surgery and post-surgery and, hence, a statement of the surgical outcome cannot be made. The assessment of the surgery can only be rated using the parameters, e.g., alpha angle etc. as described in Section 4.1.2.

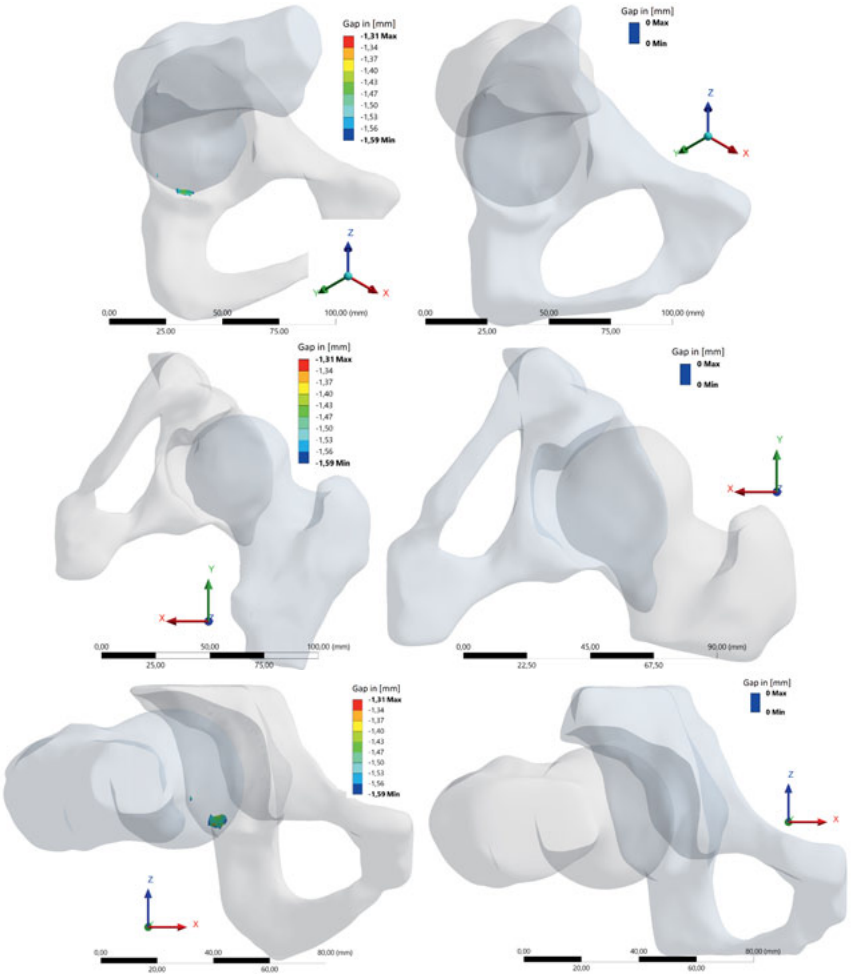

Figure 4.21: Gap Modeling of Patient 2 Including Anteversion before and after the Surgery

A bony contact could not be detected when simulating the impingement movement.

More important are simulations including soft tissue to properly understand the FAI and the Biomechanics of the hip joint. In the future, the MRI data quality must significantly increase to guarantee the best possible CAD model and, thus, a correct and most realistic simulation of the human hip joint. Most likely an improved statement of the performed surgery can also be given. This study discovered that the neutral zero position in the MRI is essential to eradicate errors, which cause an unrealistic simulation compared to the investigation by the physician.

4.1.4 Navigation assisted Planning of the Surgery

The removal of the bony part which causes the impingement can be planned using CAD simulations as a result of their fast calculation time. For this purpose, the angles which should be reached have to be implemented into the simulations, e.g., the angles should match those of the healthy joint. Additionally, a coordinate system including the maximum reached angle has to be inserted. Using the tool *Model → Get Data → Merge/Inheritance* in Creo, the impingement area can be evaluated. Hence, the model of the acetabulum including the standard coordinate system at the HJC and the new coordinate system of the femur are positioned and the overlapping volumina (red) is removed as visible in the Figure 4.22. The reduced femur model without the part, which causes the impingement, remains. With MIMICS® this area can be manually selected and integrated into the MRI data. This procedure is necessary to guarantee the best possible removal of bony deformity. The modified MRI data can be implemented into the navigation software used during the surgery.

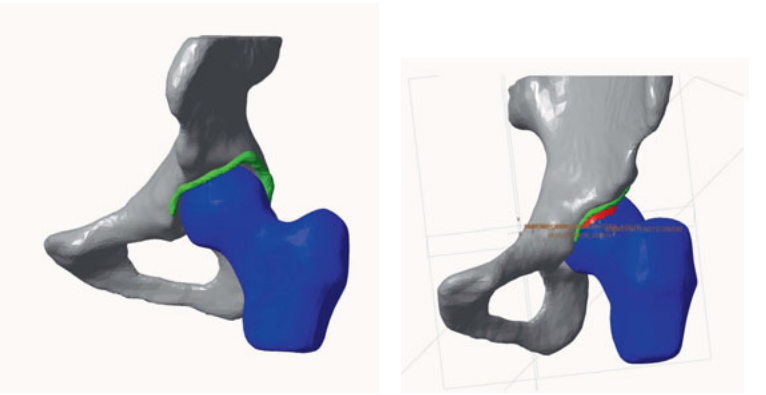

CAD Model | Simulated Model Including Contact

Figure 4.22: CAD Simulation for Determination of Bony Parts which must be Removed

4.2 Femur Head Necrosis

In this section simulations of the second disease, the FHN, are performed to calculate the optimized drilling with lowest stresses at the femoral neck and the starting point of the drilling.

4.2.1 Modeling

The MRI data were segmented using MIMICS®. Unfortunately, the standard MRI sequence for femoral head necrosis has a 3 mm slice thickness, which generates very rough surfaces as visible in Figure 4.23. The file size is about two megabytes. Hence, this segmentation is not an automatic process, errors can occur due to wrong interpretation of single areas in the slices. The experience of the researcher is of particular importance to state single structures of the human body. Acute parts of the bones may vanish due to the rough quality of the MRI data, which should be improved in the future.

After the segmentation process, the bone is smoothed using CAD software, which can cause additional deviation of the real human bone due to the fact that bony material may be added and/or removed as illustrated in Figure 4.24. This is important to obtain a good proportion between results and calculation time. After triangulation and editing, the file size increases to 150 megabyte and the calculation time of one drilling takes approximately one hour.

Figure 4.23: Manual Segmentation of a Necrotic Bone

The center of mass of the necrosis, which is the end point of the drilling, is calculated using different CAD software, such as Creo Parametric, SolidWorks and CATIA. These three softwares are compared with each other. The determined values are nearly identical as gathered in Table 4.16.

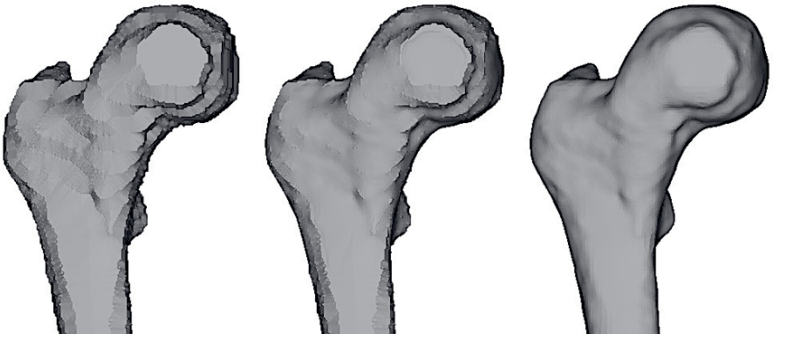

Figure 4.24: Example of the Smoothing Process

Table 4.16: Calculated Center of Mass of the Necrosis

Center of Mass	Creo Parametric	SolidWorks	CATIA
x-Coordinate [mm]	-92.42	-92.43	-92.43
y-Coordinate [mm]	-16.78	-16.78	-16.79
z-Coordinate[mm]	-4.28	-4.29	-4.29

4.2.2 Finite Element Method

The three-dimensional computer aided design models were generated from MRI and CT data as described in Section 3.3. The main reason for failure is the fracture of the bone after surgery, which mainly occurs at the femoral neck or at the drilling entrance point, because these areas affect the stability [183]. Thus, these regions were investigated with a principal stress component. The maximum value in these regions was determined and the ratio between those and the tensile strength of cortical bone was calculated [183]. Finite element simulations were performed for two conditions: regular walking and walking downstairs, such as described in the study of Tran et al. [183] with the load case as visible in Table 4.17.

Table 4.17: Hip Joint Forces [N] During Normal Walking [183]

Load Case	F_x	F_y	F_z	$\|F\|$
Normal Walking	−411.24	−247.1	2078.14	2132.8
Walking Downstairs	−411.29	−227.98	2212.37	2261.8

The material properties used are comparable to Tran et al. [183] A comparison between

both, a model exclusively of the cortical bone and a model of cancellous and cortical bone, is performed to determine the difference. For this purpose, the bony model is separated into these parts using CATIA. Supposedly, the cortical layer is 3 mm and, hence, this layer is subtracted from the upper bone layer, as visible in Figure 4.25. This procedure is only an approximation, but a manual segmentation process of both, cortical and cancellous bone is impossible and very time-consuming due to the MRI quality.

Figure 4.25: Separation of Cortical and Cancellous Bone

In Figure 4.26 the determined stresses of both, the model consisting of cortical and the model with both cortical and cancellous material properties, are visible; calculated for two Patients with 20 drilling each. As seen, the progress is similar, only the amount differs. In future studies, skipping such seperation significantly reduces the time-consumption of the process. More important is to identify the area with the lowest occurring stress and, for this purpose, a complete cortical bone suffices.

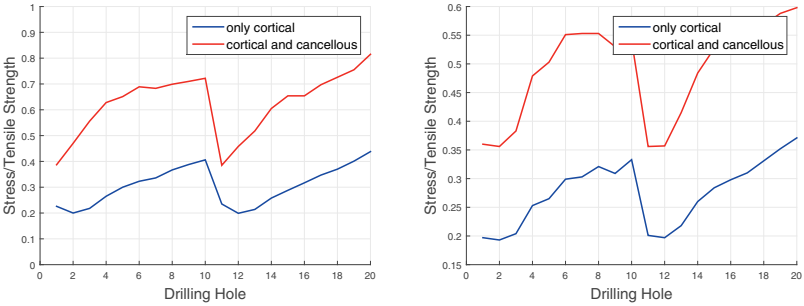

Figure 4.26: Examples for Stress Differences due to Material Properties

Generally, the results were similar compared to the results of Tran et al. [183], however,

it is also visible that the results depend on the geometry of the bone and the exact position of the necrosis. [183] A lot of different necrotic areas were generated and moved into arbitrary positions. Comparing simulation results of a model with and without cancellous bone, shows that the results only vary in the factor visible in Figure 4.26. However, to reduce time complexity, it is assumed that the bone entirely consists of cortical bone. The calculation time for each drilling takes around 50 min. In a second step, the simulations are parameter-controlled to define many different variations to calculate all occurring stresses more quickly. For this purpose, an area of interest is set to determine the entrance points for the drilling as visible in Figure 4.27.

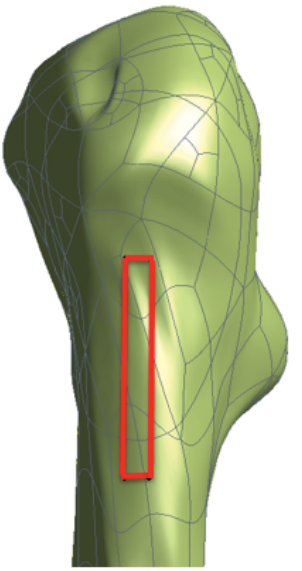

Figure 4.27: Area of Interest for drilling entrance points

In Figure 4.28 the optimal drilling regarding minimal stresses is illustrated. An optimization of this method is possible using the Tool *Response Surface* in ANSYS DesignXplorer. The results show the more the drilling diverges to the distal end of the femur, the higher are the occurring stresses and, hence, worse for the patient (negative z-axis). The optimization method is Screening and generates 1000 Examples and discovers 3 optimal candidates by a direct sampling method using a pseudo-random number. In Table 4.18 the determined quotients of calculated principle stress and maximum tensile strength for cortical bone are visible.

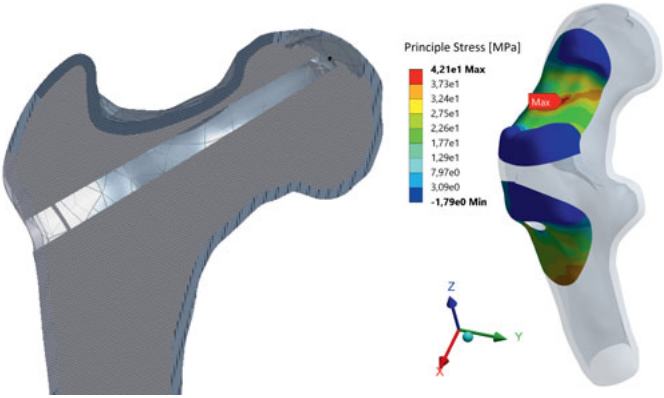

Figure 4.28: Example for an Optimal Drilling and the Occurring Stresses

Table 4.18: Example for Calculated Stresses Quotient During Normal Walking and Downstairs Walking

	Normal Walking	Walking Downstairs
Untreated	0.66	0.81
(0,-10)	0.67	0.83
(0, 0)	0.67	0.82
(0, 10)	0.67	0.83
(0, 20)	0.68	0.84
(0, 30)	0.68	0.83
(5, -10)	0.67	0.82
(5, 0)	0.67	0.83
(5, 10)	0.68	0.83
(5, 20)	0.68	0.83
(5, 30)	0.69	0.85

4.2.3 Neural Network

As of today, over 190 different necrosis-simulations were performed. All FEM results are included into the neural network to predict the stresses when the center of necrosis is given. A system is developed, which can predict the stress when the center of the necrotic lesion is given. For this purpose, H2O deep learning models are used, which promise fast,

scalable, open-source machine learning and deep learning [190]. This machine is a multi-layer neural network with backpropagation and contains many different machine learning algorithms, such as generalized linear modeling, principal components analysis, k-means clustering, etc. [190]. The complete data was split into two different sets, the training set and testing set, and was input into the library. The results are given in Figure 4.29. As it can be seen, the relative error of the predicted stresses for the new data (red points) at the entrance point is under 1% and at the femoral neck under 2%, which is very accurate.

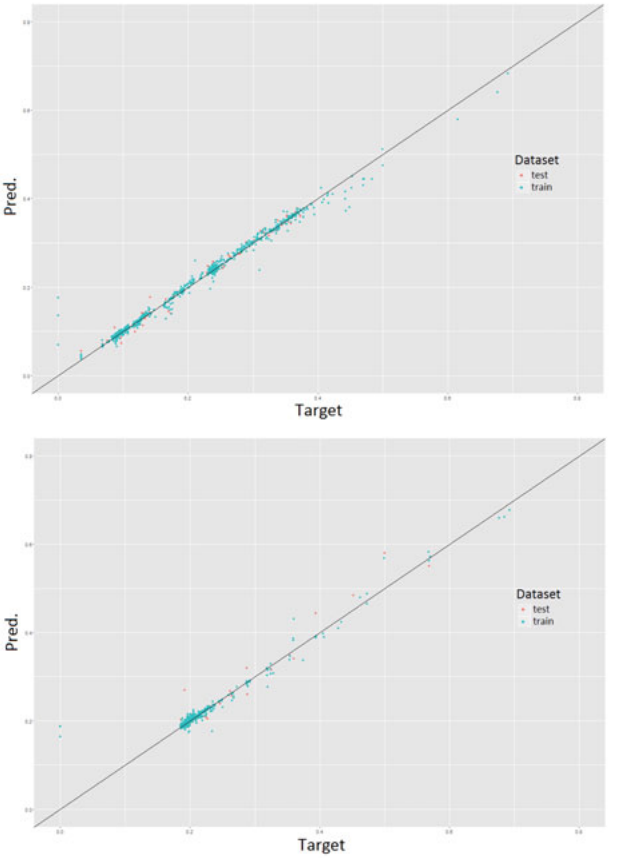

Figure 4.29: Neural Network Results for Entrance Point Drilling and Femoral Neck

In the future, with the known geometry of the surgery tool which is used to remove the necrotic material, a software could be developed which shows the optimal drilling with regard to the best possible removal of the necrotic material. In combination with

FEM simulations, the lowest stress can be integrated into the software and the system can calculate the optimal drilling with respect to lowest stress and maximum removal.

As visible in Figure 4.29, the results show a linear regression and both, the stresses at the entrance point of the drilling and at the femoral neck, are predictable for this bone. A further step is to include more bones and to check, whether these results can be generalized.

Another developed software can calculate the optimal drilling with respect to the best possible removal of the necrotic area as seen in Figure 4.30. The geometry of the surgery equipment is implemented and the software verifies the conformity of both volumina to ensure a proper removal. The last step is a combination of both systems.

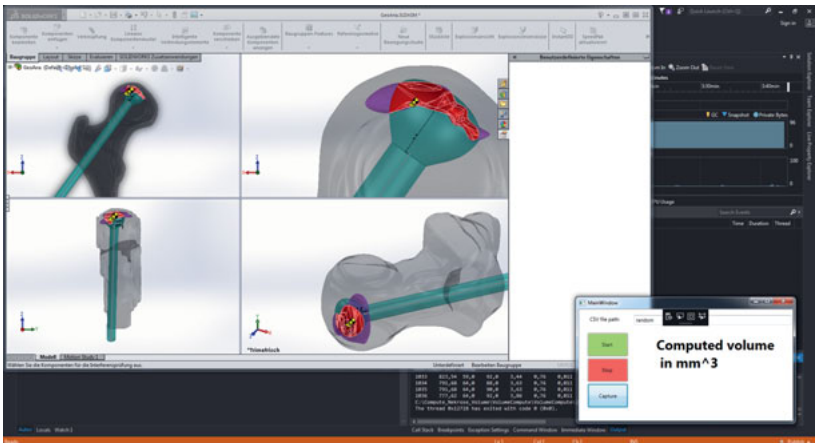

Figure 4.30: Software Calculates the Most Possible Removal of Necrotic Area

In a last step, the calculated optimal drilling can be transferred into X-ray data. The model including the drilling channel is exported as STL file to MIMICS® into the MRI data set of the patient, as illustrated in Figure 4.31. Subsequently, the results of the simulation are implemented into Creo Parametric.

Thus, the used standard during the surgery is the anteroposterior (AP) and Lauestein view, to perform the surgery, the drilling core should also be inserted into these views. In Figure 4.32 the difference between the mechanical optimal drilling and a medical optimal drilling is shown. In the AP view, the simulated drilling channel, illustrated in blue, differs with 11° proximal compared with the performed one. The deviation in the Lauenstein view is around 4° in ventral direction.

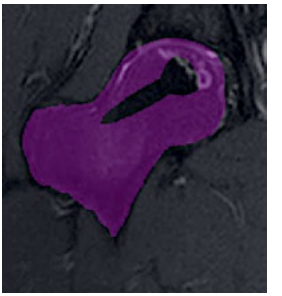

Figure 4.31: Model Including Drilling is Imported to MIMICS®

Some limitations still occur in this transfer, e.g., the right layer in which the X-ray image is taken, cannot be determined and, thus, the positioning of the simulated drilling into the X-ray images is only approximated. It is nearly impossible to get a complete accurate congruence. The presented example shows an optimal drilling for this patient under mechanical conditions, not under medical conditions illustrated in a blue color. Hence, the muscle gluteus medius starts at the greater trochanter, the drilling cannot be performed as the simulation result shows.

In comparison with the results of the compression test, the use of FEM is reasonable to predict occurring stresses in a human hip joint by a drilling into the femoral head while loading with the force, which acts during normal walking or downstairs walking. However, to ensure more accurate models of the femur an improved quality of MRI data is required.

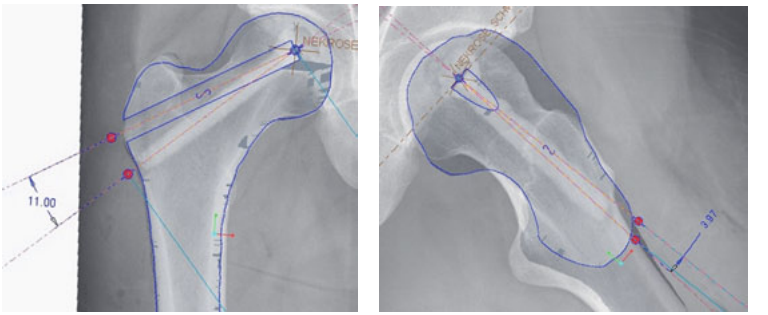

AP View Lauenstein View

Figure 4.32: Transfer of the Optimal Drilling to X-Ray Data Including Performed Surgery

5 Conclusions and Outlook

Finally, in this section the conclusions of this thesis are presented and the remaining challenges for future work will be introduced. The most popular treatment for hip diseases is the hip arthroscopy, which enables small access to the joint and, thus, a minimal damage of the surrounding tissue. A arthroscopic treatment of FAI and FHN is not the standard procedure, however, it would have advantages.

The bony abnormality of the cam-type impingement as well as the removal of the necrotic area due to a femoral head necrosis can be treated using this minimal invasive approach. In this dissertation the modeling of the hip joint including the bony deformity or the necrotic lesion and the simulation of the movement or the stability were performed. As a consequence, an improved understanding of the biomechanical background of these diseases could be generated.

5.1 Femoroacetabular Impingement

The generated FAI model should help to propose each patient an individual concept of their disease and, thus, a better surgical treatment. Additionally, another objective of this thesis was to evaluate the performed surgical treatment by using pre-surgery and post-surgery patient data and the corresponding motion analysis data.

Initially, various software is used to generate a patient specific 3D model based on MRI data. A manual segmentation process is very time-consuming and, besides, inaccurate models are a consequence when compared to models based on MRI data. Model consistency is lost due to smoothing algorithms, which are necessary to get appropriate models (cf. Section 4.1.1).

Both, pre-surgical and post-surgical data of two patients were obtained from the scanning process to develop suitable patient specific 3D models. It was noted that one issue is the slice thickness of 1.5 mm of the MRI data, which leads to rough surfaces and unfortunately to inaccurate 3D models, hence, not all joint parts could be segmented and subtle details, such as the labrum, were not identified for every patient. In future work, it is important to decrease the slice thickness to approx. 1.0 mm or less to get more appropriate models and, thus, better simulations results. Joint parts, such as the cartilage and labrum could be segmented more easily. Another issue can be introduced by contrast agents, which might also lead to better joint models. Nevertheless, the generated models were rated to be of sufficient quality for the desired task by visual appearance of radiologists.

For evaluation of the severity of cam-type FAI, the offsets and alpha angles were measured on both MRI and 3D models for two patients. The comparison of both methods show significant differences by the subjective measuring execution and a poor segmenta-

tion quality due to bad MRI quality. Nevertheless, the measurements on the 3D model were easier to process due to the helpful measurement tools in the used software and, hence, in future studies it is sufficient to only rely on this method to reduce the required time.

Many parameters could be determined using the MRI data and the 3D models, e.g., the hip joint center, femoral neck axis etc. (cf. Section 4.1.2). Control methods, e.g., a motion envelope tool to show the reliability of the hip joint center, prove a good quality of the determination method. During the determination of the offset and alpha angle values of the pre-and post-surgery patients, the alpha angle established as the more reliable parameter to assess the FAI. The offset shows no significant indication in the evaluated cases, but in the future, more cases have to be analyzed to perform a patient study. The alpha angle for Patient 2 decreases after the surgery which can be evaluated as a positive surgical outcome whereas the values of Patient 1 hardly changed. This can be explained by a sub-optimal surgical outcome, however, the patient remained free of pain during the investigation after the surgical intervention.

CAD simulations show an easier handling and shorter calculation times compared with FEM simulations, however, occurring stresses can only be calculated using FEM (cf. Section 4.1.3). Consequently, determination of maximal angles and collision positions can be performed using CAD software.

Simulations of all patients show no bony contact between femoral neck and acetabulur rim, which leads to the hypothesis that soft-tissue is the reason for pain and limitation of movement. Subsequently, the labrum was implemented into one example, in which the MRI data quality was good enough to segment this part. The results of this simulation show a contact which corresponds to the angle area, in which the patient had pain during the investigation. Hence, the FAI mechanism is a squeezing of the soft-tissue due to the bony deformation, which generates pain and limitation of movement for the patient (cf. Section 4.1.3.2).

Afterwards, the modeling and simulation were performed. With the determined angles of the motion analysis, the simulations could be controlled. Unfortunately, there were essential differences in the results for the determined angles for the patients which are compared before and after the surgery. Patient 1 shows no internal rotation which can be related to a measuring error in the gait lab, a calibration error of the equipment, or a performance mistake during the investigation. This caused a non-narrowing of the bony parts, acetabulum and femur. However, since pain could not be detected during the physical investigation, the results of the simulation can be rated as good and realistic. The surgical outcome cannot be evaluated. With an adjusted simulation including the internal rotation, a narrowing of femur and acetabulum could be detected and the impingement

area decreased after the surgical intervention, but did not entirely disappear. From this standpoint, the minor changes of the alpha angle are supported. Bearing in mind the determined parameters and the simulation results, the surgical outcome can be rated as good for Patient 1.

In the simulation of Patient 2, no approximation of femur and acetabulum can be detected, although the pain sensor was triggered during the investigation and, especially, during the impingement test. For both patients, the neutral zero position during the MRI investigation was not considered and, thus, the internal rotation may also be too brief as well as in the case of Patient 1. To eliminate this error, a larger degree of the internal rotation was applied by considering the anteversion of the femur and, hence, to assume the neutral zero position at the beginning of the simulation. Even during this adjusted simulation no bony impingement could be determined. A reason for that could be the large joint space width of this patient or, additionally, a low severity of the cam deformity. Unfortunately, the simulation could not evaluate the surgical outcome, but with the results of the determined parameter, the alpha angle, a positive surgery could be noted.

Furthermore, all performed simulations of FAI in this dissertation never showed an entirely bony contact during the cam-type impingements, which leads to the hypothesis that a cam-type FAI is caused by a squeezed soft tissue because of the bony deformity.

Concluded, several issues affect the results of this study, such as the performance of the MRI scan, the segmentation process of the hip joint parts, and the measurement of the angles in the gait lab. More reliable results of the simulation could be generated by eliminating these errors. The results of this study can be used to determine the exact removal of the deformity, such that the labrum is not squeezed anymore.

Prospectively, all simulations regarding FAI should be performed including soft tissue, especially the labrum, which is a main component in the Biomechanics of the FAI. Additionally, MRI data quality and neutral zero position are essential to generate the real movement of the investigated movements in the gait lab. Probably, a new standard to evaluate the FAI should be postulated to enhance the alpha angle, which measurements are currently very subjectively and inaccurate.

Even more, a patient study and automatism of the whole procedure would be helpful to implement a new standard in the treatment of FAI.

5.2 Femur Head Necrosis

As of today, the disease of femur head necrosis is not entirely cleared up. The generated FHN model should help to develop a new approach to treat this disease. Thereby, the best possible surgical outcome with view on mechanical properties should be obtained due to the drilling. Furthermore, the most possible necrotic removal should be performed to

guarantee a healing for the patient without a THR. The ACD is a proper method of this treatment due to the minimal invasive approach.

Initially, MRI and CT data are manually segmented and 3D models are generated to perform FEM simulations including the drilling channels (cf. Section 4.2.1). Unfortunately, the medical standard MRI sequence for femur head necrosis contains 3 mm slice thickness, which result in very rough STL models. Irregularities and error may occur, why post-processing is mandatory. In future studies, the aim should be to decrease the slice thickness and to get more appropriate models to ensure less post-processing and more exact 3D models and, thus, more reliable simulation results. The calculated stresses and positions of these may slightly change. Using CT data, the segmentation process can be preformed more easily due to threshold tools, which use additional information, e.g., density to exclude the needed tissues from each other. Unfortunately, the radiation of CT is harmful and, hence, the MRI should be used in the future.

In the following, the center of mass of the necrotic area is determined using CAD software, which is equal to the endpoint of the drilling (cf. Section 4.2.1). The center was determined by multiple CAD softwares and showed very similar results. With this calculated center of mass of the necrotic area, the untreated and the treated models, including the drilling channels with changing entrance points, were generated. For this purpose, a coordinate system was placed at the greater trochanter, which controls the variations of the entrance points. Several models could be generated to perform the simulations. In a further step, the generation of the drilling channels was automatically controlled by a parameter-controlled function of ANSYS. This method has the advantage that the calculation-time is minimized due to the fact that instead of generating each drilling model, only the values are calculated.

In the FEM simulations, the bones were loaded in two different conditions: the normal walking and the downstairs walking (cf. Section 4.2.2). The determination of the stresses was focused on the femoral neck and the entrance point of the drilling, because the failure mechanism most often occur in these positions. The ratio of the calculated stresses and the tensile strength to assume the failure risk. The lowest value represent the best drilling under mechanical conditions, which often is in the area of the greater trochanter and, hence, at the starting point of the muscle gluteus medius, which is under medical conditions not the optimal entrance point, because the muscle is devitalized. Subsequently, the optimal drilling point is the area directly under the greater trochanter, such as confirmed by Tran et al. [183]. The determined drilling can be transformed into the AP and Lauenstein views of X-rays using the segmentation software. More than 190 simulations were performed with varying center of mass, size and form of the necrosis. Moreover, with the use of the parameter-controlled simulations, it is possible to speed-up the complete simulation

process and generate more data and, hence, develop a suitable system for predicting the occurring stresses due to drilling in the femur.

Furthermore, the results of these simulations were implemented into a for this purpose generated neural network, which is able to predict occurring stresses without calculating them (cf. Section 4.2.3). It shows a proper correlation of the predicted stresses with new necrosis. Additionally, a software was created to determine the optimal drilling angle regarding the best possible removal. In the future, a combination of both systems and a generalization of this procedure is necessary to implement this method as a standard treatment for femoral head necrosis and to optimize the success rate for patients. In this case, a patient study is also necessary to validate the results.

6 Appendix

In this section the Motion Capture data is presented used to control the simulation.

6.1 MoCap Data

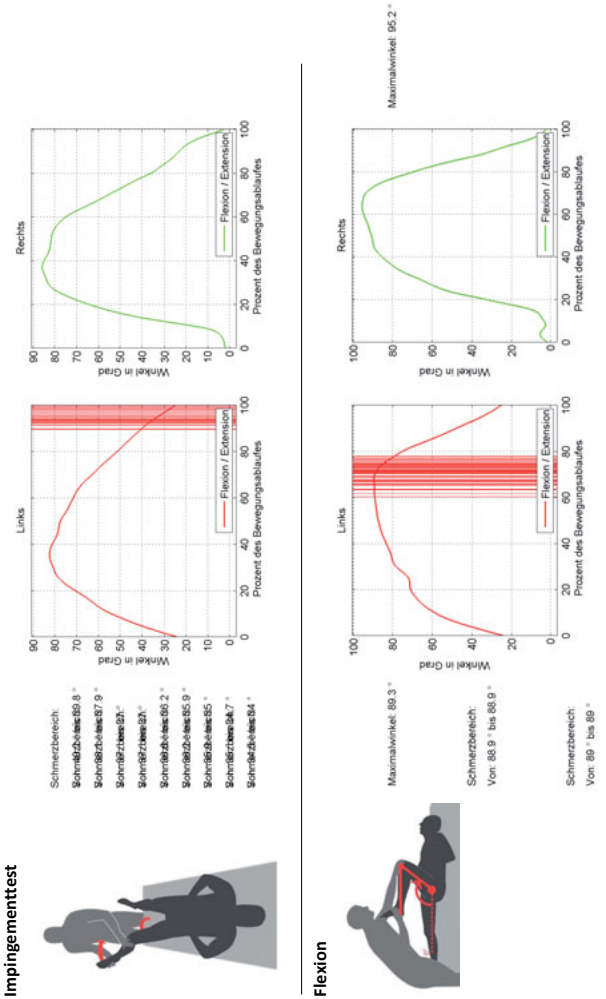

Figure 6.1: Example of Report Generated From the MoCap Analysis: Impingementtest and Flexion

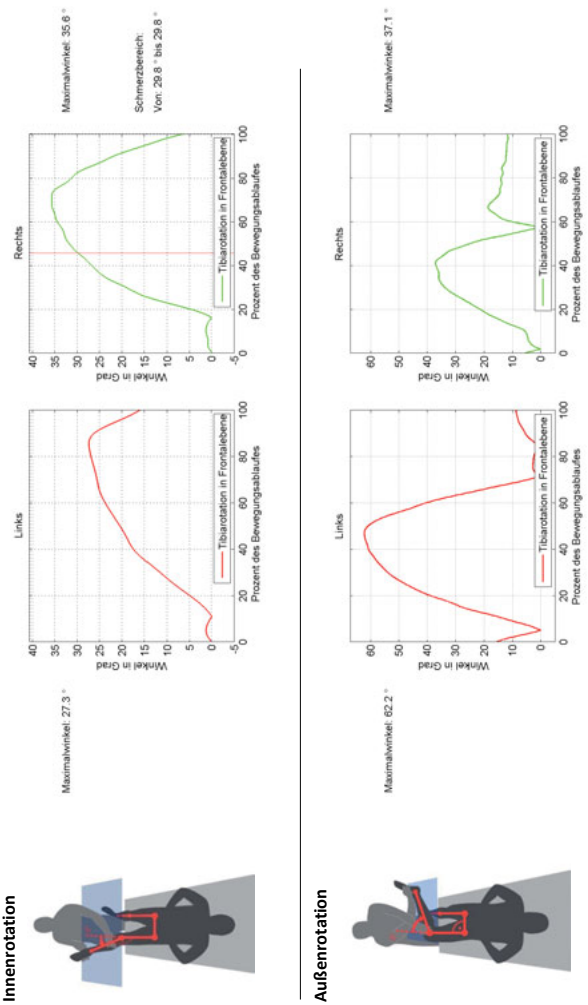

Figure 6.2: Example of Report Generated From the MoCap Analysis: Internal- and External Rotation

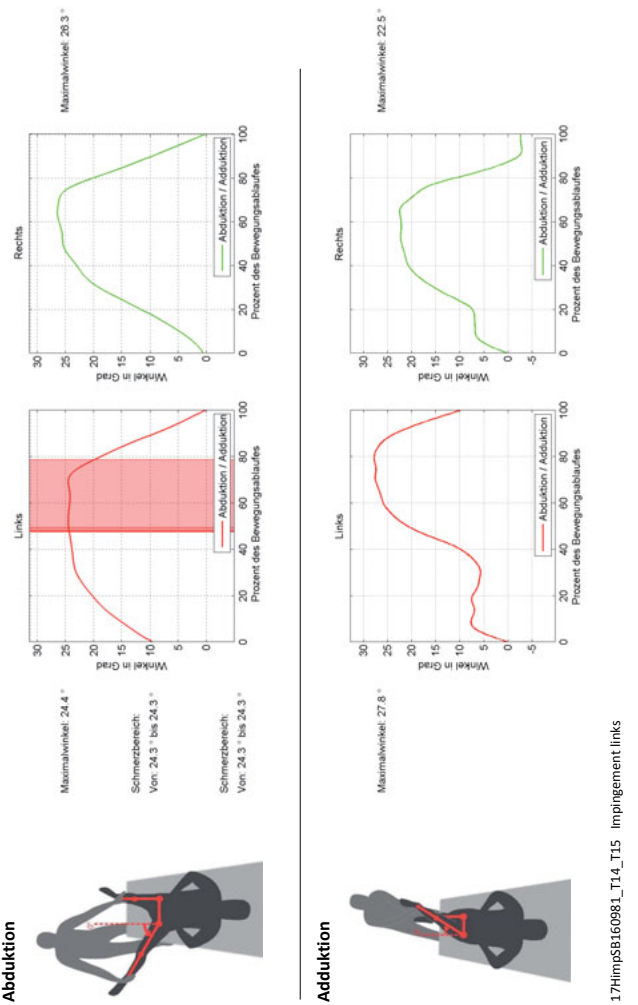

Figure 6.3: Example of Report Generated From the MoCap Analysis: Abduction and Adduction

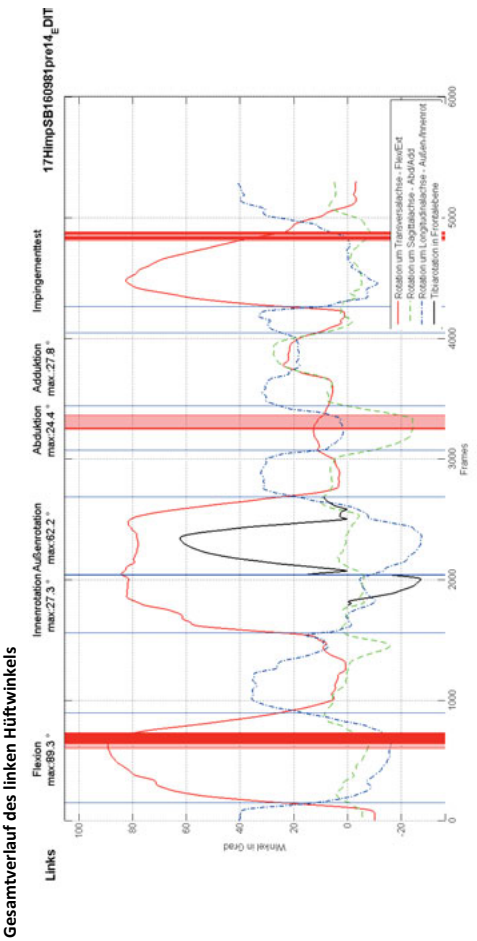

Figure 6.4: Example of Report Generated From the MoCap Analysis: Complete Movement (left)

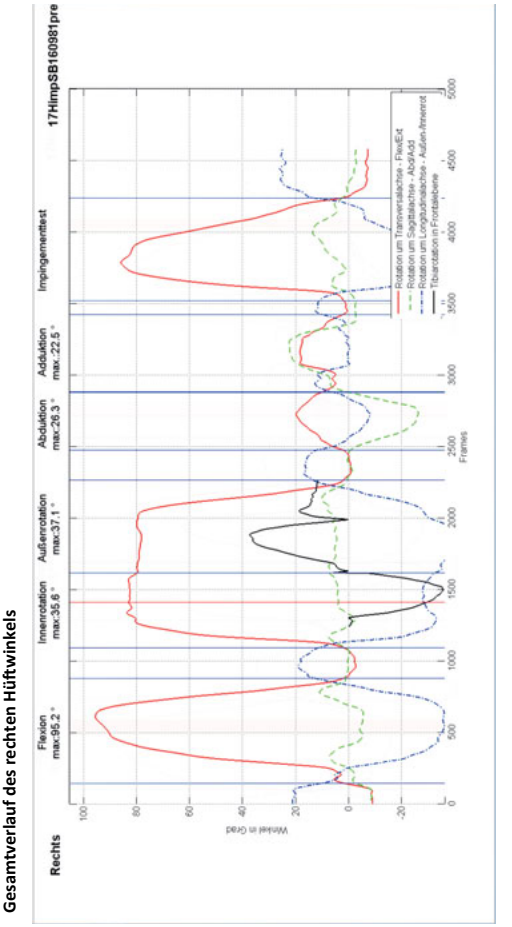

Figure 6.5: Example of Report Generated From the MoCap Analysis: Complete Movement (right)

6.2 Neural Network

In this section the code of the neural network is listed.

```
h2o_deeplearning <- function(m2, layer, epochs, y = "B2", nfolds = 0){

  model <- h2o.deeplearning(x = 2:m2$cols, y = 1,
                            hidden = layer,
                            activation = "Rectifier",
                            epochs = epochs,
```

```
                        nfolds = nfolds,
                        l1=1e-05,
                        training_frame = as.h2o(m2$train),
                        validation_frame = as.h2o(m2$test)
                        )
  file <- h2o.saveModel(model, path=getwd())
  #predict test set
  m2.pred_test <- as.matrix(h2o.predict(model, as.h2o(m2$test)))
  m2.pred_train <- as.matrix(h2o.predict(model, as.h2o(m2$train)))

  #plot
  line1 <- geom_abline(intercept = 0, slope = 1)

  m2.plot_data_train <- data.frame(m2$test[y], m2.pred_test, "test")
  colnames(m2.plot_data_train) <- c("target","pred", "dataset")
  m2.plot_data_test <- data.frame(m2$train[y],m2.pred_train, "train")
  colnames(m2.plot_data_test) <- c("target","pred", "dataset")

  rmse_train = RMSE(m2$train[y], m2.pred_train)
  rmse_test = RMSE(m2$test[y], m2.pred_test)

  m2.plot_data <- rbind(m2.plot_data_train, m2.plot_data_test)
  plot <- ggplot(m2.plot_data, aes(x=target, y=pred, color=dataset)) +
   geom_point() + line1 +
   ggtitle(paste("rmse_test=", rmse_test, "␣rmse_train=", rmse_train))

  ans <- list("model" = model,
              "rmse_train" = rmse_train,
              "rmse_test" = rmse_test,
              "file" = file,
              "plot" = plot)
  }

h2o_predict_plot <- function(model, m2, y){
  #predict test set
  pred <- h2o.predict(model, as.h2o(m2$data))
  m2.pred_data <- as.matrix(h2o.predict(model, as.h2o(m2$data)))

  #plot
  line1 <- geom_abline(intercept = 0, slope = 1)

  m2.plot_data<- data.frame(m2$data[y], m2.pred_data, "data")
  colnames(m2.plot_data) <- c("target","pred", "dataset")

  rmse_data = RMSE(m2$data[y], m2.pred_data)

  plot <- ggplot(m2.plot_data, aes(x=target, y=pred, color=dataset)) +
    geom_point() + line1 + ggtitle(paste("rmse=", rmse_data))

  ans <- list( "rmse_data" = rmse_data,
              "pred" = pred,
              "plot" = plot)
}

h2o_predict_train_plot <- function(model, m1, m2, y){
  #predict test set
```

```
  pred <- h2o.predict(model, as.h2o(m2$data))
  m2.pred_data <- as.matrix(h2o.predict(model, as.h2o(m2$data)))

  #predict train set
  pred <- h2o.predict(model, as.h2o(m1$data))
  m1.pred_data <- as.matrix(h2o.predict(model, as.h2o(m1$data)))

  #plot
  line1 <- geom_abline(intercept = 0, slope = 1)

  m.plot_data_train<- data.frame(m1$data[y], m1.pred_data, "train")
  colnames(m.plot_data_train) <- c("target","pred", "dataset")

  m.plot_data_test<- data.frame(m2$data[y], m2.pred_data, "test")
  colnames(m.plot_data_test) <- c("target","pred", "dataset")

  m.plot_data <- rbind(m.plot_data_train, m.plot_data_test)
  rmse_data = RMSE(m2$data[y], m2.pred_data)

  plot <- ggplot(m.plot_data, aes(x=target, y=pred, color=dataset)) +
    geom_point() + line1 + ggtitle(paste("rmse_test=", rmse_data))

  ans <- list( "rmse_data" = rmse_data,
               "pred" = pred,
               "plot" = plot)
}

RMSE = function(m, o){
  sqrt(mean((m - o)^2))
}
```

Listing 1: R-Code: h2o_run.R

```
library(caret)
SplitData <- function(dataset, random = TRUE, s1 = 0, s2 = 0){

  #create normalize data
  #train consists 70% data
  #valid consists 30% data, splits into test 15% and cross 15%
  data <- dataset
  cols <- ncol(data)
  if (random)
  data <- data[sample(1:nrow(alldata)), ]
  s <- scale(data)
  if (s1 == 0 || s2 == 0){
  s1 <- attr(s, 'scaled:scale')
  s2 <- attr(s, 'scaled:center')
  }
  data_s <- data
  for (i in 1:nrow(data))
  {
    data_s[i,] <- (data[i,] - s2) / s1
  }

  #test
  indexTrain <- createDataPartition(y=data[,1], p=0.8, list=FALSE)
  train <- data[indexTrain,]
```

```
  valid <- data[-indexTrain,]
  train_s <- data_s[indexTrain,]
  valid_s <- data_s[-indexTrain,]
  indexValid <- createDataPartition(y=valid[,1], p=0.5, list=FALSE)
  test <- valid[indexValid,]
  cross <- valid[-indexValid,]
  test_s <- valid_s[indexValid,]
  cross_s <- valid_s[-indexValid,]

  ans <- list("data" = data,
        "train" = train,
        "test" = test,
        "cross" = cross,
        "cols" = cols,
        "s" = s,
        "s1" = s1,
        "s2" = s2,
        "data_s" = data_s,
        "train_s" = train_s,
        "test_s" = test_s,
        "cross_s" = cross_s,
        "valid_s" = valid_s,
        "valid" = valid)
  return(ans)
}
```

Listing 2: R-Code: SplitData.R

```
source("SplitData.R")
source("h2o_run.R")

# import data set.seed(703)
alldata <- read.table("data6_train.tsv", sep="\t")

# label names to the columns in the tsv (tab sparated values )file
colnames(alldata) <- c("Sample","Sx","Sy","Sz","Bx","By","Bz","Dx","Dy",
  "Dz","Alpha","Beta","H1","B1","Rad", "Ex", "Ey", "Ez",
  "Volume","Ky","Kz","H2","B2")

target = "B2"
# parameters to use in the NN model
m2 <- SplitData(alldata[, c(target, "Sx","Sy","Sz","Dx", "Dy", "Dz", "Alpha",
  "Beta", "Ex", "Ey", "Ez", "Volume")]) #this is for B2

library(h2o)

hidden <- c(200,200,100)

set.seed(467382)

for (i in 1:10){
  #random number of hidden layers nodes
  h1 <- sample(20:200, 1)
  h2 <- sample(20:200, 1)
  h3 <- sample(20:100, 1)
  hidden <- c(h1, h2, h3)

```

```
  #500 is the epochs number, means the number of iteration, lower faster
  model <- h2o.deeplearning(m2, hidden, 500, y = target)

  output <- paste(target, "␣", toString(hidden), "␣", model$rmse_test, "␣",
    model$rmse_train, "␣",     model$file)
  print(output)
  png(filename = paste(model$file,".png"), width = 1200, height = 800)
  print(model$plot + xlim(0,0.8) + ylim(0,0.8))
  dev.off()
  write(output, file = "log.txt", append = TRUE)
}
```

Listing 3: R-Code: FindBestModel.R

```
source("SplitData.R")
source("h2o_run.R")
setwd("C:/Nekrose_Deep_Learning")

set.seed(703)

column <- c("Sample","Sx","Sy","Sz","Bx","By","Bz","Dx","Dy","Dz","Alpha",
  "Beta","H1","B1","Rad", "Ex", "Ey", "Ez", "Volume","Ky","Kz","H2","B2")
#With volume
alldata <- read.table("data7_new.tsv", sep="\t")
colnames(alldata) <- column
#make sure parameters are the same as the models,
  #which is on line 12-13 in FindBestModel.R
mB <- SplitData(alldata[, c("B2", "Sx","Sy","Sz","Dx", "Dy", "Dz",
  "Alpha", "Beta", "Ex", "Ey", "Ez", "Volume")], random = FALSE)

#With volume
alldata2 <- read.table("data6_train.tsv", sep="\t")
colnames(alldata2) <- column
mB_train <- SplitData(alldata2[, c("B2", "Sx","Sy","Sz","Dx","Dy", "Dz",
  "Alpha", "Beta", "Ex", "Ey", "Ez", "Volume")], random = FALSE)

library(h2o)

path = paste(getwd() , "/" ,
  "DeepLearning_model_R_1484828216151_7", sep = "")
print(path)
modelB <- h2o.loadModel(path)
resB <- h2o_predict_train_plot(modelB, mB_train, mB, "B2")
h2o.exportFile(resB$pred, "resB.csv", force=TRUE)
print(resB$plot)
```

Listing 4: R-Code: main_h2o.R

```
library(h2o)
h2o.init(nthreads=7)
```

Listing 5: R-Code: main_start_h2o.R

```
# testmodel
set.seed(703)
alldata <- read.table("data4.tsv", sep="\t")
colnames(alldata) <- c("Sample","Sx","Sy","Sz","Bx","By","Bz","Dx",
```

```
  "Dy","Dz","Alpha","Beta","H1","B1","Rad","Ky","Kz","H2","B2")
m2 <- SplitData(alldata[, c("B2", "Sx","Sy","Sz","Dx", "Dy", "Dz",
  "Alpha", "Beta", "Rad")])

# load model
model <- h2o.loadModel("D:\\Projects\\NekroseNN\\
␣␣DeepLearning_model_R_1471440561092_132")

m2.pred_test <- as.matrix(h2o.predict(model, as.h2o(m2$test)))
m2.pred_train <- as.matrix(h2o.predict(model, as.h2o(m2$train)))
m2.pred_cross <- as.matrix(h2o.predict(model, as.h2o(m2$cross)))

# parameters used in the test, train and cross
m2.plot_data_train <- data.frame(m2$test["B2"], m2.pred_test, "test")
colnames(m2.plot_data_train) <- c("target","pred", "dataset")
m2.plot_data_test <- data.frame(m2$train["B2"],m2.pred_train, "train")
colnames(m2.plot_data_test) <- c("target","pred", "dataset")
m2.plot_data_cross <- data.frame(m2$cross["B2"],m2.pred_cross, "cross")
colnames(m2.plot_data_cross) <- c("target","pred", "dataset")

rmse_train = RMSE(m2$train["B2"], m2.pred_train)
rmse_test = RMSE(m2$test["B2"], m2.pred_test)
rmse_cross = RMSE(m2$cross["B2"], m2.pred_cross)

# plot
line1 <- geom_abline(intercept = 0, slope = 1)
m2.plot_data <- rbind(m2.plot_data_train,
  m2.plot_data_test, m2.plot_data_cross)
plot <- ggplot(m2.plot_data, aes(x=target, y=pred, color=dataset)) +
  geom_point() + line1 + ggtitle(paste("rmse_test=", rmse_test,
  "␣␣rmse_train=", rmse_train, "␣rmse_cross=", rmse_cross))
print(plot)
png(filename = paste("cross_validation_test2.png"), width = 1200, height = 800)
print(plot + xlim(0,0.5) + ylim(0,0.5))
dev.off()
```

Listing 6: R-Code: main_testmodel.R

References

[1] H. A. Richard and G. Kullmer, *Biomechanik: Grundlagen und Anwendungen auf den menschlichen Bewegungsapparat.* Springer-Verlag, 2014.

[2] J. J. Callaghan, A. G. Rosenberg, and H. E. Rubash, *The adult hip.* Lippincott Williams & Wilkins, 2007, vol. 1.

[3] F. Pauwels, *Biomechanics of the Normal and Diseased Hip: Theoretical Foundation, Technique and Results of Treatment An Atlas.* Springer Science & Business Media, 2012.

[4] P. K. Levangie and C. C. Norkin, *Joint structure and function: a comprehensive analysis.* FA Davis Philadelphia, PA, 2001.

[5] ——, *Joint Structure and Function: A Comprehensive Analysis Fifth Edition.* F.A. Davis Company, 2011.

[6] P. K. Levangie, "Biomechanical applications to joint structure and function," *Joint structure and function: A comprehensive analysis*, pp. 15–20, 2005.

[7] A. Schäffler and S. Schmidt, "Medizin und gesundheit," *Naumann & Göbel GmbH*, 2003.

[8] D. A. Neumann, *Kinesiology of the musculoskeletal system: foundations for rehabilitation.* Elsevier Health Sciences, 2013.

[9] F. U. Niethard, J. Pfeil, and K. Birnbaum, *Orthopädie.* Thieme Stuttgart, 2003.

[10] L. Claes, P. Kirschner, C. Perka, and M. Rudert, *Ae-Manual Der Endoprothetik Hufte Und Huftrevision.* Springer-Verlag, 2012.

[11] S. Ferguson, J. Bryant, R. Ganz, and K. Ito, "An in vitro investigation of the acetabular labral seal in hip joint mechanics," *Journal of biomechanics*, vol. 36, no. 2, pp. 171–178, 2003.

[12] R. N. B. et al.., *Joint Range of Motion and Muscle Length Testing, 2nd Edition.* Saunders, 2010.

[13] Kummer, *Biomechanik:.* Deutscher Ärzte-Verlag, 2005.

[14] Óliver Marín-Pena, *Femoroacetabular Impingement.* Springer, 2012.

[15] P. Sommerfeld, *Biomechanik der menschlichen Gelenke.* Urban & Fischer bei Elsev, 2004.

[16] R. Putz, I. U. Simon, H. P. Nötzli, T. F. Wyss *et al.*, "Funktionelle anatomie und biomechanik," in *AE-Manual der Endoprothetik*. Springer, 2012, pp. 21–45.

[17] K. Zilles and B. Tillmann, *Anatomie*. Springer-Verlag, 2010.

[18] P. Augat, "Biomechanik des becken-bein-Übergangs," *Trauma und Berufskrankheit*, vol. 13, no. 1, pp. 92–96, 2011.

[19] R. W. Bohannon, "Number of pedometer-assessed steps taken per day by adults: a descriptive meta-analysis," *Physical Therapy*, vol. 87, no. 12, p. 1642, 2007.

[20] M. Morlock, E. Schneider, A. Bluhm, M. Vollmer, G. Bergmann, V. Müller, and M. Honl, "Duration and frequency of every day activities in total hip patients," *Journal of biomechanics*, vol. 34, no. 7, pp. 873–881, 2001.

[21] B. Schlink, M. Wimmer, and K. Foucher, "Hip motion patterns are associated with disease severity and reduced dynamic loading in hip osteoarthritis," in *ORS Annual Meeting*, 2011.

[22] Hochschild, *2: LWS Becken und Hüftgelenk Untere Extremität*. Thieme Georg Verlag, 2012.

[23] M. Hughes, Hsu, "Hip anatomy and biomechanics in the athlete," *Sports Medicine and Arthroscopy Review*, vol. 10, pp. 103–114, 2002.

[24] G. Bergmann, G. Deuretzbacher, M. Heller, F. Graichen, A. Rohlmann, J. Strauss, and G. N. Duda, "Hip contact forces and gait patterns from routine activities," *J Biomech*, vol. 34, no. 7, pp. 859–871, Jul 2001.

[25] J. Clohisy, P. Beaule, and C. DellaValle, *The Adult Hip*. Wolters Kluwer Health, 2015.

[26] B. F. Ricciardi, P. D. Fabricant, K. G. Fields, L. Poultsides, I. Zaltz, and E. L. Sink, "What are the demographic and radiographic characteristics of patients with symptomatic extraarticular femoroacetabular impingement?" *Clinical Orthopaedics and Related Research®*, vol. 473, no. 4, pp. 1299–1308, 2015.

[27] R. Ganz, M. Leunig, K. Leunig-Ganz, and W. H. Harris, "The etiology of osteoarthritis of the hip," *Clinical orthopaedics and related research*, vol. 466, no. 2, pp. 264–272, 2008.

[28] M. Tannast, K. A. Siebenrock, and S. E. Anderson, "Femoroacetabular impingement: radiographic diagnosis-what the radiologist should know," *American Journal of Roentgenology*, vol. 188, no. 6, pp. 1540–1552, 2007.

[29] M. Ezechieli and H. Windhagen, "Femoroazetabuläres impingement bei sportlern," *Der Chirurg*, vol. 85, no. 10, pp. 872–878, 2014.

[30] D. W. Anderson and H. E. Rubash, "Etiology of hip osteoarthritis," *The Adult Hip: Hip Preservation Surgery*, pp. 74–88, 2014.

[31] J. Mellado and N. Radi, "Cam-type deformities: Concepts, criteria, and multidetector ct features," *Radiología (English Edition)*, vol. 57, no. 3, pp. 213–224, 2015.

[32] F. Pennekamp, "Quantifizierung des hüftkopf-schenkelhals-überganges im gesunden kollektiv," Ph.D. dissertation, Universität Ulm, 2014.

[33] R. A. Zoroofi, Y. Sato, T. Nishii, N. Sugano, H. Yoshikawa, and S. Tamura, "Automated segmentation of necrotic femoral head from 3d mr data," *Computerized Medical Imaging and Graphics*, vol. 28, no. 5, pp. 267–278, 2004.

[34] K. Siebenrock, F. Ferner, P. Noble, R. Santore, S. Werlen, and T. Mamisch, "The cam-type deformity of the proximal femur arises in childhood in response to vigorous sporting activity," *Clinical Orthopaedics and Related Research®*, vol. 469, no. 11, pp. 3229–3240, 2011.

[35] O. R. Ayeni, K. Banga, M. Bhandari, Z. Maizlin, D. Golev, S. Harish, F. Farrokhyar *et al.*, "Femoroacetabular impingement in elite ice hockey players," *Knee Surgery, Sports Traumatology, Arthroscopy*, vol. 22, no. 4, pp. 920–925, 2014.

[36] K. Leunig. (2014) Hip impingement: What do we know and what do we still need to find out? Aspetar Sports Medicine Journal.

[37] M. Beck, S. Chegini, S. Ferguson, and H. S. Hosalkar, "Mechanism of femoroacetabular impingement," in *Femoroacetabular Impingement*. Springer, 2012, pp. 9–22.

[38] S. Dimmick, K. J. Stevens, D. Brazier, and S. E. Anderson, "Femoroacetabular impingement," *Radiologic Clinics of North America*, vol. 51, no. 3, pp. 337–352, 2013.

[39] R. Fraitzl, Kappe, "Das femoroacetabuläre impingement - eine häufige ursache des lsitenschmerzes beim sportler," *Deutsche Zeitschrift für Sportmedizin*, vol. 61, no. 12, pp. 292–298, 2010.

[40] H. Nötzli, T. Wyss, C. Stoecklin, M. Schmid, K. Treiber, and J. Hodler, "The contour of the femoral head-neck junction as a predictor for the risk of anterior impingement," *Bone & Joint Journal*, vol. 84, no. 4, pp. 556–560, 2002.

[41] K. A. Siebenrock and P. Henle, "X-ray examination in fai," in *Femoroacetabular Impingement*. Springer, 2012, pp. 31–39.

[42] Ejier, Leunig, and G. Mahomed and, "Cross-table lateral radiograph for screening of anterior femoral head-neck offset in patients with femoroacetabular impingement," *Hip International*, vol. 11, pp. 37–41, 2001.

[43] S. B. Weseloh G, *Coxarthrose*, B. Qualitätssicherung in der Rheumatologie, Steinkopff Verlag, Ed. Deutsche Gesellschaft für Rheumatologie e.V., 2007.

[44] K. K. Gosvig, S. Jacobsen, H. Palm, S. Sonne-Holm, and E. Magnusson, "A new radiological index for assessing asphericity of the femoral head in cam impingement," *J Bone Joint Surg Br*, vol. 89, no. 10, pp. 1309–1316, Oct 2007.

[45] M. Leunig and R. Ganz, "Femoroacetabuläres impingement. häufige ursache von zur arthrose führenden hüftbeschwerden," *Unfallchirurg*, vol. 108, no. 2, pp. 9–17, 2005.

[46] M. Beck, M. Kalhor, M. Leunig, and R. Ganz, "Hip morphology influences the pattern of damage to the acetabular cartilage femoroacetabular impingement as a cause of early osteoarthritis of the hip," *Journal of Bone & Joint Surgery, British Volume*, vol. 87, no. 7, pp. 1012–1018, 2005.

[47] L. A. Anderson, A. L. Kapron, S. K. Aoki, and C. L. Peters, "Coxa profunda: is the deep acetabulum overcovered?" *Clinical Orthopaedics and Related Research®*, vol. 470, no. 12, pp. 3375–3382, 2012.

[48] J. J. Nepple, C. L. Lehmann, J. R. Ross, P. L. Schoenecker, and J. C. Clohisy, "Coxa profunda is not a useful radiographic parameter for diagnosing pincer-type femoroacetabular impingement," *J Bone Joint Surg Am*, vol. 95, no. 5, pp. 417–423, 2013.

[49] G. Wiberg, "Studies on dysplastic acetabula and congenital subluxation of the hip joint: with special reference to the complication of osteoarthritis," *Acta Chir Scand*, vol. 83, no. 58, pp. 53–68, 1939.

[50] C. H. Heyman and C. H. Herndon, "Legg-perthes disease," *J Bone Joint Surg Am*, vol. 32, no. 4, pp. 767–778, 1950.

[51] F. Kalberer, R. J. Sierra, S. S. Madan, R. Ganz, and M. Leunig, "Ischial spine projection into the pelvis," *Clinical orthopaedics and related research*, vol. 466, no. 3, pp. 677–683, 2008.

[52] I. Zaltz, B. T. Kelly, I. Hetsroni, and A. Bedi, "The crossover sign overestimates acetabular retroversion," *Clinical Orthopaedics and Related Research®*, vol. 471, no. 8, pp. 2463–2470, 2013.

[53] C. Klein, *Orthopädie für Patienten.* Michels-Klein, 2014.

[54] K. N. Malizos, A. H. Karantanas, S. E. Varitimidis, Z. H. Dailiana, K. Bargiotas, and T. Maris, "Osteonecrosis of the femoral head: etiology, imaging and treatment," *Eur J Radiol*, vol. 63, no. 1, pp. 16–28, Jul 2007.

[55] Lehmann, *Hüftarthrose: Von der Diagnose bis zum Gelenkersatz*, 2012.

[56] A. Zibis, A. Fyllos, A. Karantanas, D. Arvanitis, Z. Dailiana, and K. Malizos, "Osteonecrosis of the femoral head–diagnosis and management," *Precision Medicine*, vol. 1, no. 2, pp. 1–8, Jun 2015.

[57] D. L. Evans, "Legg-calvé-perthes'disease," *Bone & Joint Journal*, vol. 40, no. 2, pp. 168–181, 1958.

[58] A. Roth, J. Beckmann, K. Bohndorf, and U. Maus, "Die atraumatische hüftkopfnekrose des erwachsenen," *Orthopädie und Unfallchirurgie up2date*, vol. 11, no. 03, pp. 179–196, 2016.

[59] Y. Assouline-Dayan, C. Chang, A. Greenspan, Y. Shoenfeld, and M. E. Gershwin, "Pathogenesis and natural history of osteonecrosis," *Semin. Arthritis Rheum.*, vol. 32, no. 2, pp. 94–124, Oct 2002.

[60] K. Issa, R. Pivec, B. Kapadia, S. Banerjee, and M. Mont, "Osteonecrosis of the femoral head," *Bone Joint J*, vol. 95, no. 11 Supple A, pp. 46–50, 2013.

[61] Müller, *Meine Hüfte.* Maudrich Verlag, 2013.

[62] Z.-B. Zimmer, *Hüftgelenk: axial nach Lauenstein.* Springer Verlag Heidelberg, 1979.

[63] A. Zugravu and V. Lupescu, "Sat0362 evaluation of diagnostic criteria in avascular necrosis of femoral head," *Annals of the Rheumatic Diseases*, vol. 72, no. Suppl 3, pp. A706–A706, 2013.

[64] A. Ficat, "Ischémie at nécrose osseuses," *Masson*, 1977.

[65] P. Gallinaro, A. Massè, A. Valente, and C. Cuocolo, "Osteonecrosis of the femoral head," in *European Surgical Orthopaedics and Traumatology.* Springer, 2014, pp. 2133–2145.

[66] C. J. Wirth, L. Zichner, C. Tschauner, R. M. Aigner, F. Anderhuber, and M. Beck, *Orthopädie und orthopädische Chirurgie : das Standardwerk für Klinik und Praxis. Becken, Hüfte : 114 Tabellen* -, 1st ed. Stuttgart: Georg Thieme Verlag, 2004.

[67] Y.-c. Fung, *Biomechanics: mechanical properties of living tissues.* Springer Science & Business Media, 2013.

[68] B. Klein, *FEM: Grundlagen und Anwendungen der Finite-Elemente-Methode.* Springer-Verlag, 2013.

[69] O. C. Zienkiewicz, R. L. Taylor, and R. L. Taylor, *The finite element method.* McGraw-hill London, 1977, vol. 3.

[70] R. W. Clough, "The finite element method in plane stress analysis," 1960.

[71] ——, "Early history of the finite element method from the view point of a pioneer," *International journal for numerical methods in engineering*, vol. 60, no. 1, pp. 283–287, 2004.

[72] G. A. Holzapfel, "Biomechanics of soft tissue," *The handbook of materials behavior models*, vol. 3, pp. 1049–1063, 2001.

[73] G. A. Holzapfel and H. W. Weizsäcker, "Biomechanical behavior of the arterial wall and its numerical characterization," *Computers in biology and medicine*, vol. 28, no. 4, pp. 377–392, 1998.

[74] G. A. Holzapfel and R. W. Ogden, *Biomechanics of soft tissue in cardiovascular systems.* Springer, 2014, vol. 441.

[75] A. Wagner and W. Ehlers, "Multiphasic modelling of human brain tissue for intracranial drug-infusion studies," *PAMM*, vol. 12, no. 1, pp. 107–110, 2012.

[76] A. Rohlmann, U. Mössner, G. Bergmann, and R. Kölbel, "Finite-element-analysis and experimental investigation in a femur with hip endoprosthesis," *Journal of Biomechanics*, vol. 16, no. 9, pp. 727–742, 1983.

[77] ——, "Finite-element-analysis and experimental investigation of stresses in a femur," *Journal of biomedical engineering*, vol. 4, no. 3, pp. 241–246, 1982.

[78] M. Woiczinski, A. Steinbrück, P. Weber, P. Müller, V. Jansson, and C. Schröder, "Development and validation of a weight-bearing finite element model for total knee replacement," *Computer methods in biomechanics and biomedical engineering*, vol. 19, no. 10, pp. 1033–1045, 2016.

[79] A. Steinbrück, C. Schröder, M. Woiczinski, A. Fottner, P. E. Müller, and V. Jansson, "Patellofemoral contact patterns before and after total knee arthroplasty: an in vitro measurement," *Biomedical engineering online*, vol. 12, no. 1, p. 58, 2013.

[80] ——, "The effect of trochlea tilting on patellofemoral contact patterns after total knee arthroplasty: an in vitro study," *Archives of orthopaedic and trauma surgery*, vol. 134, no. 6, pp. 867–872, 2014.

[81] A. Steinbrück, M. Woiczinski, P. Weber, P. E. Müller, V. Jansson, and C. Schröder, "Posterior cruciate ligament balancing in total knee arthroplasty: a numerical study with a dynamic force controlled knee model," *Biomedical engineering online*, vol. 13, no. 1, p. 91, 2014.

[82] A. Steinbrück, C. Schröder, M. Woiczinski, T. Müller, P. E. Müller, V. Jansson, and A. Fottner, "Influence of tibial rotation in total knee arthroplasty on knee kinematics and retropatellar pressure: an in vitro study," *Knee Surgery, Sports Traumatology, Arthroscopy*, vol. 24, no. 8, pp. 2395–2401, 2016.

[83] C. Schultze, D. Klüß, A. Lubomierski, K.-P. Schmitz, R. Bader, and W. Mittelmeier, "Finite-element-analysis of a cemented ceramic femoral component in total knee arthroplasty," *Bioceramics and Alternative Bearings in Joint Arthroplasty*, pp. 133–136, 2007.

[84] D. Kluess, H. Martin, W. Mittelmeier, K.-P. Schmitz, and R. Bader, "Influence of femoral head size on impingement, dislocation and stress distribution in total hip replacement," *Medical engineering & physics*, vol. 29, no. 4, pp. 465–471, 2007.

[85] D. Kluess, C. Zietz, T. Lindner, W. Mittelmeier, K.-P. Schmitz, and R. Bader, "Limited range of motion of hip resurfacing arthroplasty due to unfavorable ratio of prosthetic head size and femoral neck diameter," *Acta orthopaedica*, vol. 79, no. 6, pp. 748–754, 2008.

[86] D. Kluess, R. Souffrant, W. Mittelmeier, A. Wree, K.-P. Schmitz, and R. Bader, "A convenient approach for finite-element-analyses of orthopaedic implants in bone contact: modeling and experimental validation," *Computer methods and programs in biomedicine*, vol. 95, no. 1, pp. 23–30, 2009.

[87] R. Nassutt, M. A. Wimmer, E. Schneider, and M. M. Morlock, "The influence of resting periods on friction in the artificial hip." *Clinical orthopaedics and related research*, vol. 407, pp. 127–138, 2003.

[88] M. Wimmer, J. Loos, R. Nassutt, M. Heitkemper, and A. Fischer, "The acting wear mechanisms on metal-on-metal hip joint bearings: in vitro results," *Wear*, vol. 250, no. 1, pp. 129–139, 2001.

[89] M. Wimmer, C. Sprecher, R. Hauert, G. Täger, and A. Fischer, "Tribochemical reaction on metal-on-metal hip joint bearings: a comparison between in-vitro and in-vivo results," *Wear*, vol. 255, no. 7, pp. 1007–1014, 2003.

[90] M. Mathew, C. Nagelli, R. Pourzal, A. Fischer, M. Laurent, J. Jacobs, and M. Wimmer, "Tribolayer formation in a metal-on-metal (mom) hip joint: an electrochemical investigation," *Journal of the mechanical behavior of biomedical materials*, vol. 29, pp. 199–212, 2014.

[91] R. Büscher, G. Täger, W. Dudzinski, B. Gleising, M. Wimmer, and A. Fischer, "Subsurface microstructure of metal-on-metal hip joints and its relationship to wear particle generation," *Journal of Biomedical Materials Research Part B: Applied Biomaterials*, vol. 72, no. 1, pp. 206–214, 2005.

[92] G. Bergmann, F. Graichen, and A. Rohlmann, "Hip joint loading during walking and running, measured in two patients," *Journal of biomechanics*, vol. 26, no. 8, pp. 969–990, 1993.

[93] G. Bergmann, F. Graichen, A. Rohlmann, and H. Linke, "Hip joint forces during load carrying." *Clinical orthopaedics and related research*, vol. 335, pp. 190–201, 1997.

[94] G. Bergmann, F. Graichen, and A. Rohlmann, "Hip joint contact forces during stumbling," *Langenbeck's Archives of Surgery*, vol. 389, no. 1, pp. 53–59, 2004.

[95] L. Dürselen, L. Claes, and H. Kiefer, "The influence of muscle forces and external loads on cruciate ligament strain," *The American journal of sports medicine*, vol. 23, no. 1, pp. 129–136, 1995.

[96] A. Kecskeméthy, *Objektorientierte Modellirung der Dynamik von Mehrkorpersystemen mit von Ubertragungselementen.* VDI-Verl. Dusseldorf, 1993.

[97] B. Lerant, D. Raab, H. Hefter, C. Fremersdorf, M. Moll, A. Kecskeméthy, and M. Siebler, "Entwicklung eines neuen schlaganfallbewegungsscores (rehabx-score)," *Neurologie & Rehabilitation*, vol. 6, no. 2014, p. 308, 2014.

[98] F. Parafita, P. Ferreira, D. Raab, P. Flores, H. Hefter, M. Siebler, and A. Kecskeméthy, "Evaluating balance, stability and gait symmetry of stroke patients using instrumented gait analysis techniques," in *Proceedings of the Joint International Conference on Multibody System Dynamics, Montreal, QC, Canada*, vol. 29, 2016.

[99] D. Raab, Z. Tang, J. Pauli, and A. Kecskemethy, "Mobilebody: an integrated gait motion analysis tool including data-fusion with patient-specific bone geometry," in *Proceedings of the 1st International Symposium on Digital Human Modeling (DHM)*, 2011.

[100] T. Stöcker and N. J. Shah, "Grundlagen der mr-bildgebung," in *Funktionelle MRT in Psychiatrie und Neurologie*. Springer, 2013, pp. 61–78.

[101] P. Stolzmann and A. Boss, "Physikalisch-technische grundlagen," *Praxisbuch MRT Abdomen und Becken*, pp. 1–9, 2012.

[102] M. Breitenseher, *Der MR-Trainer: untere Extremität*. Georg Thieme Verlag, 2013.

[103] D. Weishaupt, V. D. Köchli, and B. Marincek, *Wie Funktioniert Mri?*. Springer, 2000, vol. 2.

[104] S. Reppenhagen, L. Rackwitz, W. Kenn, A. Roth, S. Goebel, M. Rudert, U. Nöth *et al.*, "Diagnostik der atraumatischen femurkopfnekrose des erwachsenen," *Osteologie*, vol. 19, no. 1, pp. 10–17, 2010.

[105] Radiologie.de. [Online]. Available: http://www.radiologie.de/hintergruende-und-fakten/geschichte-der-radiologie/computertomographie/

[106] H. Alkadhi, S. Leschka, P. Stolzmann, and H. Scheffel, *Wie funktioniert CT?* Springer, 2011.

[107] L. W. Goldman, "Principles of ct and ct technology," *Journal of nuclear medicine technology*, vol. 35, no. 3, pp. 115–128, 2007.

[108] L. Caspers, "Methode zur quantitative bewertung von femoroacetabuläre impingement," Master's thesis, Universität Duisburg-Essen, 2013.

[109] (2013, March) C3dformat. [Online]. Available: http://www.c3d.org/HTML/default.htm

[110] D. Raab, L. Caspers, S. Hewera, R. Cichon, J. Hewera, M. Jäger, A. Kecskemethy, W. Kowalczyk, and S. Landgraeber, "Methode zur quantitative bewertung von femoroacetabulärem impingement," in *8. Jahrestagung Deutsche Gesellschaft für Biomechanik*, 2013.

[111] S. D. Martin and J. N. Katz, "Labral tears and femoroacetabular impingement: Clinical features and arthroscopic management," *The Open Arthritis Journal*, vol. 5, no. 1, pp. 1–13, 2012.

[112] L. P. Zebala, P. L. Schoenecker, and J. C. Clohisy, "Anterior femoroacetabular impingement: a diverse disease with evolving treatment options," *The Iowa orthopaedic journal*, vol. 27, p. 71, 2007.

[113] P. Magill, J. F. Baker, and K. J. Mulhall, "Femoroacetabular impingement," *Open Sports Medicine Journal*, vol. 4, no. 1, pp. 75–80, 2010.

[114] J. T. Byrd and K. S. Jones, "Arthroscopic femoroplasty in the management of cam-type femoroacetabular impingement," *Clinical orthopaedics and related research*, vol. 467, no. 3, pp. 739–746, 2009.

[115] S. Kling, M. R. Karns, J. Gebhart, C. Kosmas, M. Robbin, S. J. Nho, A. Bedi, and M. J. Salata, "The effect of acetabular rim recession on anterior acetabular coverage a cadaveric study using the false-profile radiograph," *The American journal of sports medicine*, vol. 43, no. 4, pp. 957–964, 2015.

[116] M. Leunig, W. J. Robertson, and R. Ganz, "Femoroacetabular impingement: diagnosis and management, including open surgical technique," *Operative Techniques in Sports Medicine*, vol. 15, no. 4, pp. 178–188, 2007.

[117] C. Johnstone. (2016, April) Percy harvin injury: What is wrong with his hip? [Online]. Available: http://www.fieldgulls.com/2013-nfl-offseason/2013/7/26/4557954/percy-harvin-injuryhip-tear-labrum-seahawks-nfl

[118] R. M. Mardones, C. Gonzalez, Q. Chen, M. Zobitz, K. R. Kaufman, and R. T. Trousdale, "Surgical treatment of femoroacetabular impingement: evaluation of the effect of the size of the resection," *J Bone Joint Surg Am*, vol. 87, no. 2, pp. 273–279, 2005.

[119] M. Lavigne, J. Doyon, and P. Vendittoli, "Bone-wax granuloma after femoral neck osteoplasty," *Can J Surg*, vol. 51, no. 3, pp. E58–E60, 2008.

[120] R. C. Elmslie, "Remarks on AETIOLOGICAL FACTORS IN OSTEO-ARTHRITIS OF THE HIP-JOINT," *Br Med J*, vol. 1, no. 3757, pp. 1–46, Jan 1933.

[121] R. O. Murray, "The aetiology of primary osteoarthritis of the hip," *Br J Radiol*, vol. 38, no. 455, pp. 810–824, Nov 1965.

[122] *Acetabular dysplasia and development of osteoarthritis of the hip*, The hip: Proceedings of the Second Open Scientigic Meeting of the Hip Society. S. Stulberg and W. Harris, 1974.

[123] S. Stulberg, L. Cordell, and W. Harris, "Unrecognized childhood hip disease: a major cause of idiopathic osteoarthritis of the hip," *The hip: Proceedings of the Third Meeting of the Hip Societey*, vol. 3, pp. 212–228, 1975.

[124] L. Solomon, "Patterns of osteoarthritis of the hip," *J Bone Joint Surg Br*, vol. 58, no. 2, pp. 176–183, May 1976.

[125] R. O. Murray and C. Duncan, "Athletic activity in adolescence as an etiological factor in degenerative hip disease," *J Bone Joint Surg Br*, vol. 53, no. 3, pp. 406–419, Aug 1971.

[126] D. Resnick, "The 'tilt deformity' of the femoral head in osteoarthritis of the hip: a poor indicator of previous epiphysiolysis," *Clin Radiol*, vol. 27, no. 3, pp. 355–363, Jul 1976.

[127] A. R. Altenberg, "Acetabular labrum tears: a cause of hip pain and degenerative arthritis," *South. Med. J.*, vol. 70, no. 2, pp. 174–175, Feb 1977.

[128] T. Ueo and M. Hamabuchi, "Hip pain caused by cystic deformation of the labrum acetabulare," *Arthritis Rheum.*, vol. 27, no. 8, pp. 947–950, Aug 1984.

[129] J. C. McCarthy, P. C. Noble, M. R. Schuck, J. Wright, and J. Lee, "The watershed labral lesion: its relationship to early arthritis of the hip," *J Arthroplasty*, vol. 16, no. 8 Suppl 1, pp. 81–87, Dec 2001.

[130] S. Myers, H. Eijer, and R. Ganz, "Anterior femoroacetabular impingement after periacetabular osteotomy." *Clinical orthopaedics and related research*, vol. 363, pp. 93–99, 1999.

[131] R. Ganz, T. J. Gill, E. Gautier, K. Ganz, N. Krugel, and U. Berlemann, "Surgical dislocation of the adult hip a technique with full access to the femoral head and acetabulum without the risk of avascular necrosis," *J Bone Joint Surg Br*, vol. 83, no. 8, pp. 1119–1124, Nov 2001.

[132] R. Ganz, J. Parvizi, M. Beck, M. Leunig, H. Nötzli, and K. A. Siebenrock, "Femoroacetabular impingement: a cause for osteoarthritis of the hip." *Clinical orthopaedics and related research*, vol. 417, pp. 112–120, 2003.

[133] G. T. Rab, "The geometry of slipped capital femoral epiphysis: implications for movement, impingement, and corrective osteotomy," *J Pediatr Orthop*, vol. 19, no. 4, pp. 419–424, 1999.

[134] M. Lavigne, L. Jean-Michel, and V. Pascal-André, "Historical evolution of the concept of femoroacetabular impingement as a cause of hip osteoarthritis," in *Femoroacetabular Impingement*. Springer, 2012, pp. 3–7.

[135] M. Ribas, R. Ledesma, C. Cardenas, O. Marin-Peña, J. Toro, and E. Caceres, "Clinical results after anterior mini-open approach for femoroacetabular impingement in early degenerative stage," *Hip Int*, vol. 20, no. Suppl 7, pp. 36–42, 2010.

[136] F. Haddad, "Femoro-acetabular impingement: An arthroscopic solution," *Bone Joint J*, vol. 95, no. SUPP 22, pp. 46–46, 2013.

[137] R. L. Garijo, R. García-Bógalo, and E. Diez-Nicolas, "Evidence-based medicine in the treatment of femoroacetabular impingement," in *Femoroacetabular Impingement*. Springer, 2012, pp. 65–71.

[138] D. S. Hungerford, "Osteonecrosis: avoiding total hip arthroplasty," *J Arthroplasty*, vol. 17, no. 4 Suppl 1, pp. 121–124, Jun 2002.

[139] I. Dudkiewicz, A. Covo, M. Salai, A. Israeli, Y. Amit, and A. Chechik, "Total hip arthroplasty after avascular necrosis of the femoral head: does etiology affect the results?" *Arch Orthop Trauma Surg*, vol. 124, no. 2, pp. 82–85, Mar 2004.

[140] C. J. Ortiguera, I. T. Pulliam, and M. E. Cabanela, "Total hip arthroplasty for osteonecrosis: matched-pair analysis of 188 hips with long-term follow-up," *J Arthroplasty*, vol. 14, no. 1, pp. 21–28, Jan 1999.

[141] M. A. Mont, J. J. Carbone, and A. C. Fairbank, "Core decompression versus nonoperative management for osteonecrosis of the hip." *Clinical orthopaedics and related research*, vol. 324, pp. 169–178, 1996.

[142] R. P. Ficat, "Idiopathic bone necrosis of the femoral head. Early diagnosis and treatment," *J Bone Joint Surg Br*, vol. 67, no. 1, pp. 3–9, Jan 1985.

[143] T. Kiaer, N. W. Pedersen, K. D. Kristensen, and H. Starklint, "Intra-osseous pressure and oxygen tension in avascular necrosis and osteoarthritis of the hip," *J Bone Joint Surg Br*, vol. 72, no. 6, pp. 1023–1030, Nov 1990.

[144] W. Medical, "X-ream," Patent.

[145] S. Landgraeber, J. M. Theysohn, T. Classen, M. Jäger, S. Warwas, H.-P. Hohn, and W. Kowalczyk, "Advanced core decompression, a new treatment option of avascular necrosis of the femoral head–a first follow-up," *Journal of tissue engineering and regenerative medicine*, vol. 7, no. 11, pp. 893–900, 2013.

[146] W. Medical. (2016, 11) Product overview prodense. [Online]. Available: http://www.wright.com/physicians/prodense/product-overview

[147] R. M. Urban, T. M. Turner, D. J. Hall, N. Inoue, and S. Gitelis, "Increased bone formation using calcium sulfate-calcium phosphate composite graft." *Clinical orthopaedics and related research*, vol. 459, pp. 110–117, 2007.

[148] W. Medical. (2016, 11) Advanced core decompression system - x-ream percutaneous expandable reamer pro-dense core decompression procedure kit surgical technique. Wright Medical. [Online]. Available: http://documents.wright.com/Document/Get/009166

[149] S. Landgraeber, T. N. Tran, T. Claßen, S. Warwas, J. Theysohn, A. Lazik, M. Jäger, and W. Kowalczyk, "Geometric analysis of an expandable reamer for treatment of avascular necrosis of the femoral head," *Archives of orthopaedic and trauma surgery*, vol. 135, no. 10, pp. 1357–1362, 2015.

[150] A. G. Holzapfel, "Nonlinear solid mechanics ii," 2000.

[151] W. Rust, *Nichtlineare finite-elemente-berechnungen*. Springer, 2011.

[152] J. Bonet and R. D. Wood, *Nonlinear continuum mechanics for finite element analysis*. Cambridge university press, 1997.

[153] C. Gebhardt, *Praxisbuch FEM mit ANSYS Workbench: Einführung in die lineare und nichtlineare Mechanik*. Carl Hanser Verlag GmbH Co KG, 2014.

[154] A. H. Viewer, "Mechanical apdl - types of solvers," *ANSYS Help Viewer*, 2017.

[155] R. Kotz and D. G. Poitout, *Biomechanics and biomaterials in orthopedics*. Springer Science & Business Media, 2013.

[156] E. Wang. Ansys contact. CAD-FEM GmbH, Germany.

[157] A. H. Viewer, "Contact formulation theory, global mesh controls, etc." *ANSYS Help Viewer*, 2017.

[158] H.-H. Lee, *Finite element simulations with ANSYS workbench 16*. SDC publications, 2015.

[159] J. C. Clohisy, P. E. Beaulé, A. O'Malley, M. R. Safran, and P. Schoenecker, "Aoa symposium," *J Bone Joint Surg Am*, vol. 90, no. 10, pp. 2267–2281, 2008.

[160] K. Klaue, C. Durnin, and R. Ganz, "The acetabular rim syndrome. a clinical presentation of dysplasia of the hip," *Bone & Joint Journal*, vol. 73, no. 3, pp. 423–429, 1991.

[161] Vicon. (2017) Manual plug-in gait.

[162] Siemens. (2015, July) Siemens healthcare gmbh dicom format. http://www.healthcare.siemens.com/services/it-standards/dicom. [Online]. Available: http://www.healthcare.siemens.com/services/it-standards/dicom

[163] G. Pahl and W. Beitz, *Konstruktionslehre: Methoden und Anwendung*. Springer-Verlag, 2013.

[164] C. P. (2015, June) Meshlab. http://meshlab.sourceforge.net/. [Online]. Available: http://meshlab.sourceforge.net/

[165] M. Kazhdan, M. Bolitho, and H. Hoppe, "Poisson surface reconstruction," in *Proceedings of the fourth Eurographics symposium on Geometry processing*, vol. 7, 2006.

[166] F. Radetzki, B. Saul, A. Hagel, T. Mendel, T. Döring, K. Delank, D. Wohlrab, and D. Stoevesandt, "Three-dimensional virtual simulation and evaluation of the femoroacetabular impingement based on black bone mra," *Archives of orthopaedic and trauma surgery*, vol. 135, no. 5, pp. 667–671, 2015.

[167] A. L. Kapron, *Kinematics of femoroacetabular impingement*. THE UNIVERSITY OF UTAH, 2013.

[168] M. Yazdifar, M. Yazdifar, P. Rahmanivahid, S. Eshraghi, I. Esat, and M. Chizari, "Evaluation of hip impingement kinematics on range of motion," in *Human-Computer Interaction. Towards Intelligent and Implicit Interaction*. Springer, 2013, pp. 262–269.

[169] R. M. Ehrig, W. R. Taylor, G. N. Duda, and M. O. Heller, "A survey of formal methods for determining the centre of rotation of ball joints," *Journal of biomechanics*, vol. 39, no. 15, pp. 2798–2809, 2006.

[170] B. Siciliano, L. Sciavicco, L. Villani, and G. Oriolo, *Robotics: modelling, planning and control*. Springer Science & Business Media, 2010.

[171] S. Westermaier, "Entwicklung von patientindividuellen mehrkörpermodellen und fem analysen zur behanldungsoptimierung von femoroacetabulärem impingement," Master's thesis, Universität Duisburg-Essen, 2015.

[172] A. L. Kapron, S. K. Aoki, C. L. Peters, and A. E. Anderson, "In-vivo hip arthrokinematics during supine clinical exams: Application to the study of femoroacetabular impingement," *Journal of biomechanics*, vol. 48, no. 11, pp. 2879–2886, 2015.

[173] F. Liska *et al.*, "Vergleich der mechanischen eigenschaften von spongiösem knochen verschiedener spezies und künstlichem knochen," Ph.D. dissertation, München, Technische Universität München, Diss., 2012, 2012.

[174] D. G. Poitout *et al.*, *Biomechanics and biomaterials in orthopedics*. Springer, 2004.

[175] K. Moglo and A. Shirazi-Adl, "On the coupling between anterior and posterior cruciate ligaments, and knee joint response under anterior femoral drawer in flexion: a finite element study," *Clinical Biomechanics*, vol. 18, no. 8, pp. 751–759, 2003.

[176] S. Ferguson, J. Bryant, and K. Ito, "The material properties of the bovine acetabular labrum," *Journal of orthopaedic research*, vol. 19, no. 5, pp. 887–896, 2001.

[177] X. Zhao, E. Chosa, K. Totoribe, and G. Deng, "Effect of periacetabular osteotomy for acetabular dysplasia clarified by three-dimensional finite element analysis," *Journal of orthopaedic science*, vol. 15, no. 5, pp. 632–640, 2010.

[178] A. E. Anderson, B. J. Ellis, S. A. Maas, and J. A. Weiss, "Effects of idealized joint geometry on finite element predictions of cartilage contact stresses in the hip," *Journal of biomechanics*, vol. 43, no. 7, pp. 1351–1357, 2010.

[179] S. Chegini, M. Beck, and S. J. Ferguson, "The effects of impingement and dysplasia on stress distributions in the hip joint during sitting and walking: a finite element analysis," *Journal of Orthopaedic Research*, vol. 27, no. 2, pp. 195–201, 2009.

[180] A. D. Speirs, M. O. Heller, G. N. Duda, and W. R. Taylor, "Physiologically based boundary conditions in finite element modelling," *Journal of biomechanics*, vol. 40, no. 10, pp. 2318–2323, 2007.

[181] K. Rudman, R. Aspden, and J. Meakin, "Compression or tension? the stress distribution in the proximal femur," *Biomedical engineering online*, vol. 5, no. 1, p. 1, 2006.

[182] T. Tran, W. Kowalczyk, H. Hohn, M. Jäger, and S. Landgraeber, "Effect of the stiffness of bone substitutes on the biomechanical behaviour of femur for core decompression," *Medical Engineering & Physics*, vol. 38, no. 9, pp. 911–916, 2016.

[183] T. Tran, S. Warwas, M. Haversath, T. Classen, H. Hohn, M. Jäger, W. Kowalczyk, and S. Landgraeber, "Experimental and computational studies on the femoral fracture risk for advanced core decompression," *Clinical Biomechanics*, vol. 29, no. 4, pp. 412–417, 2014.

[184] K.-C. G. Ng, "Finite element analysis to examine the mechanical stimuli distributions in the hip with cam femoroacetabular impingement," Ph.D. dissertation, Université d'Ottawa/University of Ottawa, 2011.

[185] B. Couteau, M.-C. Hobatho, R. Darmana, J.-C. Brignola, and J.-Y. Arlaud, "Finite element modelling of the vibrational behaviour of the human femur using ct-based individualized geometrical and material properties," *Journal of Biomechanics*, vol. 31, no. 4, pp. 383–386, 1998.

[186] I. Aleksander and H. Morton, *An introduction to neural computing*. Chapman and Hall London, 1990, vol. 240.

[187] W. S. McCulloch and W. Pitts, "A logical calculus of the ideas immanent in nervous activity," *The bulletin of mathematical biophysics*, vol. 5, no. 4, pp. 115–133, 1943.

[188] C. C. Aggarwal and C. K. Reddy, *Data clustering: algorithms and applications*. Chapman and Hall/CRC, 2013.

[189] S. S. Haykin, S. S. Haykin, S. S. Haykin, and S. S. Haykin, *Neural networks and learning machines*. Pearson Upper Saddle River, NJ, USA:, 2009, vol. 3.

[190] A. Candel, V. Parmar, E. LeDell, and A. Arora, "Deep learning with h2o," *H2O. ai Inc.,*, 2016.

[191] M. Sangeux, A. Peters, and R. Baker, "Hip joint centre localization: Evaluation on normal subjects in the context of gait analysis," *Gait & posture*, vol. 34, no. 3, pp. 324–328, 2011.

[192] G. R. Milner and J. L. Boldsen, "Humeral and femoral head diameters in recent white american skeletons," *Journal of forensic sciences*, vol. 57, no. 1, pp. 35–40, 2012.

[193] R. Sutter, T. J. Dietrich, P. O. Zingg, and C. W. Pfirrmann, "How useful is the alpha angle for discriminating between symptomatic patients with cam-type femoroacetabular impingement and asymptomatic volunteers?" *Radiology*, vol. 264, no. 2, pp. 514–521, 2012.

[194] K. S. Rakhra, A. M. Sheikh, D. Allen, and P. E. Beaulé, "Comparison of mri alpha angle measurement planes in femoroacetabular impingement," *Clinical orthopaedics and related research*, vol. 467, no. 3, pp. 660–665, 2009.

[195] T. C. Pollard, R. N. Villar, M. R. Norton, E. D. Fern, M. R. Williams, D. J. Simpson, D. W. Murray, and A. J. Carr, "Femoroacetabular impingement and classification of the cam deformity: the reference interval in normal hips," *Acta orthopaedica*, vol. 81, no. 1, pp. 134–141, 2010.

[196] M. Neumann, Q. Cui, K. A. Siebenrock, and M. Beck, "Impingement-free hip motion: the normal angle alpha after osteochondroplasty," *Clinical orthopaedics and related research*, vol. 467, no. 3, pp. 699–703, 2009.

[197] M. Lequesne, J. Malghem, and E. Dion, "The normal hip joint space: variations in width, shape, and architecture on 223 pelvic radiographs," *Annals of the rheumatic diseases*, vol. 63, no. 9, pp. 1145–1151, 2004.

[198] G. von Salis-Soglio, "Die neutral-0-methode," in *Klinische Untersuchung der Stütz- und Bewegungsorgane*. Springer, 2015, pp. 11–18.

[199] R. Sutter, T. J. Dietrich, P. O. Zingg, and C. W. Pfirrmann, "Femoral antetorsion: comparing asymptomatic volunteers and patients with femoroacetabular impingement," *Radiology*, vol. 263, no. 2, pp. 475–483, 2012.

Online-Buchshop für Ingenieure

VDI nachrichten

BUCHSHOP

Online-Shops

Fachliteratur und mehr - jetzt bequem online recherchieren & bestellen unter: www.vdi-nachrichten.com/Der-Shop-im-Ueberblick

Täglich aktualisiert: Neuerscheinungen VDI-Schriftenreihen

Im Buchshop von vdi-nachrichten.com finden Ingenieure und Techniker ein speziell auf sie zugeschnittenes, umfassendes Literaturangebot.

Mit der komfortablen Schnellsuche werden Sie in den VDI-Schriftenreihen und im Verzeichnis lieferbarer Bücher unter 1.000.000 Titeln garantiert fündig.

Im Buchshop stehen für Sie bereit:

VDI-Berichte und die Reihe **Kunststofftechnik**:

Berichte nationaler und internationaler technischer Fachtagungen der VDI-Fachgliederungen

Fortschritt-Berichte VDI:

Dissertationen, Habilitationen und Forschungsberichte aus sämtlichen ingenieurwissenschaftlichen Fachrichtungen

Newsletter „Neuerscheinungen":

Kostenfreie Infos zu aktuellen Titeln der VDI-Schriftenreihen bequem per E-Mail

Autoren-Service:

Umfassende Betreuung bei der Veröffentlichung Ihrer Arbeit in der Reihe Fortschritt-Berichte VDI

Buch- und Medien-Service:

Beschaffung aller am Markt verfügbaren Zeitschriften, Zeitungen, Fortsetzungsreihen, Handbücher, Technische Regelwerke, elektronische Medien und vieles mehr – einzeln oder im Abo und mit weltweitem Lieferservice

Die Reihen der Fortschritt-Berichte VDI:

1 Konstruktionstechnik/Maschinenelemente
2 Fertigungstechnik
3 Verfahrenstechnik
4 Bauingenieurwesen
5 Grund- und Werkstoffe/Kunststoffe
6 Energietechnik
7 Strömungstechnik
8 Mess-, Steuerungs- und Regelungstechnik
9 Elektronik/Mikro- und Nanotechnik
10 Informatik/Kommunikation
11 Schwingungstechnik
12 Verkehrstechnik/Fahrzeugtechnik
13 Fördertechnik/Logistik
14 Landtechnik/Lebensmitteltechnik
15 Umwelttechnik
16 Technik und Wirtschaft
17 Biotechnik/Medizintechnik
18 Mechanik/Bruchmechanik
19 Wärmetechnik/Kältetechnik
20 Rechnerunterstützte Verfahren (CAD, CAM, CAE CAQ, CIM ...)
21 Elektrotechnik
22 Mensch-Maschine-Systeme
23 Technische Gebäudeausrüstung

ISBN 978-3-18-329517-3